MAGNETIC PROPERTIES OF NANOSCALE CONDUCTORS

A Dissertation

Presented to the Faculty of the Graduate School

of Cornell University

in Partial Fulfillment of the Requirements for the Degree of

Doctor of Philosophy

by

Shaffique Adam

May 2006

MAGNETIC PROPERTIES OF NANOSCALE CONDUCTORS

Shaffique Adam, Ph.D.

Cornell University 2006

This doctoral dissertation examines some magnetic properties of nanoscale conductors. It comprises two classes of problems, namely, the response of closed nanoscopic systems to an external magnetic field, and the magnetization dependent transport of nanomagnets. In the first class of closed nanoscopic structures like quantum dots or metal grains, the system has discrete energy levels which can be modeled by Random Matrix Theory. The addition of a magnetic field is analyzed using a crossover random matrix model. In Chapter 2, we show that in the crossover there exist correlations between elements of the same eigenvector and between different eigenvectors. We show that these correlations between different eigenvectors lead to enhanced fluctuations of the electron-electron interaction matrix elements which are absent in the pure ensembles. In Chapter 3, we generalize these results to analyze the magnetic field response of energy levels in ultrasmall metal grains. We present a theory of mesoscopic fluctuations of g tensors and avoided crossing energies in a small metal grain that contains both orbital and spin contributions to the g tensor.

In the second class of problems we study two effects in small ferromagnets where the charge transport is coupled to the magnetization. In Chapter 4, we show that a sufficiently large unpolarized current can cause a spin-wave instability in a nanomagnet with asymmetric contacts. The dynamics beyond the instability

is calculated analytically in the perturbative regime of small spinwave amplitudes, and numerically for larger currents. In Chapter 5, we study "anisotropic magnetoresistance fluctuations" which is the ferromagnetic analog of the well-known Universal Conductance Fluctuations in metals. The conductance of a ferromagnetic particle depends on the relative orientation of the magnetization with respect to the direction of current flow. This phenomenon is known as "anisotropic magnetoresistance" and has no counterpart in normal-metal conductors. We show that quantum interference leads to an additional, random yet (statistically) universal dependence of the conductance of a ferromagnet on the magnetization direction. The mechanism for these anisotropic magnetoresistance fluctuations is the interplay of spin-orbit scattering, random impurity scattering, and the ferromagnet's exchange field.

BIOGRAPHICAL SKETCH

The author, Shaffique Adam, was born on January 20th 1978 in Nairobi, Kenya to Shiraz T. N. Adam and Guli Adam. His parents were among the fourth generation of Kenyan-Asians, who left the Indian province of Gujarat in the 1900s to settle on the East African coast. He attended the Aga Khan Academy, finishing top of his class with all A-grades in the University of London GCE O-level and A-level examinations. In highschool, among other things he was the Head Prefect, made the school basketball team, climbed Mt. Kilimanjaro, and represented Kenya in regional chess tournaments. Shaffique then went on to Stanford University. He graduated with a BS in Physics, a minor in Mathematics, departmental honors and a University distinction. Among the highlights of his time at Stanford was being the Class of 2000 Baccalaureate speaker, spending four months as an exchange student at Magdalen College, Oxford and a course on the history of Jerusalem that was followed by a trip there. Shaffique also developed data analysis algorithms for the Gravity Probe B experiment, and was awarded both departmental and university research grants to work with Giorgio Gratta on acoustic neutrino detection. Shaffique then moved to Cornell University, where under the direction of Piet Brouwer, completed his MS and PhD doing theoretical work on the properties of nanoscale systems. In addition to doing exciting research, the highlights of his Cornell experience include getting married in 2004, being a Graduate Resident Fellow for the Alice H. Cook House, writing biweekly opinion columns for the Cornell Daily Sun, and getting elected as the Secretary of the Graduate and Professional Student Assembly. Shaffique recently accepted a postdoctoral position at the Condensed Matter Theory Center at the University of Maryland.

Dedicated to the memory of a dear friend, Tejal A. B. Shah, who passed away in a road accident just weeks before her 25th birthday

ACKNOWLEDGEMENTS

"It takes a village to raise a child"

- Kenyan Proverb

It would be impossible for me to thank all the people who have shaped me and enabled me to complete this doctoral dissertation. I owe all my accomplishments to the three villages of Nairobi, Stanford and Cornell and the numerous individuals and institutions in these communities under whose care I was nurtured and guided. A complete acknowledgment would have to include all the numerous role models and friends I have encountered throughout my schooling and the diverse and vibrant cultural, social, religious, and political organizations that have always been part of my life – but this daunting task is for another day, and all I can offer today is a sincere thank-you to all the many people who in so many ways have helped me reach this far in life.

Knowing full well that following the custom of using this space to list people who have had a significant positive impact on my life will inevitably result in important omissions, I will nonetheless make an attempt. There are four people who clearly stand out and deserve special mention. First and foremost, my mother, Guli Adam, who sparked my interest in physics at a young age, and who has always been a constant source of support. Even the small things, like sending me daily e-mail, when aggregated over ten years, has an enormous impact. Throughout the ups and downs of the PhD program, what did not change was the daily doses of encouragement from home. Second, I would like to thank my deceased father, Shiraz T. N. Adam. I could not have asked for a better father. He has shaped most of my values and much of my outlook towards the world.

I would like to thank my wife, Munira Alhad Hyder-Adam, mostly for making the past three years among the happiest of my life, but also for her crucial support at those moments of frustration that accompany every doctoral program. And finally, I would like to thank my advisor Piet Brouwer. For his enthusiasm that made my research exciting and meaningful, for his patience as a teacher, and for being a role model on how to be an ethical and responsible member of society. These four individuals have had a strong impact on my life, and I will forever be grateful to them.

I thank my Special Committee: Tomás Arias, for his crucial advice at the beginning of my graduate career that got me taking my first ever Solid State physics course, and for much guidance since then; Dan Ralph, for teaching that Solid State physics course in an innovative and exciting way that took me right to the doorstep of my current research group. Since then, Dan has provided much advice, both scientific and otherwise, and I will always appreciate the neverending stream of exciting experimental discoveries that he was always happy to discuss.

The work in this thesis would not have been possible without my scientific collaborators: Xavier Waintal, Jim Sethna, Mikhail Polianski, Stephan Braig, Prashant Sharma, Saar Rahav, Markus Kindermann, and Joern Kupferschmidt. Of these I would like to single out Xavier, Jim and Prashant for additionally serving as mentors and to Stephan, Prashant, Saar and Joern for being good friends.

During my first Summer at Cornell, Xavier guided me through my first condensed matter theory project; Jim's insightful questions during a seminar I gave began an exciting collaboration leading to much of the work that is presented in Chapter 2, and Prashant was always full of ideas and enthusiasm, and served as a sounding board for my ideas, helping me formulate them more concretely.

Stephan and I shared an office for four years, and along with the physics came many philosophical and sociological discussions – and plenty of skiing and golf.

One advantage of being at Cornell is the collaboration with excellent experimental groups. I would like to thank the experimentalists with whom I worked very closely, especially Jason Petta, Sergey Kiselev and Jack Sankey.

I also acknowledge support from the Cornell Center for Nanoscale Systems, the National Science Foundation and the Cornell University Graduate Fellowship that funded most of my graduate studies, as well as the S.M.W. Mulji Educational Trust, Stanford University and my family for funding my undergraduate education. I appreciate travel grants from I2CAM and NATO/ASI that helped fund Summer conferences in Les Houches, Trieste and Copenhagen. I have also benefited from the Cornell Center for Materials Research Computing Facility.

I would also like to thank my family: my brother, Raheem Adam, and my aunt Amina Harji, who have always been there for me in every possible way. It is knowing that I have the support of my immediate family that has enabled me to journey out confidently into the world.

I am grateful to my mother-in-law Fatma Hyder who has done so much for both Munira and me. Many thanks to the rest of the Adam family including my deceased grandfather Tajdin Noormohamed Adam; my grandmother Khadhija Adam; my aunt Nabat Adam, her children Naaz Rahemtulla, Saleem Fazal and Shaffiq Rahemtulla (and his family); my uncle Amir Adam and his family; My aunt Yasmin Jamal, my uncle Zul Adam and his family; and to all of the Hyder family (including the Shirazys, the Kibwanas and the Abdulwahabs), a big thank-you for all your support.

At Cornell I am grateful for the guidance and friendship of Shawkat and Parvine

Toorawa; Ross Brann, Eileen Yagoda and Allon Brann; Yasmin Koolsam; Marianne Scott; Janet Shortall; Pastor Rick Bair; Jean Reese; Douglas McGregor; Gerburg Brouwer and Syed Rizvi. And for the support of Alison Power, Andy Bass, Persis Drell and David Rubin.

From my time at Stanford, I especially would like to thank some of the faculty who made a strong impact on me including Ebrahim Moosa (Religious Studies), Bob Gregg (Religious Studies), Giorgio Gratta (Physics), Yasha Eliashberg (Mathematics), Robert Laughlin (Physics) and Krystyna von Henneberg (History). In addition I would also like to thank Kelly Denton-Borhaug, Doug Osheroff, Charlie Marcus, Pat Burchat, Eric Roberts, Scott Sagan, Ticien Carlson and Carol St. Louis.

I have been very fortunate to make so many good friends in so many different parts of the world. A special thank-you to Sandra Chesoni and Nauman Khan who are both close to my heart.

Of all my childhood friends from Kenya, I am grateful to the few who have remained in close contact till this day: Suzzanne Gitata, Salim Jivanji, Sajad Abdulla, Alykhan Jamal and Sameer Lalani.

I will always cherish my Stanford days and the friends I made there, and I am especially thankful to those close friends who have made an effort to keep in touch: Hussein Kanji, Murad Akhter, Imran Maskatia, Uzma Siddiqui, Hamed Saeed, Omer Saeed, Carlos Ancona Torres, Katherine Flynn and Ilya Mandel. I also thank Eren Tasar, Meklit Berhan, Fahd and Ayesha Khan, Frederick Matsen, Adil Husain, Ari Nordhagen, Gabriel Flores, Charity Lu, Munira Rahemtulla, Saurabh Prakash and Mung Chiang.

At Cornell I had great fun living for two years at the headquarters of the Maple

Hill Mafia. A special thank-you to the friends I made there: Ali Gokirmak, Helena Silva, Kursad Araz, Umer Syed, Hazer Inaltekin, Faisal Zubairi, Mandy Esch, Gurbuz Gunes, Halit Ozkan, Khalid Al-Banaa, Meriam Djeledi, Aman Siddiqi, Alper Bozkurt, Gokhan Arikan and Murat Baday.

Many of my closest friends were from the Cornell Muslim community: Shada El-Sharif, Nida Chaudhary, Reza Samad, Nosheen Ali, Tareq Aryne, Wajih Effendi, Aneela Haider, Yusif Akhund, Qasim Husain, and Aziz Alkhalifa; and from JAM: Julia Stone, Nicole Simon, Rima Grunes (and family), Simon Garcia, Rachel Byrd and Joe Regenstein.

The physics department at Cornell has a wonderful community with amazing people and dear friends. Foremost I would like to thank Harald Pfeiffer (and his wife Sylke) to whom I am indebted for their friendship and their kindness which began even before I decided to come to Cornell. I have shared in wonderful activities with Jeandrew Brink, Faisal Ahmad, Thalia Mills, Gil Toomes, Eric Ryan, Allie King and Amena Siddiqi; ranging from hiking in the Adirondacks to day trips to New York City. I also thank Eileen Tan, Diane Wong, Sourish Basu, Iya Khalil, Josh Waterfall, Mark Wyman, Ethan Bernard, Ethan Minot, Sami Rosenblatt, Marko Nanias, Saikat Ghosh, Saswat Sarangi, Connie Chang, Maurizio Chinchio, Hande Üstünel, Vera Sazonova, Ribhu Kaul, Umberto Pesavento, Jonathan Wrubel and Dan Goldbaum.

I am very grateful to some of the Physics and CCMR outreach, administrative and support staff who have been especially helpful during my time at Cornell including Nevjinder Singhota, Julianne Bauer-Hutchinson, Barry Robinson, Douglas Milton, Judy Wilson, Larisa Vygran, Connie Wright, Deb Hatfield and Lisa Margosian.

Finally, I would also like to thank some people who did not fall into any of the above categories. These include: Wendy Clavano, Saiful and Dian Mahdi, Mazalan Kamis (and family), Hakiem and Margo Nankoe, Emily Sensenbach, Stephanie Meyer, Father Bob Smith, Marianna Wolfner, Iftikhar Dadi, Edward Abrokwah, Gavin Hurley, Esther Tang, Nadeem Siddiqui, Hameedah Merchant, Lello Tesema, Malka Benjamin, Ben Towbin, Nuha Abdurahman, Sabeen Virani, Julia Levy, Qahir Dhanani, Rebecca Abou-Chedid, Razan Francis, Shaheena Karbanee, Michael Crawford, Amayas Toufik Mostefaoui, Jontie Karden, Carolyn Taber and Sue McNamara.

I am certain that I have forgotten to include many people. To those who have made valuable contributions to my life, and have escaped my memory, accept my gratitude, and know that at some point after I submit this thesis, I will recall your contribution and wish that I had remembered earlier.

Ithaca, May 2006

TABLE OF CONTENTS

LIST OF TABLES

LIST OF FIGURES

Chapter 1

Introduction

This thesis should be viewed as a modest theoretical contribution to the rapidly expanding field of nanoscience. Nanoscience is a relatively young and cross-disciplinary area of study that has been fueled by major advances in experimental techniques to fabricate and probe systems at the nanometer scale. While there are many basic science questions that emerge at this length scale, it would be a very skewed perspective to not mention the emphasis that is given towards making useful technology, ranging from the more practical like magnetic memory devices to the more fanciful ideas in quantum computing or carbon nanotube elevators. Perhaps one way to appreciate this tremendous technological achievement of making reproducible devices with nanometer dimensions is to contrast this scale with the thickness of human hair which is about 100,000 nanometers. It is without doubt that some of these devices being imagined today will in the next decade or two, be standard components in products made by the computer industry.

From a more basic science perspective, the world looks quite different at nanometer length scales. In particular, we are dealing with systems of the order of only ten to a hundred atoms. The properties of atomic systems is known to be determined

from quantum theory, yet attempts to analytically solve the Schrödinger equation for more than a single atom become futile. Numerical solutions fare better and routinely determine the ground state properties of systems comprising tens of atoms, but for larger systems or those out of equilibrium, alternative techniques are needed.

It is important to point out that for macroscopic systems, the law of large numbers and the machinery of statistical physics comes into play. For example, while quantum theory suggests that there is a finite probability for the water in your glass to spontaneously escape its confining barrier, the law of large numbers tells us that we would have to wait longer than the age of the universe to expect to see this. What this also illustrates is that our intuition built on observations of the macroscopic world breaks down at these smaller length scales.

Although the statistical methods used to average over 10^{26} atoms and derive macroscopic properties fail to work at the nanoscale, it is nonetheless still reasonable to use bulk concepts like temperature, entropy, average density and resistance. The methods that were developed to understand the effects of quantum coherence on these macroscopic quantities gave rise to a branch of condensed matter physics known as mesoscopic physics. Since the mid-1980s this field has explored the boundary between the quantum and classical worlds by studying the unexpected phenomena that emerge from the rich interplay between electron interaction, impurity scattering, and boundary conditions.

One of the most important results from mesoscopic physics is that the correct question to ask at this length scale is not about a particular sample with specific boundary conditions or disorder configuration, but rather a statistical one about the properties of an ensemble of samples with similar size, shape and impurity con-

centration, but with different actual atomic-scale shape and disorder realizations. Such an average over macroscopically equivalent, but microscopically different ensembles is the only one that makes sense if one is to describe the phenomena seen in actual experiments where the resolution is on the nanoscale and not the atomic scale. There are many different techniques employed by the mesoscopic community to perform such microscopic averages. In this thesis we employ two such techniques: Random Matrix Theory which is described in Section 1.1, and Diagrammatic Perturbation Theory discussed in Section 1.4.

Another way to think about nanoscale systems is a sort of top-down approach. Physics is all about different natural laws that begin to play out at different length-scales, and as one goes to smaller length scales or colder temperatures, certain physical phenomena that were dominant cease to be so, giving rise to new phenomena. Sometimes this can be very useful from a technological standpoint. An illustrative example of this that is related to Chapter 4 of this thesis is the physics of the spin-transfer torque. For most of today's magnetic memory devices, information is stored as bits of spin-up or spin-down magnets that are flipped by an optimized cross-bar network of current carrying wires running above the bit. The physics of this has been known since 1820 when the experimental work by Ørsted and theoretical work by Ampere showed that current in a wire generates a magnetic field. It is this field that flips the magnetic bit allowing one to write information. In 1996, Slonczewski [1] and Berger [2] predicted that when a spin-polarized current is passed through a ferromagnet it transfers the transverse component of its spin angular momentum to the ferromagnet. This spin-transfer torque scales proportional to the current density (i.e current per unit area), while the Ampere field is proportional to the total current. For nanometer length-scales the spin-transfer

mechanism dominates and becomes a far more effective mechanism for flipping magnetic bits. Notwithstanding the technological application, this is a typical example of how new physical phenomena emerges at the nanoscale. Despite many attempts (starting from the original works of Slonczewksi and Berger) to provide a microscopic derivation for the spin-transfer torque, none does too much better than a simple conservation of angular momentum argument that follows directly from the well-known spin-filtering properties of nanomagnets. It is important to keep in mind that the field of nanoscience has many similar examples of new phenomena that are not obtained from an ensemble average over a rigorously defined microscopic model. It is through a combination of both top-down and bottom-up approaches that one strives for a better understanding of the nanoscale world.

In this thesis, we are concerned with the magnetic properties of nanoscale conductors. In Chapter 2, we study the correlations between eigenvectors corresponding to different eigenvalues in a Random Matrix crossover ensemble. This would be relevant, for example, when calculating wavefunction correlations caused by turning on a magnetic field in a closed puddle of electrons trapped in a semiconductor quantum dot, or for a tiny metal grain. In Chapter 3, we explicitly look at tiny metal grains, and develop a Random Matrix crossover model to capture both the orbital and spin response to an external magnetic field in the presence of spin-orbit scattering. In Chapter 4 we look at the properties of a nanomagnet driven by a large current, and show that the solution requires a self-consistent treatment where the magnitude and direction of the spin-transfer torque acting on the nanomagnet to change the magnetization depends on the spin accumulation in the normal metal, which, in turn, depends on the magnetization of the nanomagnet. Finally, in Chapter 5, we examine nanomagnets at low temperature with

transparent contacts and show that mesoscopic effects give rise to conductance correlations. In particular, in the presence of spin-orbit scattering, coherent multiple scattering off impurities in the ferromagnet causes a mesoscopic anisotropic magnetoconductance fluctuation. This would be seen as a random and non-monotonic dependence of the conductance on the magnetization direction that is different for each sample, but reproducible for a given sample. At the end of the thesis we provide two appendices, the first with a generalization of the third-order torque calculation used in Chapter 4, and the second with some of the details used in calculating the diagrams and arriving at the results of Chapter 5.

What follows is a some background material in random matrix theory and crossover ensembles in Section 1.1, followed by Section 1.2, where we provide a brief introduction to the spectroscopy of small metal grains. In Section 1.3 we provide background material for the spin-transfer torque and in Section 1.4 we sketch the basics of diagrammatic perturbation theory and universal conductance fluctuations.

1.1 Random matrix theory and crossover ensembles

1.1.1 Wigner-Dyson ensembles

Random Matrix Theory (RMT) started out as a technique to calculate the statistical distribution of nuclear energy levels, but has since found applications in many very different branches of physics and mathematics (see, for example, Ref. [3] for the proceedings of a Summer school on the various applications of random matrices

in physics). For the purpose of this thesis, the key idea is that the statistical properties of physical systems with randomness or disorder can be determined by large random matrices which posses the same fundamental symmetries as the physical system. A particularly nice way to think of random matrix ensembles is through the framework of the Renormalization Group (RG) and universality. While at high energy, different physical systems might exhibit very different properties, they all flow (under the RG) to limited number of low-energy fixed points that depend only on certain discrete symmetries. The symmetry classes of Random Matrix Theory should be thought of as these low-energy fixed points.

The Wigner-Dyson universality classes of random matrices have been around since the early 1960s and have been the subject of much research. In this thesis, we are mostly concerned with the crossover between universality classes and therefore we only outline the basic properties. It is important to define two types of symmetries common in physical systems. The first is Time-Reversal Symmetry (TRS). A Hamiltonian with this symmetry will be invariant under the following operation

$$\begin{aligned} \mathcal{H} &= \tau \mathcal{H}^T \tau^{-1}, \\ \tau &= i\sigma_2 \otimes 1_N = \begin{pmatrix} 0 & 1 \\ -1 & 0 \end{pmatrix} \otimes 1_N. \end{aligned} \tag{1.1}$$

We now define a quaternion structure, or the from of a 2×2 matrix that is invariant under time-reversal. We have

$$Q = \begin{pmatrix} x & y \\ -y^* & x^* \end{pmatrix}. \tag{1.2}$$

The other important symmetry for the Wigner-Dyson class is Spin Rotation Symmetry (SRS), where in similar fashion, we can describe a Hamiltonian with this

symmetry as

$$\mathcal{H} = \sigma_j \mathcal{H} \sigma_j, \tag{1.3}$$

where σ_j means that the symmetry holds for each Pauli spin matrix. Given that any 2×2 spin block can be decomposed into the three Pauli matrices and the identity $\sigma_0 = 1_2$, we have that only Hamiltonians proportional to σ_0 in the spin sector will have the Spin Rotation Symmetry.

At this point it is convenient to introduce some notation. We define the following letters to represent $N \times N$ matrices

$$\begin{aligned} h &= h^\dagger, \quad \text{hermitian, complex} \\ a &= -a^T, \quad \text{antisymmetric, complex} \\ b &= b^* = -b^T, \quad \text{antisymmetric, real} \\ s &= s^* = s^T, \quad \text{symmetric, real} \end{aligned}$$

and any subscripts, for example, a_1, a_2 will be used to represent different realizations of these antisymmetric random matrices. Given that these classes are low energy fixed points, the exact form of the probability distribution for the elements is not important, but they are conventionally taken from Gaussian probability distributions with zero mean and variances chosen such that each element of the total Hamiltonian $\mathcal{H}$ has the same variance of $4N\delta^2/\pi^2$, where δ is the mean level spacing of the physical system. In addition we define

$$q = s + i \sum_{j=1}^{3} b_j \sigma_j,$$

which is just another way of writing a $2N \times 2N$ matrix whose spin sector is of the form Q in Eq. (1.2) above.

Armed with this notation, we are now define the three Wigner-Dyson classes. The Gaussian Orthogonal Ensemble (GOE) has both spin rotation symmetry and time reversal symmetry. Requiring SRS means that the spin structure is proportional to σ_0, and TRS means that the spin structure must also be of the form Q in Eq. (1.2) above, with SRS imposing the additional constraints that $y = 0$ and $x \in \Re$ (see Eq. (1.2) above). Hermiticity implies that $x = s$, so we have that the Wigner-Dyson GOE class is given by $\mathcal{H} = s \otimes \sigma_0$ which has both TRS and SRS. Notice that $\mathcal{H} \rightarrow O\mathcal{H}O^{-1}$, where O is an orthogonal matrix, leaves the probability distribution of $\mathcal{H}$ invariant, and hence the name Gaussian Orthogonal Ensemble.

Preserving TRS but breaking SRS gives rise to the Gaussian Symplectic Ensemble (GSE). This is just a matrix of the form $\mathcal{H} = q$ as defined above. This has been constructed to preserve time reversal symmetry. If we define a Symplectic matrix (Sp) to be a unitary matrix with elements given by quaternions of the form Q, then $\mathcal{H} \rightarrow (Sp)\mathcal{H}(Sp)^{-1}$ preserves the probability distribution.

Finally we consider the Gaussian Unitary Ensemble (GUE) where TRS is broken. Once TRS is broken, the RG fixed points with and without SRS coincide, although one can explicitly construct a Hamiltonian preserving SRS by considering two independent blocks of GUE matrices. The condition of Hermiticity requires that $\mathcal{H} = s + ib$, and the probability is invariant under unitary transformations. Table 1.1 summarizes the Wigner-Dyson class.

Many physical systems have been modeled using the Wigner Dyson classes. To provide just one example relevant to this thesis, about four decades ago, Gor'kov and Eliashberg [4] used Random Matrix Theory to study the electronic properties of small metal grains. The main idea is that electrons inside a metal grain behave like particle-in-a-box states trapped in a random confining potential. In the absence

Table 1.1: Classification of symmetry classes for Wigner-Dyson standard class. The symmetry classes are defined in terms of the presence or absence of time-reversal symmetry (TRS) and spin-rotation invariance (SRS). To provide a connection to other Random Matrix literature, we also list the corresponding classification using the Cartan notation.

Name	TRS	SRS	$\mathcal{H}$	Cartan
WD GOE	Yes	Yes	$s \otimes \sigma_0$	AI
WD GUE	No	-	$s + ib$	A
WD GSE	Yes	No	q	AII

of a magnetic field, both TRS and SRS are present and one might model the energy levels in the metal grain by eigenvalues of the GOE random matrix.

Of course, such a bold ansatz requires much more motivation to be convincing; afterall, as defined above, the random matrix model in the limit of $N \to \infty$ has only one free parameter which is the variance of the matrix elements (these are related to the mean level spacing as $4N\delta^2/\pi^2$), whereas the problem of electron diffusion in a disordered metal grain has several energy scales. Following arguments similar to Ref. [5], we can quantify the various energy scales in the metal grain as follows. We are interested in the diffusive regime, where the mean free path $\ell \ll L$, where L is the size of the dot. For a given Fermi energy $E_F = (1/2)mv_F^2$, where m is the electron mass and v_F is the Fermi velocity, this sets constraints on the strength of the impurity potential defined by a scattering rate $\hbar/\tau$, where $\hbar$ is the reduced Planck constant, and $\ell = v_F\tau$. We can define a Thouless energy E_T

which sets the energy scale for an electron to diffuse through the grain. This was first introduced in Ref. [6, 7] to characterize the sensitivity of levels to changing of boundary conditions. Equivalently, we can define $t_L = \hbar/E_T$ as the time to diffuse a distance L. We can calculate t_L by assuming that a random walk with t_L/τ steps moving a distance of ℓ at each step travels a distance of $L = \sqrt{t_L/\tau}\ell$. From this we get that $E_T = \hbar v_F^2 \tau / L^2$, and that $E_F \gg \hbar/\tau \gg E_T$.

To make the connection with Random Matrix Theory, we need to further assume that the dimensionless conductance $g \gg 1$, where $g = E_T/\delta$, and we identify the mean level spacing δ with that of the random matrix model. For the metal grain, this last condition implies that we are interested in the physics related to the discreteness of the energy spectrum caused by the electrons being confined to a grain of finite size L. For the random matrix model, this condition implies that we are only interested in a region having a flat density of states, which corresponds to an energy window much smaller than the width of the Wigner semi-circle, or equivalently to the limit $N \to \infty$. We note in passing that this correspondence between the eigenvalues of the random matrix model and the spectrum of energy levels in a diffusive metal grain has been rigorously proved by Efetov using a field theoretic technique that he calls a zero-dimensional supermatrix σ-model (See Ref. [8] for details).

1.1.2 Transition between ensembles

Thus far we have looked at pure RMT ensembles. In this thesis we are more concerned with the crossover between ensembles. In the preceding section we argued that, for example, the GOE ensemble preserved time reversal symmetry, while the GUE had broken TRS. For a physical system this corresponds to turning

on a magnetic field. In reality, a weak magnetic field does not immediately break time-reversal symmetry completely. A discussion of crossover ensembles was first put forward in Ref. [9], where they considered a model (using the notation of the previous section) of the form

$$\mathcal{H} = s + i\alpha b, \tag{1.4}$$

where the limits of $\alpha = 0(1)$ correspond to the GOE (GUE) respectively. In this case α corresponds to the magnetic flux Φ through the system. The first natural question is the relation between the flux and crossover parameter. From a simple perturbation theory estimate, one notices that treating α as a perturbation causes and energy shift $\Delta E \sim N\alpha^2\delta$. One can also estimate that the magnetic field necessary to give an energy shift of $\Delta E \sim \delta$ requires an accumulated flux $\sqrt{E_T/\delta}(\Phi/\Phi_0) \sim 1$, where $\Phi_0 = h/e$ is the flux quantum and we have assumed a random walk of E_T/δ time steps picking up a phase of Φ/Φ_O at each step. Combining these two estimates we find that

$$N\alpha^2 \sim \frac{E_T}{\delta}\left(\frac{\Phi}{\Phi_0}\right). \tag{1.5}$$

.

This formalism is quite general and can be readily generalized to model different systems that continuously interpolated between pure ensembles. For example, one could use the cross-over between GOE and GSE, to model a system where spin-orbit scattering breaks spin rotational symmetry (See Section 1.2), or the interpolation between two copies of a GUE matrix to one GUE matrix of twice the size can be used to model two quantum dots of roughly equal size coupled through a point contact. Turning off the coupling corresponds to the two independent GUEs, while strong coupling corresponds to a single GUE, and the crossover represents intermediate coupling (See Refs.[10, 11] for more details).

While in the previous section, we were mostly concerned with the connection between the eigenvalues of the random matrix model and the energy levels of the physical system, one can ask if the eigenvectors in a similar fashion correspond to wavefunctions. One problem with this is that one can show that such an identification would not be gauge invariant and that the correspondence could be broken by choosing a different gauge. However, with this caveat in mind, so long as one looks only at gauge invariant quantities, one can make the following identification [12]

$$V^{1/2}\psi_\mu(\mathbf{r}_i) \leftrightarrow N^{1/2}v_\mu(i), \tag{1.6}$$

where V is the volume, $\psi_\mu(\mathbf{r}_i)$ is the wavefunction at the position $\mathbf{r}_i$ corresponding to the energy ϵ_μ and $v_\mu(i)$ is the i-th component of the eigenvector $\boldsymbol{v}$.

Having introduced the crossover ensembles, and identified the correspondence with physical systems, we now discuss an important observation – There are some quantities that are zero in the pure ensembles, but non-zero in the cross-over. In particular, we consider long-range wavefunction correlations.

In the pure ensembles one can write the probability distribution

$$P(\boldsymbol{v}_1, \boldsymbol{v}_2, \ldots, \boldsymbol{v}_n) \propto \delta(\boldsymbol{v}_1^\dagger \boldsymbol{v}_1 - 1)\delta(\boldsymbol{v}_2^\dagger \boldsymbol{v}_2 - 1)\ldots\delta(\boldsymbol{v}_1^\dagger \boldsymbol{v}_2)\ldots. \tag{1.7}$$

For any finite subset of variables, one can integrate out the remaining variables to find that in the limit of large N,

$$\begin{aligned} P(v_\mu(i), v_\nu(j), \ldots) \quad &\sim \exp[\frac{-|v_\mu(i)|^2}{2\beta N}]\exp[\frac{-|v_\nu(j)|^2}{2\beta N}]\ldots, \\ &\sim P(v_\mu(i))P(v_\nu(j))\ldots, \end{aligned} \tag{1.8}$$

where $\beta = 1, 2$ or 4 for the GOE, GUE and GSE ensembles. The factorization of the probability distributions shows that there is no wavefunction correlations in the pure ensembles.

By contrast, in the crossover ensembles, there are long-range correlations of wavefunctions (both for the same wavefunction [12, 13] and for different wavefunctions [Chapter 2]). We have that this long-range order vanishes in the basic ensembles but is finite in the crossover. For the GOE-GUE crossover, one can study this by considering an orthogonal invariant defined as

$$\rho_{\mu\nu} = \rho_{\nu\mu} = \boldsymbol{v}_\mu^{\mathrm{T}} \boldsymbol{v}_\nu, \quad \mu, \nu = 1, \ldots, n, \tag{1.9}$$

where the superscript T denotes transposition. Notice that the orthogonality of wavefunctions requires that the phase rigidity, defined as $\langle |\rho_{\mu\mu}|^2 \rangle$, has well defined values for the pure ensembles, viz. $|\rho|^2 = 1$ for GOE and $|\rho|^2 = 0$ for GUE. In the crossover, this parameter does not taken on a single value but fluctuates [12]. The same observation was made by Ref. [13] when they noticed that the while joint distribution of $P(|\psi_\mu(\mathbf{r}_1)|^2, |\psi_\mu(\mathbf{r}_2)|^2) = P(|\psi_\mu(\mathbf{r}_1)|^2) P(|\psi_\mu(\mathbf{r}_2)|^2)$ for the basic ensembles, that it no longer factorized in the crossover, which suggested long range wavefunction correlations. Our work in Chapter 2 shows that such long-range correlations extends to off-diagonal $\rho_{\mu\nu}$ as well.

However, for the purpose of this introduction, we are mostly concerned with the physical consequences of these correlations. One physical consequence put forward by Refs. [12, 14] was to consider a tiny perturbation, for example, either a global random magnetic field or several localized scatters. If one calculates the level velocity, defined as the derivative of an energy level with respect to the amplitude of the perturbation, for the pure ensembles one would get Gaussian distributed values. However, since the distribution of the level velocities is related to the distribution of phase rigidity [12]. This results in a non-Gaussian distribution in the crossover. Another consequence of this correlations can be observed in conductance peak-height correlations in Coulomb blockaded quantum dots. In Ref. [15], we addressed

how wavefunction correlations causes peak-height correlations in the conductance of quantum dots. Much larger correlations have been seen experimentally, and our paper provided the intrinsic correlations caused only by the statistical properties of breaking of time reversal symmetry by a magnetic field, which would continue to be seen even in the absence of other mechanisms.

Another consequence of the wavefunction correlations was seen in the work of Ref. [16] where studying a GOE-GSE crossover (with the breaking of SRS with spin-orbit scattering), found that while g-factors had well defined values in both the pure ensembles, they had fluctuating values in the crossover. In Chapter 3 we extend this work to include the orbital contribution to the g-factors, but we also calculate the correlation between neighboring g-factors that depends on the correlation between neighboring wavefunctions. By generalizing the ideas of Chapter 2 to the GOE-GSE crossover, we are able to calculate both the off-diagonal wavefunction distribution as well as its effects on observables like the correlator $\langle g_{\mu+1}^2 g_\mu^2 \rangle$.

Finally, in Ref. [11], we were able to use the long-range wavefunction correlations in crossover ensembles to describe the interactions in the double dot model discussed above. Using a Renormalization Group method, we found both that the Universal Hamiltonian (see Ref. [17]) was the low energy fixed point and we also verified that the instability caused by large interactions occurred at precisely the same strength in mesoscopic system as they did in bulk systems.

1.2 Spectroscopy of energy levels in metal grains

1.2.1 Transport through discrete electronic energy levels

One feature of the closed systems that we have been studying so far is that the confinement causes the system to have discrete energy levels. By weakly connecting such systems to external leads using tunnel junctions, it is possible to make low temperature transport measurements through the grain that reveal steps in the current-voltage profile that are caused by transport through individual electronic states of the nanoparticle. The first such experiments were done by Ralph, Black and Tinkham [18], where they were able to fabricate nanoscale Al particles and through low temperature transport measurements, were able to perform spectroscopy measurements of these discrete energy levels.

Here we sketch out only the basic principles involved in this spectroscopy of energy levels in metal grains, (see Ref. [19] for a detailed review). The basic principle is captured in the cartoon shown in Fig. 1.1. The metal grain has discrete energy levels with thermal broadening being much less than the distance between levels. In this case, one can increase the bias voltage between the left and right reservoirs and as the window of voltage difference sweeps past an energy level, this opens up a conductance channel, causing a step-like increase in the conductance or a peak in the differential conductance dI/dV. Using this method, the differential conductance provides a direct probe of the energy levels of the ultra-small metallic grain. Applying a magnetic field can Zeeman split these energy levels, as can be seen in actual experimental data taken from Ref. [20] and shown in Fig. 1.2.

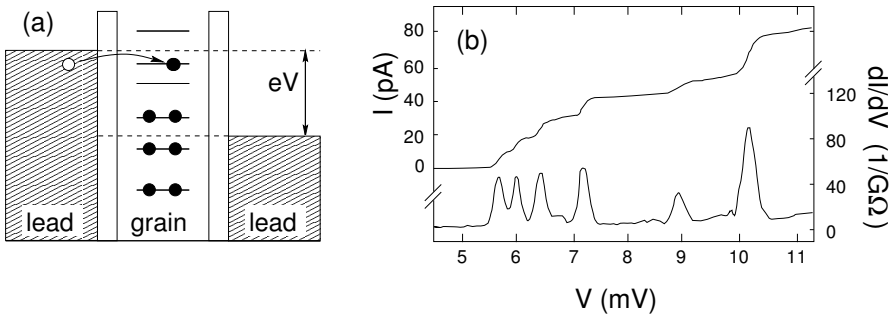

Figure 1.1: (a) Cartoon of transport measurement in metal grain. The number of available transport channels corresponds to the number of discrete energy levles in the bias voltage window. (b) The current and differential conductance as functions of bias voltage V for one of the grains studied by Ref. [18]. Beyond the Coulomb-blockade threshold one sees steps in the current and peaks in the conductance reflecting the metal grain's discrete eigenspectrum. Figure taken from Ref. [19], available online at http://arxiv.org/format/cond-mat/0101019.

1.2.2 Verification of the random matrix model

Although the 1965 random matrix model of Gorkov and Eliashberg [4] was widely believed to be applicable to metal nanoparticles, no verification was possible until the recent experimental ability to measure the energy levels directly as was discussed in previous section. In the experiments of Salinas *et al.* [21], they were able to dope Al nanoparticles – which does not have much spin-orbit scattering – with with varying amounts of Au, which being a heavier element has a large amount of spin-orbit scattering. In bulk samples, spin-orbit interaction causes only a small effect on g-factors, while in the experiments in nanoparticles, g-factors vary from the free electron value of 2 to about 0.1 for Au samples [20, 21, 22, 23, 24].

The work in Chapter 3 builds on earlier theoretical work by Matveev, Glazman and Larkin [25] and by Brouwer, Waintal and Halperin [16]. As described in Sec-

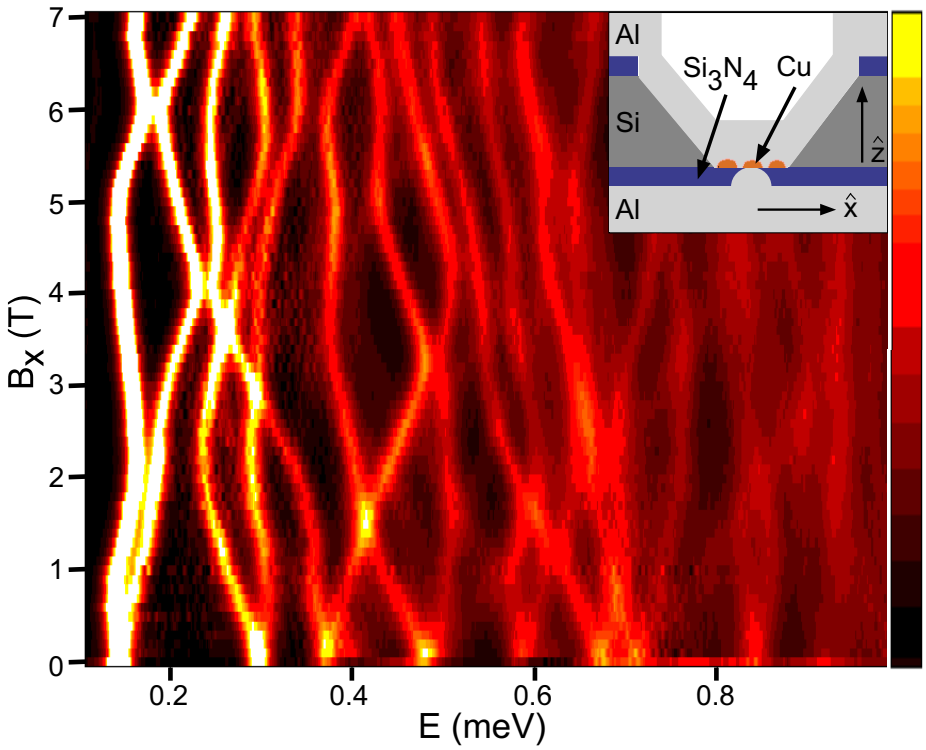

Figure 1.2: The dependence of energy levels of a copper nanoparticle to an applied magnetic field. Main panel: A plot of the differential conductance (dI/dV) versus energy (E) as a function of magnetic field (B_x). White corresponds to a conductance of 2 mS, and black to zero. Values between 2 mS and the maximum conductance of 3 mS are also set to white. The inset shows a sample schematic. A small hole in a Si_3N_4 membrane is used to make electrical contact to a single copper nanoparticle. Al_2O_3 tunnel junctions (not shown) lie between the nanoparticle and aluminum electrodes. Figure taken from Ref. [20], available online at http://arxiv.org/format/cond-mat/0206423.

tion 1.1.2, the breaking of spin-rotational symmetry by spin-orbit scattering causes a transition from GOE to GSE random matrix ensembles. Following Ref. [16] one can define a cross-over Hamiltonian of the form

$$\mathcal{H}(\lambda) = \mathcal{H}_{\mathrm{GOE}} + \frac{\lambda}{\sqrt{N}}\mathcal{H}_{\mathrm{GSE}} \tag{1.10}$$

where one can relate the crossover parameter λ to the spin-orbit scattering time τ_{so} by comparing the spin-orbit energy $\hbar/\tau_{so}$ to the random matrix shift in energy $N\lambda^2\delta$ to get that $\lambda \sim (\tau_{so}\delta)^{-1/2}$. While spin no longer commutes with the Hamiltonian, there is nonetheless time-reversal symmetry preserved throughout the crossover. The addition of a magnetic field breaks this degeneracy between Kramers' doublets and the g-factor is understood to be the derivative of the difference in energy between the Kramers pairs with respect to the magnetic field. Reference [16] only considered the spin contribution to the g-factor, but noticed that because of mesoscopic fluctuations, the energy change in a magnetic field was highly anisotropic requiring the use of a g-tensor to analyze the magnetic response. On the other hand, while Ref. [25] only looked at the isotropic response, they calculated the orbital contribution to the g-factor in the limit of large spin-orbit coupling. In Chapter 3, we introduce a random matrix model that accounts for both orbital and spin contributions to the g-factor which we solve for both weak and strong spin-orbit scattering. In addition, we calculate other statistical properties including the g-tensor correlations for neighbouring energy levels as well as avoided crossing energies. The calculations shown in Chapter 3 depend on only two parameters (the spin-orbit strength λ and the orbital coupling term η) each of which can be measured independently in the experiments. For a given sample, once these parameters have been determined, the other predictions of the theory like distribution of avoided crossing energies or correlations between neighboring

g-factors can be compared to experiments without any adjustable parameters.

1.3 Current-induced transverse spin-wave instabilities

1.3.1 Ferromagnetism and the spin-transfer torque

Magnetism has been known since ancient times. The ancient Greeks knew about the magnetic properties of lodestone and that these effects disappeared when the material was heated beyond a critical temperature. It was not until the age of quantum mechanics that an adequate understanding was possible. In this thesis we are concerned mostly with ferromagnets like Cobalt, so named because their magnetic properties are similar to Iron (Ferrus). A ferromagnet can be considered as a state of broken symmetry between up-spins and down-spins as has been shown in the cartoon in Fig. 1.3. For the most part, we will not be interested in the microscopic details or band properties of the different spin-species, but rather assume that the magnet has an internal magnetization that depends both on the shape anisotropy and an external applied magnetic field. In this section and in Chapter 4, we will be concerned with the spin-torque effects discussed earlier which can be seen at room temperature and has great potential for technological application. In Section 1.4 and in Chapter 5, we will be interested in the same type of nanomagnets, but this time at sub-Kelvin temperatures and studying quantum coherent effects that would be washed away at room temperature.

Over the past few years there has been much theoretical and experimental attention on understanding the spin-transfer torque and how it plays out in struc-

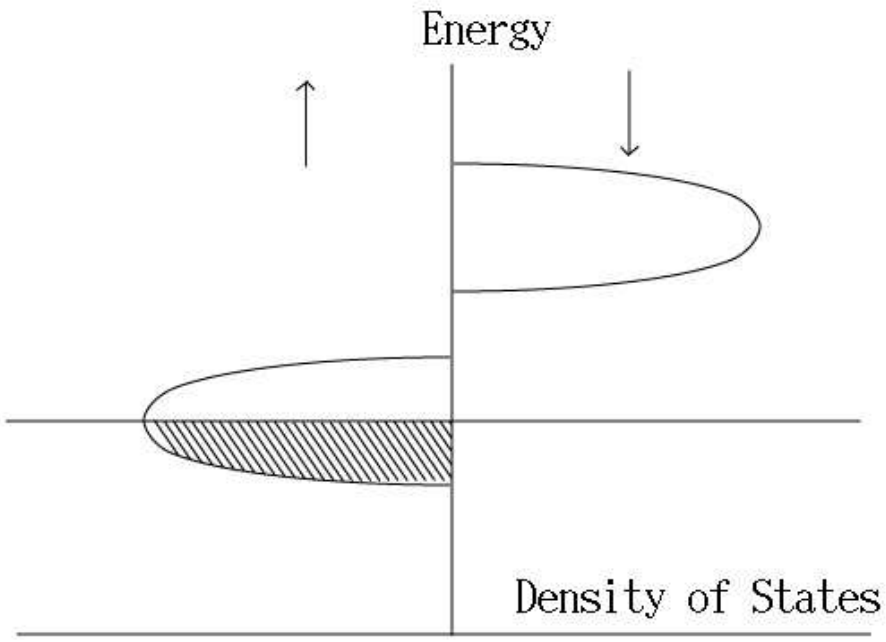

Figure 1.3: Cartoon of a ferromagnet as a state with broken symmetry between majority and minority spins. The shaded region represents states occupied below the Fermi energy.

tures made of layers of normal metals and ferromagnets. A common geometry is to have a heterostructure comprising a thick ferromagnet, a normal metal spacer and a thin free layer of ferromagnet. The thick (or fixed) layer acts as a spin-filter. This can be understood from the cartoon in Fig. 1.3 since at the interface between the normal metal and the ferromagnet, one spin species would have a greater density of states overlap and hence greater transmission. Without loss of generality, this can be thought of as an increase in the spin-accumulation in the adjacent normal layer spacer in a direction aligned to the magnetization of the fixed layer. Changing the direction of current flow reverses the direction of the spin accumulation causing the spins in the normal metal spacer to be anti-aligned with the fixed layer magnetization. In a certain approximation, one can then forget about the thick layer and examine the effects of this change in direction of spin accumulation on the free ferromagnet keeping in mind that by simple two channel circuit theory arguments, the device resistance will be lower when the free layer and fixed layer magnetizations are parallel and higher when they are anti-parallel.

It is now almost a decade since Slonczewski [1] proposed that when a spin-polarized current passes through a ferromagnet it transfers any transverse component of its spin angular momentum to the ferromagnet. This spin-transfer torque is caused by the exchange interaction between the s orbitals of the electrons in the normal metal and the d electron orbitals in the ferromagnet. Slonczewski calculated the form of the torque using semiclassical WKB wavefunctions. In the same year Berger [2] found a similar result using a different semiclassical method. As alluded to earlier, if one treats magnetization of the ferromagnet semiclassically, then just by considering the conservation of spin angular momentum one can arrive at the required form of the spin-transfer torque [26]. For a thin ferromagnet,

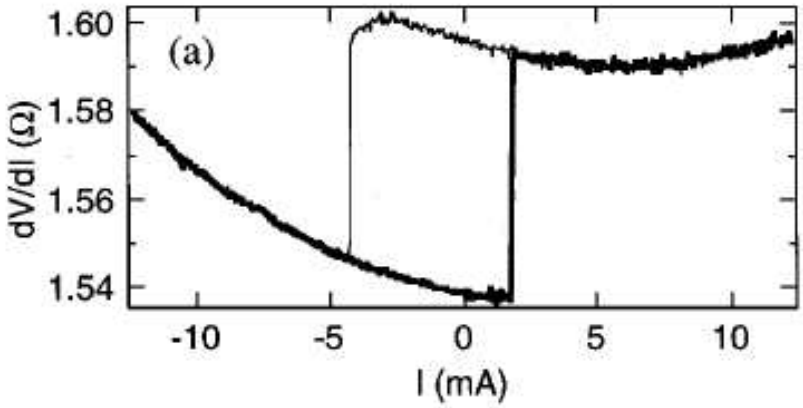

Figure 1.4: dV/dI of a nanopillar spin-transfer device as a function of the applied current through the device. The current is defined as positive when the spin-polarized electrons are flowing from the nanomagnet to the thick ferromagnet film. Figure taken from Ref. [28].

the torque is proportional to the component of spin current transverse to the ferromagnet magnetization. This torque causes the free layer to align itself with the spin accumulation in the normal metal spacer. Therefore, by switching the direction of the current, one can move from a high resistance to low resistance state, a characteristic well suited to making a magnetic memory device. The experimental observation of hysteretic switching [27] confirmed the spin-transfer effect. Shown in Fig. 1.4 is the experimental data of Ref. [28] showing clearly the current driven magnetization reversal.

1.3.2 Single ferromagnetic layers

In Chapter 4 we are mostly concerned with a single ferromagnetic layer sandwiched between two normal metal leads. A few years ago, Polianski and Brouwer [29]

were the first to demonstrate that spin-transfer effects were important even for an unpolarized current. The key idea was that since typical devices have a transverse dimension that is of the same order as the spin-diffusion length, one must take into account electron diffusion along this transverse direction. If the source and drain contacts are asymmetric, even an unpolarized current applied perpendicular to the plane of a thin ferromagnet, can excite a transverse spin-wave instability where one part of the ferromagnet acts as the polarizer for another part of the same ferromagnet.

For one direction of current, the torque acts against intrinsic damping to excite the spin-wave, while for the opposite current direction, the spin-torque enhances damping thereby stabilizing the system. Stiles et al. [30] later showed that for sufficiently large ferromagnet thickness, even symmetric junctions are unstable to spin-waves, but in this case, these are longitudinal spin-waves that are excited at higher currents than the transverse spin-waves predicted in Ref. [29]. Both these calculations show that important qualitative features are missed when the ferromagnet is modeled as a single domain.

The mechanism for the spin-wave instability found in Ref. [29] is as follows: The ferromagnet acts as a spin-filter for electrical current passing through the magnet, leading to a spin accumulation that depends on the direction of the current (as discussed above). However, by allowing for the possibility of non-uniform modes in the direction transverse to current flow, one finds that there is a spin-wave instability that depends both on the stiffness of the nanomagnet and on the spin-diffusion length of the normal metal ℓ_{sf}. By performing a linear stability analysis [29] one finds that the instability occurs when the current induced enhancement of a spin-wave amplitude is greater than the intrinsic damping in the ferromagnet. One

can thus derive a critical current I_c for the onset of the spin-wave instability. Recent experiments [31] on single domains have verified these theoretical predictions finding spin-wave instabilities for only one direction of the current and for only asymmetric junctions. The experimental results are shown in Fig. 1.5. Note that there are dips in the resistance, which is consistent with transverse spin-waves, as will be discussed in Chapter. 4.

Having discovered this spin-wave instability for a single ferromagnetic layers with an unpolarized current, it is a natural question to address what happens for larger currents beyond I_c. It is the goal of Chapter 4 to examine in detail the dynamics of the spin-wave beyond the instability. While for simplicity we focus on the case of single-layers, in light of the work of Ref. [32], these dynamics are relevant also to the case of tri-layers and heterojunctions with possible applications to tunable Giga-Hertz range resonators. It is important to emphasize that an important part of the calculation in Chapter 4, is that the spin-transfer torque is calculated self-consistently. This is important since the magnetization dynamics is determined by the spin-transfer torque which depends on the spin accumulation in the normal metal, this in turn, depends on the precise magnetization profile of the ferromagnet. Calculating spin and charge chemical potentials to second order in perturbation theory, allows us to calculate the third-order Slonczewski torque which provides us with detailed information about the magnetization dynamics including the amplitude of the spin-wave mode and the corresponding decrease in junction resistance.

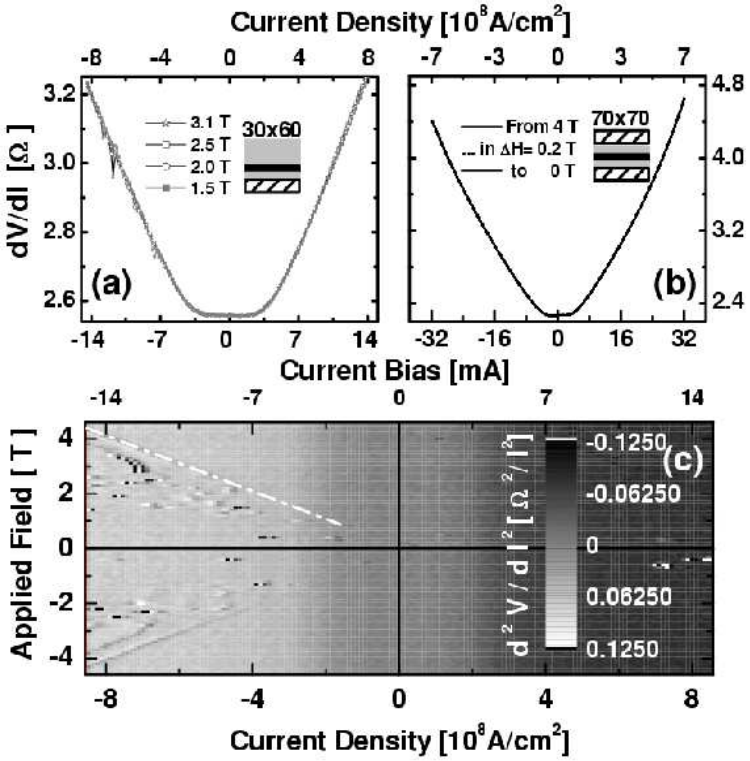

Figure 1.5: dV/dI vs I at constant fields. (a) asymmetric junction of dimensions 30 nm $\times$ 60 nm, $t \approx 8$ nm. For sufficiently large fields, dips are observed at negative bias only. (b) Symmetric junction of dimensions 70 nm $\times$ 70 nm, $t \approx$ 10 nm. Current-voltage curves at different field values overlap fully. (c) Phase diagram for current induced excitations in single layer junctions; same junction as in (a). d^2V/dI^2 is plotted on a grayscale. The white dash-dotted line indicates the boundary for excitations. Figure taken from Ref. [31] and available online at http://arxiv.org/format/cond-mat/0403367.

1.3.3 Adiabatic boundary conditions

In Chapter 4, we make use of the adiabatic approximation used previously by Refs. [29, 33, 34]. Here we derive the boundary conditions that relate the spin and charge currents at the boundary to the chemical potentials using interface conductivities. We can define interface conductivities by considering the scattering matrix for the boundary, in particular, we have $g_{\sigma\sigma'} = \sum_{nm}[\delta_{nm} - r^{\sigma}_{nm}(r^{\sigma'}_{nm})^*]$ and $t^{\sigma\sigma'} = \sum_{nm} t^{\sigma}_{nm}(t^{\sigma'}_{nm})^*$ where the r_{nm} and t_{nm} are reflection and transmission coefficients of the scattering matrix, and $\sigma, \sigma' \in [\uparrow, \downarrow]$ represent the majority and minority spins which are parallel and antiparallel to the ferromagnet magnetization $\hat{\mathbf{m}}$. It is convenient to define the following linear combinations: $g_{\uparrow\downarrow} = g_1 - ig_2$ and $g_{\pm} = (g_{\uparrow\uparrow} \pm g_{\downarrow\downarrow})/2$. One can show that for any interface, $g_1 > g_+$. This is done by noticing that this condition is equivalent to the off-diagonal conductivities being larger than the diagonal ones, i.e. $g_{\uparrow\downarrow} + g_{\downarrow\uparrow} > g_{\uparrow\uparrow} + g_{\downarrow\downarrow}$, which can be obtained from the definition of $g_{\sigma,\sigma'}$ and the property $|r^{\uparrow} - r^{\downarrow}|^2 > 0$. It also follows from their definitions that $g_+ > g_-$. We now wish to decompose the charge and spin currents into terms that depend on the local magnetization and the interface conductivities. This can be done by projecting the charge and spin chemical potential onto a basis aligned with the local magnetization

$$\begin{aligned} j/2 &= g_{\uparrow\uparrow}(\sigma_0 + \mathbf{m}\cdot\boldsymbol{\sigma})(\Delta\mu_c\sigma_0 + \Delta\boldsymbol{\mu}_s\cdot\boldsymbol{\sigma})(\sigma_0 + \mathbf{m}\cdot\boldsymbol{\sigma})/4 \\ &\quad + g_{\downarrow\downarrow}(\sigma_0 - \mathbf{m}\cdot\boldsymbol{\sigma})(\Delta\mu_c\sigma_0 + \Delta\boldsymbol{\mu}_s\cdot\boldsymbol{\sigma})(\sigma_0 - \mathbf{m}\cdot\boldsymbol{\sigma})/4 \\ &\quad + g_{\uparrow\downarrow}(\sigma_0 + \mathbf{m}\cdot\boldsymbol{\sigma})(\Delta\mu_c\sigma_0 + \Delta\boldsymbol{\mu}_s\cdot\boldsymbol{\sigma})(\sigma_0 - \mathbf{m}\cdot\boldsymbol{\sigma})/4 \\ &\quad + g_{\downarrow\uparrow}(\sigma_0 - \mathbf{m}\cdot\boldsymbol{\sigma})(\Delta\mu_c\sigma_0 + \Delta\boldsymbol{\mu}_s\cdot\boldsymbol{\sigma})(\sigma_0 + \mathbf{m}\cdot\boldsymbol{\sigma})/4, \end{aligned} \tag{1.11}$$

where σ_0 is the 2×2 identity matrix and $\boldsymbol{\sigma} = (\sigma_x, \sigma_y, \sigma_z)$ is the vector of Pauli matrices. The reason for calculating $j/2$ is to be consistent with the definitions of

interface conductivities used in Chapter 4. After some algebra, one arrives at

$$\begin{aligned} j/2 &= (g_+\Delta\mu_c + g_-\mathbf{m}\cdot\Delta\boldsymbol{\mu}_s)\sigma_0 + ([g_-\Delta\mu_c + g_+\mathbf{m}\cdot\Delta\boldsymbol{\mu}_s]\mathbf{m} \\ &\quad - g_1[(\Delta\boldsymbol{\mu}_s\times\mathbf{m})\times\mathbf{m}] - g_2[(\Delta\boldsymbol{\mu}_s\times\mathbf{m})])\cdot\boldsymbol{\sigma} \end{aligned} \tag{1.12}$$

As was noticed by Tserkovnyak et al [34], in general there is an additional current term dependent on the time derivative of the magnetization. We have a contribution of the form $j_p = -g_1\hbar\partial_t\mathbf{m}\times\mathbf{m} - g_2\hbar\partial_t\mathbf{m}$. We also note that for the geometry considered in Chapter 4, we have the property that the charge current and parallel components of the spin current are continuous at the interface, and by assuming that the two ferromagnet-normal-metal interfaces are identical, we can replace $\Delta\mu_c$ with $\mu_c(0)/2$. By assuming that the perpendicular component of the spin-chemical potential is zero inside the ferromagnet, we have that $\Delta\boldsymbol{\mu}_s = \boldsymbol{\mu}_s(0)$. Putting this together, we get

$$\begin{aligned} j + j_p &= (g_+\mu_c(0) + g_-\mathbf{m}\cdot\boldsymbol{\mu}_s(0))\sigma_0 + ([g_-\mu_c(0) + g_+\mathbf{m}\cdot\boldsymbol{\mu}_s(0)]\mathbf{m} \\ &\quad - g_1[(2\boldsymbol{\mu}_s(0)\times\mathbf{m} + \hbar\dot{\mathbf{m}})\times\mathbf{m}] \\ &\quad - g_2[(2\boldsymbol{\mu}_s(0)\times\mathbf{m} + \hbar\dot{\mathbf{m}})])\cdot\boldsymbol{\sigma}. \end{aligned} \tag{1.13}$$

To compare this with the Eq. (4.3) in Chapter 4, we explicitly define $j_x = (\sigma/e)\partial_x\mu_\mathrm{c}$ and $\mathbf{j}_\mathrm{s} = -(\hbar\sigma/2e^2)\partial_x\boldsymbol{\mu}_\mathrm{s}$ as the charge and spin currents to obtain

$$\begin{aligned} j_x(0) &= \frac{1}{e}\left[g_+\mu_\mathrm{c}(0) + g_-\mathbf{m}\cdot\boldsymbol{\mu}_\mathrm{s}(0)\right], \\ \mathbf{j}_\mathrm{s}(0) &= -\frac{\hbar}{2e^2}\left(g_-\mu_\mathrm{c}(0) + g_+\mathbf{m}\cdot\boldsymbol{\mu}_\mathrm{s}(0)\right)\mathbf{m} \\ &\quad + \frac{\hbar}{2e^2}g_1\left(2\boldsymbol{\mu}_\mathrm{s}(0)\times\mathbf{m} + \hbar\dot{\mathbf{m}}\right)\times\mathbf{m} \\ &\quad + \frac{\hbar}{2e^2}g_2\left(2\boldsymbol{\mu}_\mathrm{s}(0)\times\mathbf{m} + \hbar\dot{\mathbf{m}}\right). \end{aligned} \tag{1.14}$$

This equation for the boundary condition at the interface between the normal metal and ferromagnet is the starting point for the calculations in Chapter 4.

1.4 Diagrammatic perturbation theory and conductance fluctuations

Diagrammatic perturbation theory is now a well established technique. At its heart it is a field-theoretic method of tackling the quantum many-body problem by representing physical quantities as a purturbative expansion that is conveniently expressed in pictorial form as Feynmann diagrams. Oftentimes a subset of this perturbative expansion is identified as a geometric series and can be summed exactly to all orders. If there exists good physical reasons why (order-by-order) other diagrams in the expansion can be neglected, or sometimes by sheer luck, then this method of expanding a quantity in Feynmann diagrams and summing a subset of the diagrams gives an accurate way to calculate physical phenomena. There are several good textbooks on diagrammatic techniques including Refs.[35, 36, 37], and for the purpose of this introduction we just mention that the two important signatures of quantum coherent transport viz. weak localization and universal conductance fluctuations were each first seen experimentally and then soon afterward calculated theoretically using diagrammatic methods. The focus of Chapter 5 is mostly on universal conductance fluctuations which is the phenomena that the conductance of any metallic sample viewed as a function of chemical potential, magnetic field, or impurity configuration has a variance of the order of e^2/h independent of the specific sample properties, such as impurity configuration, material, shape, or method of preparation.

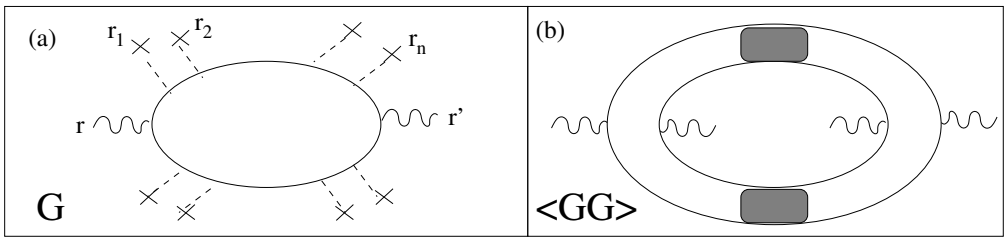

Figure 1.6: (a) Diagram for the conductance G before impurity averaging. Electrons propagate from $\mathbf{r}$ to $\mathbf{r}'$ while being scattered by impurities located at $\mathbf{r}_1, \mathbf{r}_2, \cdots \mathbf{r}_n$ which are represented by the dashed lines and crosses. (b) Diagram for the impurity averaged variance of conductance $\langle GG \rangle$, where the shaded area represents impurity averages involving both classical Diffusion modes and the Cooperon quantum corrections.

Theoretically, the problem was first solved by two groups, Altshuler [38] and by Lee and Stone [39]. The details of the calculation were given by Lee, Stone and Fukuyama [40] and form the basis of our calculation in Chapter 5. Using the Kubo formula that relates the linear response expectation value of any operator to an equilibrium expectation value of the commutator of that operator and the perturbation Hamiltonian, one finds that the conductance is given by [37]

$$G = \lim_{\omega \to 0} \frac{e^2}{\omega} \int dt \exp^{i\omega t} \theta(t) \langle [\hat{I}(t), \hat{I}(0)] \rangle, \tag{1.15}$$

where $\hat{I}$ is the current through an arbitrary cross-section, and $\theta(t)$ is the step function. This formulation connects the linear response conductance to the retarded current-current correlator which is shown in the diagrammatic language in Fig. 1.6.

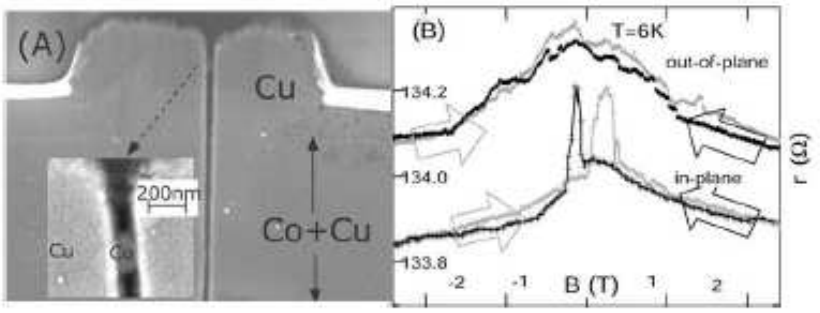

Figure 1.7: A: Image of a typical sample. B: Out-of-plane and in-plane magnetoresistance. Figure taken from Ref. [41] and available online at http://arxiv.org/format/cond-mat/0509452.

1.4.1 Universal conductance fluctuations in ferromagnets

In Chapter 5, we turn our attention to ferromagnets. The very recent experiments of Ref. [41] done at low temperatures on ferromagnets with good contacts have begun to see quantum interference effects. Shown in Fig. 1.7 and Fig. 1.8 is the set-up and results from these experiments. Without an applied magnetic field the nanoparticle (which we model to be a single domain) has its magnetization along the plane of the long-axis which because of shape anisotropy is the preferred orientation. Applying an out-of-plane magnetic field rotates the internal magnetization by $\pi/2$ so that it points along the field direction (see cartoons in Fig. 1.8). The small field data probes both the effects of the magnetic field itself, and the effect of rotating the internal magnetization, whereas for larger magnetic fields, one only probes the effect of the applied field.

From the data in Fig. 1.8, we see "mesoscopic anisotropic magnetoconductance fluctuations", which is the ferromagnetic analog of these well known universal con-

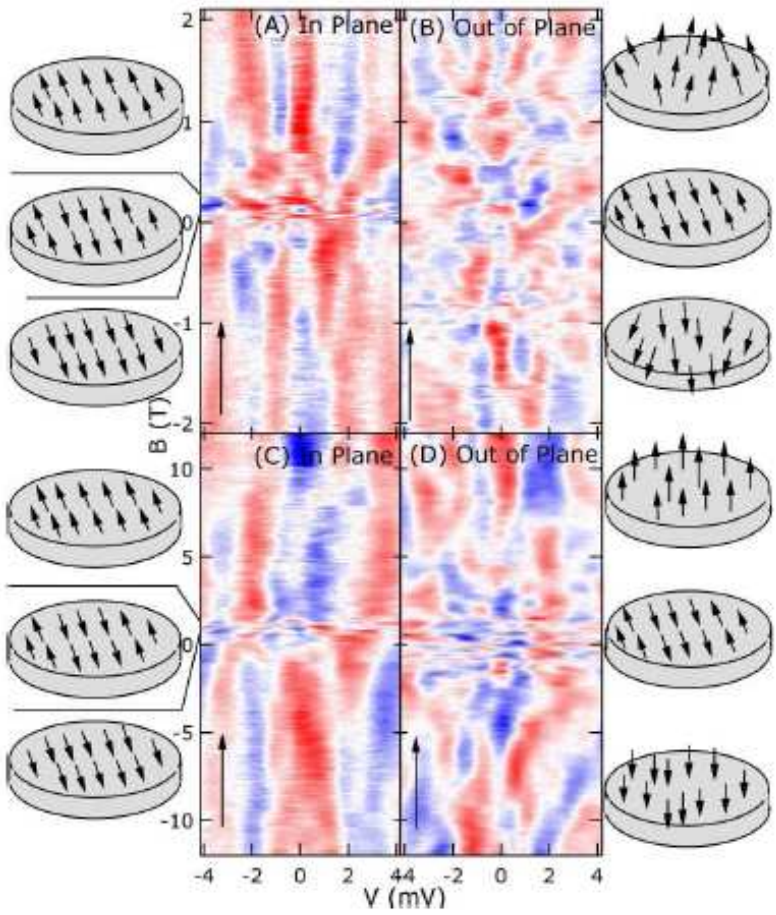

Figure 1.8: A and B: Fluctuations in differential resistance with bias voltage and the in-plane and the out-of plane magnetic field, respectively. C and D: same as A and B, but in a wider field range. The expected magnetic configurations are indicated by the schematics. Figure from Ref. [41] and available online at http://arxiv.org/format/cond-mat/0509452.

ductance fluctuations in normal metals. It is well established that the conductance of a ferromagnetic particle depends on the relative orientation of the magnetization with respect to the direction of current flow. This is the standard anisotropic magnetoresistance (AMR) effect (See Ref. [42]). What we describe is this thesis is a theoretical framework to understand the mesoscopic effect that consists of an additional and faster random dependence on the magnetization direction that is different for each sample, but reproducible for a given sample. Its origin is the coherent multiple scattering off impurities in the ferromagnet. As a function of magnetization direction, the mesoscopic correction will show a quick succession of minima and maxima, superimposed on the smooth material-dependent anisotropic magnetoresistance of the bulk material. We identify two possible sources for this non-monotonic behaviour. The first is that changing the direction of the internal magnetization (or the change of the applied magnetic field itself for large field) directly affects the orbital motion of electrons by changing the amount of Aharonov-Bohm phase picked up by the electron orbit. The correlation angle (which sets the field scale on which we should see conductance correlations) for this orbital effect is set by Φ_0/Φ where Φ_0 is the flux quantum, and Φ is the magnetic flux through a phase coherent area. One finds that this effect orbital scales as L^{-2}, where L is the system size. Another mechanism for mesoscopic fluctuations is caused by spin-orbit scattering. Without spin-orbit scattering, changing the external field will merely rotate the magnetization direction which would only change the spin-quantization axis, but not affect the conductances. However, the presence of spin-orbit scattering couples the orbital motion to the spin-quantization axis and this leads to accumulation of different phases for different directions of the internal magnetization. One can estimate that the square of the correlation angle for

this effect scales as the ratio of the spin-orbit energy scale to the Thouless Energy, concluding that the correlation angle scales as L^{-1}. Comparing the two estimates, we see that for smaller phase-coherent lengths, the spin-orbit effect dominates, consistent with the observations in Ref. [41]. In Chapter 5 we calculate the mesoscopic anisotropic magnetoconductance fluctuations using the methods of Ref. [40] generalized for a ferromagnet. We find that for coherence lengths $L_\phi \lesssim 100$ nm the spin-orbit effect dominates which should be the case for the samples in Ref. [41] where they estimate that $L_\phi \sim 30$ nm. In this case, one finds that when rotating the magnetization by an angle $\pi/2$, the orbital effect gives about 1 conductance oscillation, while the spin-orbit effect gives about 5 oscillations, which consistent with the data shown in Fig. 1.8.

BIBLIOGRAPHY

[1] J. C. Slonczewski, J. Magn. Magn. Mater. **159**, 1 (1996).

[2] L. Berger, Phys. Rev. B **54**, 9353 (1996).

[3] *Applications of Random Matrices in Physics*, edited by E. Brézin, V. Kazakov, D. Serban, P. Wiegmann and A. Zabrodin (Springer, Dordrecht, 2006).

[4] L. P. Gorkov and G. M. Eliashberg, Sov. Phys. JETP **21**, 940 (1965).

[5] B. L. Altshuler and B. Simons, in *Mesoscopic Quantum Physics*, edited by E. Akkermans et al. (Elsevier, Amsterdam, 1995).

[6] D. J. Thouless, J. Phys. C **8**, 1803 (1975).

[7] D. J. Thouless, Phys. Rev. Lett. **39**, 1167 (1977).

[8] K. B. Efetov, *Supersymmetry in disorder and chaos* (Cambridge University Press, New York, 1997).

[9] A. Pandey and M. L. Mehta, Commun. Math. Phys. **87**, 449 (1983).

[10] A. Tschersich and K. B. Efetov, Phys. Rev. E **62**, 2042 (2000).

[11] S. Adam, P. W. Brouwer, and P. Sharma, Phys. Rev. B **68**, 241311 (2003).

[12] S. A. van Langen, P. W. Brouwer, and C. W. J. Beenakker, Phys. Rev. E **55**, 1 (1997).

[13] V. I. Fal'ko and K. B. Efetov, Phys. Rev. Lett. **77**, 912 (1996).

[14] N. Taniguchi, A. Hashimoto, B. D. Simons, and B. L. Altshuler, Europhys. Lett. **27**, 335 (1994).

[15] S. Braig, S. Adam, and P. W. Brouwer, Phys. Rev. B **68**, 035323 (2003).

[16] P. W. Brouwer, X. Waintal, and B. I. Halperin, Phys. Rev. Lett. **85**, 369 (2000).

[17] I. L. Aleiner, P. W. Brouwer, and L. I. Glazman, Phys. Rep. **358**, 309 (2002).

[18] D. C. Ralph, C. T. Black, and M. Tinkham, Phys. Rev. Lett. **74**, 3241 (1995).

[19] J. von Delft and D. C. Ralph, Phys. Rep. **345**, 61 (2001).

[20] J. R. Petta and D. C. Ralph, Phys. Rev. Lett. **89**, 156802 (2002).

[21] D. G. Salinas, S. Guéron, D. C. Ralph, C. T. Black, and M. Tinkham, Phys. Rev. B **60**, 6137 (1999).

[22] D. Davidovic and M. Tinkham, Phys. Rev. Lett. **83**, 1644 (1999).

[23] D. Davidovic and M. Tinkham, Phys. Rev. B **61**, 16359 (2000).

[24] J. R. Petta and D. C. Ralph, Phys. Rev. Lett. **87**, 266801 (2001).

[25] K. A. Matveev, L. I. Glazman, and A. I. Larkin, Phys. Rev. Lett. **85**, 2789 (2000).

[26] X. Waintal, E. B. Myers, P. W. Brouwer, and D. C. Ralph, Phys. Rev. B **62**, 12317 (2000).

[27] E. Myers, D. Ralph, J. Katine, R. Louie, and R. Buhrman, Science **285**, 867 (1999).

[28] F. J. Albert, J. A. Katine, R. A. Buhrman, and D. C. Ralph, **77**, 3809 (2000).

[29] M. L. Polianski and P. W. Brouwer, Phys. Rev. Lett. **92**, 026602 (2004).

[30] M. D. Stiles, J. Xiao, and A. Zangwill, Phys. Rev. B. **69**, 054408 (2004).

[31] B. Özyilmaz, A. D. Kent, J. Z. Sun, M. J. Rooks, R. H. Koch, Phys. Rev Lett. **93**, 176604 (2004).

[32] A. Brataas, Y. Tserkovnyak, and G. Bauer, cond-mat/0501672 (2005).

[33] A. Brataas and X. H. Wang, cond-mat/0004082 (2000).

[34] Y. Tserkovnyak, A. Brataas, and G. E. W. Bauer, Phys. Rev. Lett. **88**, 117601 (2002).

[35] A. A. Abrikosov, L. P. Gorkov, and I. E. Dzyaloshinski, *Methods of quantum field theory in statistical physics* (Dover, New York, 1975).

[36] S. Doniach and E. H. Sondheimer, *Green's Functions for Solid State Physicists* (Imperial College Press, London, 1998).

[37] H. Bruus and K. Flensberg, *Many-Body Quantum Theory in Condensed Matter Physics: An Introduction* (Oxford University Press, Oxford, 2004).

[38] B. L. Altshuler, JETP Lett. **41**, 648 (1985).

[39] P. A. Lee and A. D. Stone, Phys. Rev. Lett. **55**, 1622 (1985).

[40] P. A. Lee, A. D. Stone, and H. Fukuyama, Phys. Rev. B **35**, 1039 (1987).

[41] Y. G. Wei, X. Y. Liu, L. Y. Zhang, and D. Davidović, cond-mat/0509452 (2005).

[42] R. C. O'Handley, *Modern Magnetic Materials* (Wiley, New York, 2000).

Chapter 2

Enhanced mesoscopic fluctuations in the crossover between random matrix ensembles

2.1 Introduction

Random matrix theory has focused on the study of three ensembles of Hamiltonians: the Gaussian Unitary Ensemble (GUE), the Gaussian Orthogonal Ensemble (GOE), and the Gaussian Symplectic Ensemble (GSE). These describe the statistics of single-particle energy levels and wavefunctions of disordered metal grains or chaotic quantum dots with the corresponding symmetries; GUE if time-reversal symmetry is broken, and GOE or GSE if time-reversal symmetry is present and spin-rotation symmetry is present or absent, respectively. In these three basic ensembles, eigenvector elements are Gaussian complex/real/quaternion random numbers; elements of the same eigenvector and of different eigenvectors are all

statistically independent [1].

Disordered or chaotic systems with partially broken symmetries show a variety of phenomena that go beyond a mere "interpolation" of descriptions based on the GOE, GUE, and GSE alone. For example, in a quantum dot, a weak magnetic field causes long-range wavefunction correlations [2, 3, 4, 5] and a non-Gaussian distribution of "level velocities", derivatives of energy levels with respect to, e.g., a shape change of the dot [6]. Both effects are absent without a magnetic field (in the GOE), or when the magnetic field is strong enough to fully break time-reversal symmetry (in the GUE). In a metal grain, weak spin-orbit interaction induces mesoscopic fluctuations of the g-tensor [7, 8], which does not fluctuate in either the GOE or the GSE. Further, as we'll show below, in a weak magnetic field or for weak spin-orbit scattering, matrix elements of the electron-electron interaction exhibit fluctuations that are parametrically larger than in each of the three basic ensembles.

The underlying reason for these phenomena is that eigenvector elements are not independent in (random-matrix) ensembles that interpolate between the three basic symmetry classes: There exist both correlations within the same eigenvector [2, 3, 4, 5, 6, 7] and, as we show in this chapter, between different eigenvectors. To study the eigenvector correlations in such crossover ensembles, we will make use of a surprising relation between the eigenvector statistics late in the crossover from class A to class B and that of finite-sized matrices in class B (where B is the class of lower symmetry). Examples of such a relation were known for the statistics of a single eigenvector. For example, in the GOE-GUE crossover, which is described by the $N \times N$ random hermitian matrix (with N taken to ∞ at the end of the

calculation)[9]

$$H_{\mathrm{OU}}(N,\alpha) = H_{\mathrm{O}}(N) + \frac{\alpha}{\sqrt{N}} H_{\mathrm{U}}(N), \tag{2.1}$$

the distribution of the "phase rigidity" $|\boldsymbol{v}^{\mathrm{T}}\boldsymbol{v}|^2$ [6] of a single eigenvector $\boldsymbol{v}$ is the same as in the *finite-sized* $M \times M$ GUE ensemble with $M = 2\alpha^2$ if α is large. In Eq. (2.1), $H_{\mathrm{O}}(N)$ and $H_{\mathrm{U}}(N)$ are $N \times N$ matrices taken from the GOE and GUE, respectively, with equal variances for the matrix elements. A similar correspondence occurs for the g-tensor of a Kramers doublet in the GOE-GSE crossover [7, 8]. Our main finding is that such a correspondence extends to the correlations between different eigenvectors.

In this chapter we will accomplish four tasks. (i) We show numerically that the relation

$$H_{\mathrm{OU}}(N,\alpha) \leftrightarrow H_{\mathrm{U}}(M), \quad M = 2\alpha^2 \tag{2.2}$$

between the GOE-GUE crossover Hamiltonian $H_{\mathrm{OU}}(\alpha)$ for large α and N and a finite-sized $M \times M$ GUE Hamiltonian extends to correlations between eigenvectors. Just as in critical phenomena, where simple power laws unfold into universal scaling functions as you flow away from the critical point, here a rich theory of correlations unfolds in the crossover region. We wish to point out that this principle applies not only to the GOE-GUE crossover, but also, e.g., to the GOE-GSE crossover, or to wavefunctions in two coupled quantum dots, which are described by a random Hamiltonian interpolating between two independent GUE's and one GUE of double size [10]. (ii) We show that, for large α, the universality classes are actually curves in the $(1/\alpha, 1/N)$ plane, reminiscent of renormalization-group flow trajectories (Renormalization group ideas have been applied previously to study universality and deviations from universality in the three basic ensembles of random matrix theory see Ref. [11, 12, 13]). (iii) We calculate correlations between

eigenvectors, based on the surmise (2.2) and diagrammatic perturbation theory. (iv) We calculate how the inter-eigenvector correlations in the crossover region affect matrix elements of the electron-electron interaction in a quantum dot or metal grain in a weak magnetic field, and predict a significant enhancement of fluctuations compared to the basic ensembles.

2.2 Orthogonal invariants

Let us now consider the joint distribution $P(\{\boldsymbol{v}_\mu\})$ of n eigenvectors $\boldsymbol{v}_\mu$, $\mu = 1, \ldots, n$, for the example of the GOE-GUE crossover Hamiltonian (2.1). Throughout the entire GOE-GUE crossover, the distribution of the eigenvectors is invariant under orthogonal transformations. As a consequence, the joint distribution $P(\{\boldsymbol{v}_\mu\})$ is completely determined by the distribution of the orthogonal invariants [2, 3]

$$\rho_{\mu\nu} = \rho_{\nu\mu} = \boldsymbol{v}_\mu^{\mathrm{T}} \boldsymbol{v}_\nu, \quad \mu, \nu = 1, \ldots, n, \tag{2.3}$$

where the superscript T denotes transposition. Hence

$$\begin{aligned} P(\{\boldsymbol{v}_\mu\}) &= \int \prod_{\mu \le \nu}^{n} d\rho_{\mu\nu}\, P(\{\rho_{\mu\nu}\}) \\ &\quad \times \prod_{\mu \le \nu}^{n} \delta(\boldsymbol{v}_\mu^\dagger \boldsymbol{v}_\nu - \delta_{\mu\nu}) \delta(\boldsymbol{v}_\mu^{\mathrm{T}} \boldsymbol{v}_\nu - \rho_{\mu\nu}). \end{aligned} \tag{2.4}$$

For the physically relevant case of large N, Eq. (2.4) implies that the eigenvector elements $\boldsymbol{v}_{\mu m}$, $m = 1, \ldots, N$, have a Gaussian distribution with zero mean and

$$\langle v_{\mu m}^* v_{\nu n} \rangle_\rho = \frac{1}{N} \delta_{\mu\nu} \delta_{mn}, \quad \langle v_{\mu m} v_{\nu n} \rangle_\rho = \frac{1}{N} \rho_{\mu\nu} \delta_{mn}. \tag{2.5}$$

The subscript $\langle \ldots \rangle_\rho$ indicates that the average is taken at fixed $\rho_{\mu\nu}$. For the full ensemble average one has to perform a subsequent average over the $\rho_{\mu\nu}$ with the

distribution $P(\{\rho_{\mu\nu}\})$. We can find $P(\{\rho_{\mu\nu}\})$ from the surmise that, for $\alpha \gg 1$ and for eigenvectors $\boldsymbol{v}_\mu$ whose energies are all inside a window of size $\ll \alpha^2\Delta$, Δ being the level spacing of the Hamiltonian $H(\alpha)$, the joint distribution of the $\rho_{\mu\nu}$ *is the same as for a GUE Hamiltonian of finite size* $M = 2\alpha^2$. Thus the $\rho_{\mu\nu}$ are independently and Gaussian distributed with zero mean and with variance

$$\langle|\rho_{\mu\nu}|^2\rangle = (1+\delta_{\mu\nu})/M, \quad M = 2\alpha^2. \tag{2.6}$$

Together, Eqs. (2.4)–(2.6) fix the joint distribution of eigenvectors in the crossover ensemble close to the GUE. For the single-eigenvector distribution, they reproduce the $\alpha \gg 1$ limit of the exact solution of Ref. [3]. The fact that the phase rigidity $|\rho_{\mu\mu}|^2$ of a single eigenvector is a fluctuating quantity is the prime cause of the correlations between elements of one eigenvector [4, 5, 6]; It is the existence of nonzero and fluctuating $\rho_{\mu\nu}$ for $\mu \neq \nu$ that causes the correlations between different eigenvectors.

2.3 Verification of surmise

2.3.1 Heuristic picture

We now proceed to present arguments in support of our surmise. We consider eigenvectors $\boldsymbol{v}_\mu$ ($\mu = 1, \ldots, n$) with energies within a distance $\ll \alpha^2\Delta$ from a reference energy $\varepsilon_{\rm ref}$, sorting them by increasing energy. We then consider how each of these eigenvectors is built up from the eigenvectors $\boldsymbol{o}_\nu$ of the unperturbed Hamiltonian $H_{\rm O}$. The admixture of eigenvectors $\boldsymbol{o}_\nu$ with energy ε_ν far away from $\varepsilon_{\rm ref}$ is small and can be neglected if $|\varepsilon_{\rm ref} - \varepsilon_\nu|$ is large enough. On the other hand, eigenvectors $\boldsymbol{o}_\nu$ with energy ε_ν close to $\varepsilon_{\rm ref}$ contribute non-perturbatively for large

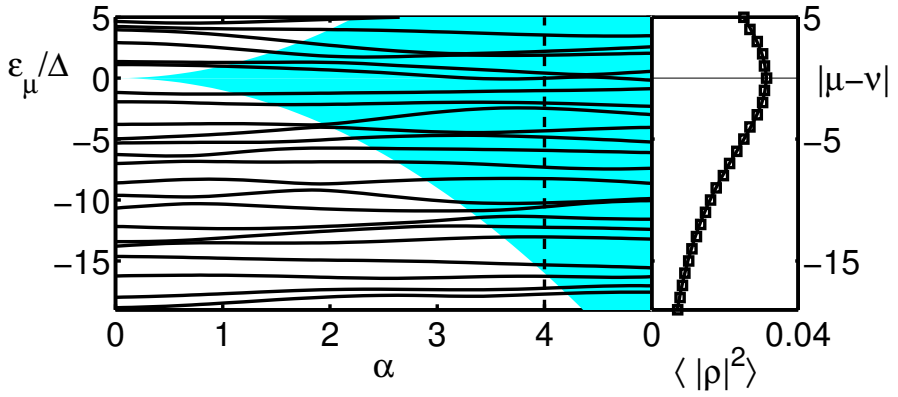

Figure 2.1: Left panel: Eigenvalues for one realization of $H_{\rm OU}(\alpha)$. The shaded region marks the energy window of size $\sim M(\alpha)\Delta = 2\alpha^2\Delta$ for which the eigenvalues are kept in the effective $M \times M$ GUE Hamiltonian. Right panel: $\langle|\rho_{\mu\nu}|^2\rangle$ as a function of the distance $\mu - \nu \approx (\varepsilon_\mu - \varepsilon_\nu)/\Delta$ between eigenvalues, for $\alpha = 4.0$ (dashed line, left panel). Solid curve: Eq. (2.9). Data points: numerical calculation for $N = 400$.

α. Upon increasing α, the eigenvectors $\boldsymbol{v}_\mu(\alpha)$ in the latter energy range have undergone several avoided crossings, and the unperturbed eigenvectors $\boldsymbol{o}_\nu$ have roughly equal weights in each of the vectors $\boldsymbol{v}_\mu(\alpha)$ in our set.

It is on this heuristic picture that our surmise for an effective description of the eigenvector statistics for large α is based: We only retain those eigenvectors of the unperturbed Hamiltonian $H_{\rm O}$ that are relatively close in energy and hence all contribute roughly equally, see Fig. 2.1 for a cartoon. Since the time-reversal symmetry breaking perturbation in Eq. (2.1) is strong for these eigenvectors, the matrix elements between them form a random hermitian matrix of the GUE. Denoting the effective number of contributing unperturbed eigenvectors as $M(\alpha)$, we thus reduce the problem of finding the distribution of the orthogonal invariants

$\rho_{\mu\nu}$ for the $N \times N$ crossover Hamiltonian (2.1) to that of finding the distribution of the $\rho_{\mu\nu}$ for the much smaller GUE Hamiltonian of size $M(\alpha)$. To calculate $M(\alpha)$ in terms of N and α, we turn to the exact solution for the single-eigenvector distribution obtained in Refs. [3, 4, 5, 6], and find

$$M(\alpha) = \alpha^2 N(\alpha^2 + 2N)/(\alpha^2 + N)^2. \tag{2.7}$$

For large N this simplifies to $M(\alpha) = 2\alpha^2$, in agreement with Eq. (2.6). A rough estimate of M can be obtained by comparing the contributions to $\boldsymbol{v}_\mu(\alpha)$ from unperturbed eigenvectors $\boldsymbol{o}_\nu$ with energy ε_ν close to (far away) from ε_μ, which are (are not) included in the effective $M \times M$ GUE Hamiltonian. In the former case, the weight of $\boldsymbol{o}_\nu$ is $\sim M^{-1}$, whereas in the latter case it is $\sim \alpha^2 h^2/N|\varepsilon_\mu - \varepsilon_\nu|^2$, where $h^2 = N\Delta^2/\pi^2$ is the mean square of an element of $H_{\rm U}$. Comparing the two estimates at the energy difference $|\varepsilon_\mu - \varepsilon_\nu| \sim M\Delta/2$ separating the two regimes, we conclude $M \sim \alpha^2$, in agreement with the exact result (2.7).

2.3.2 Numerical verification

By our surmise, the distribution of the orthogonal invariants should depend on the effective matrix size $M(\alpha)$ only, not on α and N individually, as long as N and α are large. We have verified this by numerical calculation of the averages $\langle|\rho_{\mu\nu}|^2\rangle$ for different points along a curve of constant $M(\alpha)$ in the $(1/N, 1/\alpha)$ plane. The results of such a calculation are shown in Fig. 2.2 for $\mu = \nu$, $\mu = \nu + 1$, and $\mu = \nu + 2$. We have also verified that the distribution of the $\rho_{\mu\nu}$ is indeed Gaussian (not shown).

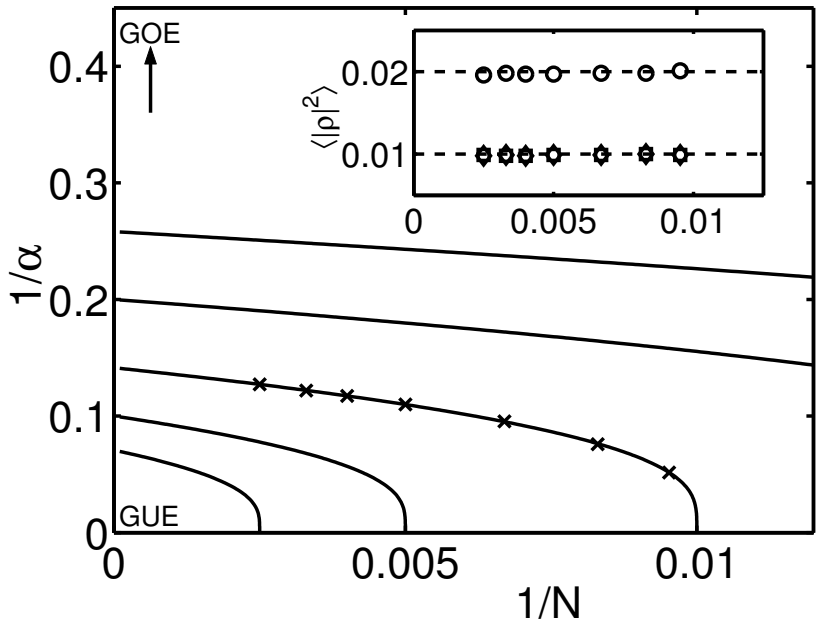

Figure 2.2: Curves of constant effective GUE size $M(\alpha)$, Eq. (2.7), in the $(1/\alpha, 1/N)$ plane for the $N \times N$ crossover Hamiltonian (2.1). Top to bottom: $M = 30$, $M = 50$, $M = 100$, $M = 200$, and $M = 400$. The horizontal and vertical axes correspond to the pure GUE and to the $N \to \infty$ crossover Hamiltonian, respectively. Inset: $\langle |\rho_{\mu\nu}|^2 \rangle$ for the points indicated at the $M = 100$ curve in the main panel. Circles: $\mu = \nu$; Squares: $\mu = \nu + 1$ (eigenvectors with neighboring energy levels); diamonds: $\mu = \nu + 2$ (next-nearest neighbors). The dashed lines indicate the surmise of Eq. (2.6).

2.3.3 Diagrammatic perturbation theory

The surmise (2.2) is expected to be valid as long as only eigenvectors taken from an energy window of width $\ll M(\alpha)\Delta = 2\alpha^2\Delta$ are involved. If the energy differences between eigenvectors become of order $\alpha^2\Delta$ or larger, the eigenvectors $\boldsymbol{v}_\mu(\alpha)$ do not share the same unperturbed eigenvectors $\boldsymbol{o}_\nu$, and we thus expect that they become uncorrelated. A quantitative description of eigenvector correlations at energy separations $\gg \Delta$ can be obtained using diagrammatic perturbation theory. The only nonzero second moment is $\langle|\rho_{\mu\nu}|^2\rangle$, which can be computed from

$$\begin{aligned}\langle|\rho_{\mu\nu}|^2\rangle &= -\frac{\Delta^2}{4\pi^2}\sum_{s_1,s_2=\pm} s_1 s_2 \\ &\quad\times\left\langle \operatorname{tr} G^{\mathrm{T}}(\varepsilon_\mu + is_1\delta)G(\varepsilon_\nu + is_2\delta)\right\rangle . \end{aligned} \tag{2.8}$$

where $G(z) = 1/(z - H_{\mathrm{OU}})$, δ is a positive infinitesimal, and the eigenvectors $\boldsymbol{v}_\mu$ and $\boldsymbol{v}_\nu$ have energies ε_μ and ε_ν, respectively. Calculating the averages using the technique of Ref. [14], we find, if $\mu \neq \nu$,

$$\langle|\rho_{\mu\nu}|^2\rangle = \frac{2\alpha^2}{4\alpha^4 + \pi^2(\varepsilon_\mu - \varepsilon_\nu)^2/\Delta^2}. \tag{2.9}$$

A similar result for parametric correlations inside a basic random-matrix ensemble was derived in Ref. [15]. The right panel of Fig. 2.1 shows $\langle|\rho_{\mu\nu}|^2\rangle$ as a function of $\varepsilon_\mu - \varepsilon_\nu$ and a numerical calculation of the same quantity.

2.4 Discussion and conclusion

The GOE-GUE crossover describes wavefunction statistics in, e.g., a chaotic quantum dot or a disordered metal grain in a weak magnetic field. Wavefunction distributions have immediate experimental relevance for the spacings, widths, and heights of Coulomb blockade peaks in the conductance of metal grains or quantum

dots [16]. Correlations between wavefunctions of neighboring energy levels cause correlations between the heights and widths of conductance peaks. Wavefunction distributions also influence the positions of Coulomb blockade peaks through the electron-electron interaction matrix elements [17], which we now discuss in detail. The interaction matrix element $U_{\mu\nu\rho\sigma}$ is defined as

$$\begin{aligned} U_{\mu\nu\rho\sigma} &= \int d\mathbf{r}_1 d\mathbf{r}_2 U(\mathbf{r}_1 - \mathbf{r}_2) \\ &\quad \times \phi_\mu(\mathbf{r}_1)\phi_\nu(\mathbf{r}_2)\phi_\rho(\mathbf{r}_2)^*\phi_\sigma(\mathbf{r}_1)^*, \end{aligned} \tag{2.10}$$

where $U(\mathbf{r})$ is the electron-electron interaction potential and $\phi_\mu(\mathbf{r})$ the wavefunction for an electron in level ε_μ. For example, the difference of interaction matrix elements $U_{\mu\nu\nu\mu} - U_{\mu oo\mu}$ gives the spacing between peak positions corresponding to different nonequilibrium configurations (levels ν and o unoccupied, respectively) in tunneling spectroscopy of small metal grains [18].

In a metal grain or quantum dot, the interaction can be approximated by an $\mathbf{r}$-independent part and a local interaction $U^{\rm loc}(\mathbf{r}) = \lambda\Delta V\delta(\mathbf{r})$, where Δ is the mean level spacing, V the sample volume, and λ a parameter of order unity governing the strength of the local interaction. The spatially constant interaction leads to a charging energy and does not show mesoscopic fluctuations. Without magnetic field, the ensemble average of matrix elements of $U^{\rm loc}$ is [16]

$$\langle U^{\rm loc}_{\mu\nu\rho\sigma}\rangle = \lambda\Delta(\delta_{\mu\sigma}\delta_{\nu\rho} + \delta_{\mu\rho}\delta_{\nu\sigma} + \delta_{\mu\nu}\delta_{\rho\sigma}). \tag{2.11}$$

If time-reversal symmetry is broken by a magnetic field (i.e., in the GUE), the last term in Eq. (2.11) is left out. For repulsive interactions, the last term in Eq. (2.11) also vanishes in the GOE once the renormalization of the Cooper channel of the local interaction is taken into account, see, e.g., Ref. [16]. The Cooper channel renormalization also affects the enhanced fluctuations in the GOE-GUE

crossover. The enhancement of the fluctuations of interaction matrix elements in other crossovers, such as the crossover GOE-GSE or the crossover of Ref. [10], is not renormalized.

In both the GOE and GUE, fluctuations of the interaction matrix elements $U^{\rm loc}_{\mu\nu\rho\sigma}$ and corrections to Eq. (2.11) are nonuniversal and small as (at most) $g^{-1/2}$, g being the sample's dimensionless conductance. Equation (2.11) can be reproduced from random-matrix theory if the wavefunctions $\phi_\mu(\mathbf{r})$ are replaced by eigenvectors $\boldsymbol{v}_\mu$ and the integration over space is replaced by a summation over the vector indices.

How are the interaction matrix elements distributed in the presence of a weak magnetic field? If we are not interested in the non-universal $(1/g)$ corrections, that question can be answered using the eigenvector distributions for the GOE-GUE crossover that we derived above. First, upon increasing the magnetic field, there is a suppression of the last term in Eq. (2.11).

Second, the appearance of inter-eigenvector correlations enhances the average of "diagonal" interaction matrix elements $U_{\mu\nu\rho\sigma}$ with μ,ν and ρ,σ pairwise equal: Using Eq. (2.5), we find

$$\langle U^{\rm loc}_{\mu\nu\rho\sigma}\rangle \;=\; \lambda\Delta(\delta_{\mu\rho}\delta_{\nu\sigma}+\delta_{\mu\sigma}\delta_{\nu\rho}+\langle\rho_{\mu\nu}\rho^*_{\rho\sigma}\rangle). \tag{2.12}$$

For $\alpha\gg 1$, $\langle\rho_{\mu\nu}\rho^*_{\rho\sigma}\rangle$ is given by Eqs. (2.6) and (2.9), hence

$$\begin{aligned}\langle U^{\rm loc}_{\mu\nu\rho\sigma}\rangle \;&=\; \lambda\Delta(\delta_{\mu\rho}\delta_{\nu\sigma}+\delta_{\mu\sigma}\delta_{\nu\rho})\\ &\quad\times\left(1+\frac{2\alpha^2}{4\alpha^4+\pi^2(\varepsilon_\mu-\varepsilon_\nu)^2/\Delta^2}\right).\end{aligned} \tag{2.13}$$

Third, the inter-eigenvector correlations enhance the fluctuations of the interaction matrix elements. This is best illustrated by the expectation value $\langle|U_{\mu\nu\rho\sigma}|^2\rangle$ with

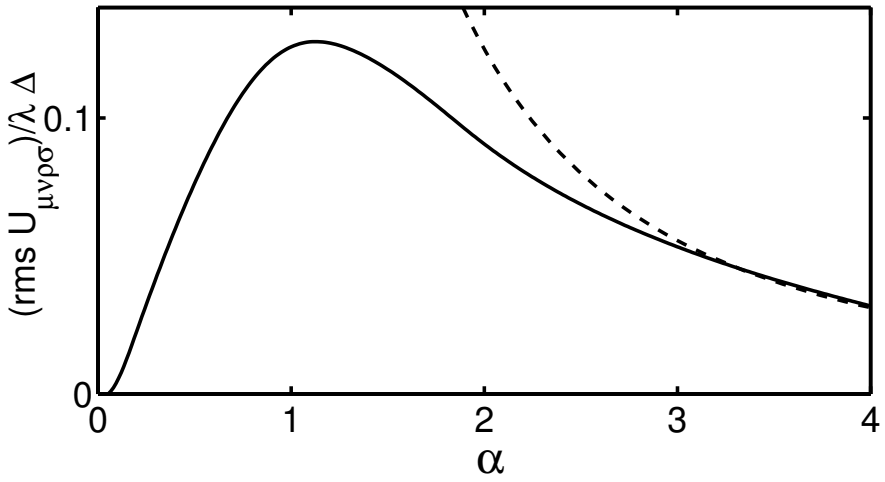

Figure 2.3: Root-mean-square fluctuations of the interaction matrix element $U_{\mu\nu\rho\sigma}$ for four consecutive levels $\mu = \nu - 1 = \rho - 2 = \sigma - 3$. The dashed line shows the large-α asymptote of Eq. (2.14). The solid line is obtained from numerical generation of 400×400 GOE-GUE crossover matrices, using $\langle |U_{\mu\nu\rho\sigma}|^2 \rangle = (\lambda\Delta)^2 \langle |\rho_{\mu\nu}|^2 |\rho_{\rho\sigma}|^2 \rangle$. (Direct numerical calculation of $U_{\mu\nu\rho\sigma}$ suffers from large finite-N corrections.)

all four indices μ, ν, ρ, and σ different,

$$\langle |U^{\rm loc}_{\mu\nu\rho\sigma}|^2 \rangle \;\; = \;\; (\lambda\Delta)^2 \langle |\rho_{\mu\nu}|^2 |\rho_{\rho\sigma}|^2 \rangle = (\lambda\Delta)^2/(2\alpha^2)^2. \qquad (2.14)$$

The first equality in Eq. (2.14) holds for all α, the second one only if $\alpha \gg 1$ and the four eigenvalues ε_μ, ε_ν, ε_ρ, ε_σ are within a distance $\ll \alpha^2\Delta$ of each other. We have numerically calculated $\langle |U^{\rm loc}_{\mu\nu\rho\sigma}|^2 \rangle$ for four neighboring energy levels, see Fig. 2.3.

A similar increase of the fluctuations of the interaction matrix elements is found for other crossovers between random matrix ensembles, such as the crossover between GOE and GSE.

Although the fluctuations are small if $\alpha \gg 1$, they can be significantly larger

than the non-universal fluctuations that vanish as g^{-2} [for Eq. (2.14)]. The existence of nonzero off-diagonal interaction matrix elements and large fluctuations of the diagonal matrix elements implies that existing analytical methods based on the universal description of electron-electron interactions in terms of the total spin and the total charge only [16] are not valid in the crossover regime. For a full description, new calculations, using the tools developed in this chapter, are necessary.

The origin of the eigenvector correlations and the enhanced fluctuations of interaction matrix elements can be sought in the existence of the large parameter α^2 that plays a role similar to the dimensionless conductance g in the pure ensembles. The parameter α^2 can be identified as the ratio of the Heisenberg time $\tau_{\rm H} = 2\pi\hbar/\Delta$ and the time $\tau_{\rm OU}$ needed to acquire a flux quantum [16]. Late in the crossover, GUE physics ranges from the mean level spacing Δ up to the scale $\hbar/\tau_{\rm OU}$. In the pure GUE, however, validity of random-matrix theory ceases only at the higher energy scale $\hbar/\tau_{\rm erg}$, where $\tau_{\rm erg}$ is the ergodic time. The role of the large parameter $g = \tau_{\rm H}/\tau_{\rm erg}$, which governs wavefunction correlations and interaction matrix element fluctuations in the "pure" GUE and GOE is thus played by $\alpha^2 \sim \tau_{\rm H}/\tau_{\rm OH}$ in the GOE-GUE crossover.

BIBLIOGRAPHY

[1] M. L. Mehta, *Random Matrices*, 2 ed. (Academic Press, New York, 1991).

[2] J. B. French, V. K. B. Kota, A. Pandey, and S. Tomsovic, Ann. Phys. (N. Y.) **181**, 198 (1988).

[3] H.-J. Sommers and S. Iida, Phys. Rev. E **49**, 2513 (1994).

[4] V. I. Fal'ko and K. B. Efetov, Phys. Rev. B **50**, 11267 (1994).

[5] V. I. Fal'ko and K. B. Efetov, Phys. Rev. Lett. **77**, 912 (1996).

[6] S. A. van Langen, P. W. Brouwer, and C. W. J. Beenakker, Phys. Rev. E **55**, 1 (1997).

[7] P. W. Brouwer, X. Waintal, and B. I. Halperin, Phys. Rev. Lett. **85**, 369 (2000).

[8] K. A. Matveev, L. I. Glazman, and A. I. Larkin, Phys. Rev. Lett. **85**, 2789 (2000).

[9] A. Pandey and M. L. Mehta, Commun. Math. Phys. **87**, 449 (1983).

[10] A. Tschersich and K. B. Efetov, Phys. Rev. E **62**, 2042 (2000).

[11] E. Brézin and J. Zinn-Justin, Phys. Lett. B **288**, 54 (1992).

[12] E. Brézin and A. Zee, Compt. Rend. Acad. Sci **17**, 735 (1993).

[13] S. Higuchi, C. Itoi, S. Hishigaki, and N. Sakai, Nucl. Phys. B **434**, 283 (1995).

[14] E. Brézin and A. Zee, Phys. Rev. E **49**, 2588 (1994).

[15] M. Wilkinson and P. N. Walker, J. Phys. A: Math. Gen. **28**, 6143 (1995).

[16] I. L. Aleiner, P. W. Brouwer, and L. I. Glazman, Phys. Rep. **358**, 309 (2002).

[17] J. von Delft and D. C. Ralph, Phys. Rep. **345**, 61 (2001).

[18] O. Agam, N. S. Wingreen, B. L. Altshuler, D. C. Ralph, and M. Tinkham, Phys. Rev. Lett. **78**, 1956 (1997).

Chapter 3

Magnetic-field dependence of energy levels in ultrasmall metal grains

3.1 Introduction

Recent developments in nanofabrication techniques have allowed for the resolution of individual "particle-in-a-box" energy levels in small metal grains or semiconductor quantum dots using tunneling spectroscopy [1, 2, 3, 4]. In the absence of a magnetic field, the energy levels ε_μ are two-fold degenerate (Kramers' degeneracy). An applied magnetic field B lifts the degeneracy; the splitting of the doublet is described with the help of a "g factor",

$$\delta\varepsilon_\mu = \mu_B g B, \tag{3.1}$$

where $\mu_B = e\hbar/2mc$ is the Bohr magneton. A cartoon of the magnetic-field dependence of the energy levels is shown in Fig. 3.1. Whereas $g = 2$ for electrons

in vacuum, in a metal grain the g factor can be different from two as a result of spin-orbit scattering. Recently, the magnetic-field dependence of particle-in-a-box levels in metal grains have been measured by two groups [5, 6, 7, 8, 9]. Measured g factors range from 0.1 to 2, depending on grain size, material, and, in the case of Ref. [5], doping with heavy ions.

Unlike in bulk metals, where g factors are used to describe the effect of spin-orbit coupling on the band structure, g factors in a metal grain are not a "bulk" property [10]. Not only does the typical value of the g factors depend on the size of the metal grain, g factors also depend on the microscopic details such as the impurity configuration, the location of defects, and the form of the grain boundary. As a result, different energy levels in a metal grain have different g factors. Moreover, even if the metal grain is roughly spherical and without lattice anisotropy, the presence of impurities breaks the rotational symmetry on the microscopic scale, causing g factors to depend on the direction of the applied magnetic field. A statistical description of the level-to-level fluctuations of g factors in metal grains has been formulated by Matveev *et al.*[11] and by Brouwer, Waintal and Halperin [12] using random matrix theory (RMT). Petta and Ralph [8] measured g factors for up to 9 consecutive levels in nanometer-size Cu, Ag, and Au grains and found good agreement with the distributions of Refs. [11, 12]. The dependence on the direction $\hat{B}$ of the magnetic field is taken into account by replacing the g factor by a "g tensor" $\mathcal{G}$ [13],

$$\delta\varepsilon_\mu = \mu_B B(\hat{B}^{\mathrm{T}}\mathcal{G}_\mu\hat{B})^{1/2}. \tag{3.2}$$

(The g tensor carries a subscript μ to reflect its dependence on the energy level ε_μ, and $\hat{B}^{\mathrm{T}}$ is the vector transpose of $\hat{B}$.) The g-factor (3.1) for a magnetic field in the z direction is the square root of the tensor element $\mathcal{G}_{zz}$. A measurement of

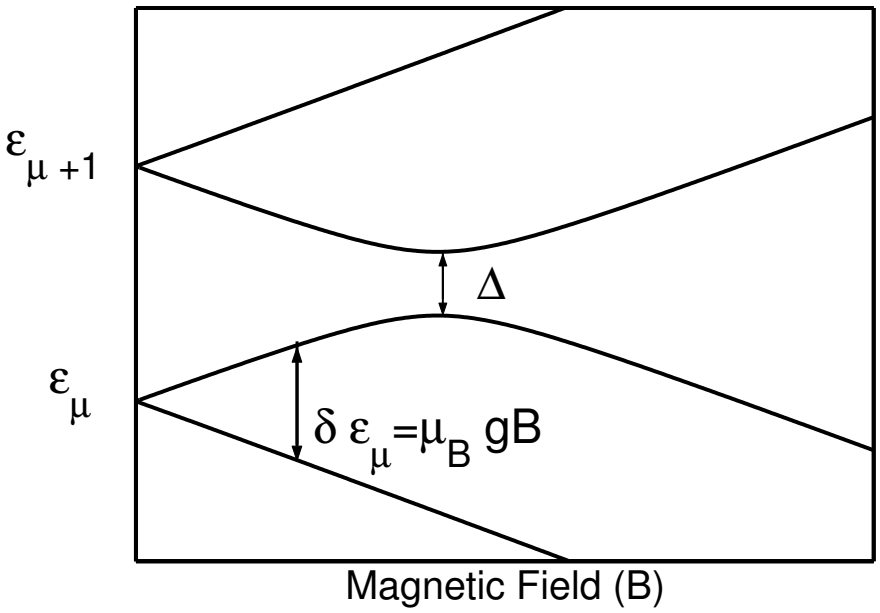

Figure 3.1: A cartoon showing the definitions of the g-factors and the avoided crossing energy Δ. At zero magnetic field, all energy levels ε_μ are doubly degenerate. A magnetic field splits these doublets. The g-factor measures the size of the splitting of a doublet ε_μ as a function of magnetic field, see Eq. (3.1). The avoided crossing energy Δ is the minimum distance at the first avoided crossing of neighboring energy levels, see Sec. 3.4.

full g tensors in Cu grains was reported quite recently [9]. Again, good agreement was found between the experimentally measured g-tensor distribution and RMT.

The effect of the spin-orbit interaction on the wavefunctions in a metal grain can be described by a dimensionless parameter λ,

$$\lambda^2 = \frac{\pi\hbar}{\tau_{\rm so}\delta}, \tag{3.3}$$

where $\tau_{\rm so}$ is the spin-orbit scattering time and δ is the mean spacing between Kramers' doublets in the grain (in the absence of the magnetic field). The effects of spin-orbit scattering are weak if $\lambda \ll 1$. In that case, wavefunctions are real and

have a well-defined spin; the electron magnetic moment is close to its vacuum value $g = 2$. In the opposite limit of strong spin-orbit scattering, $\lambda \gg 1$, wavefunctions are complex and have no well-defined spin. Hence, the spin contribution to the electron's magnetic moment is strongly suppressed, compared to the case of electrons in vacuum. However, in addition to a contribution from the electron's spin, there may be a significant orbital contribution to the magnetic moment carried by a single electron if spin-orbit scattering is present: wavefunctions are complex, and hence current-carrying [11].

Experimental estimates of λ are close to zero in Al and range from 0.7 in a small Cu grain ($\delta \approx 0.7$ meV) to 13 in a larger Au grain ($\delta \approx 0.1$ meV) [8]. A full theory of the combined orbital and spin contributions to the g tensor was developed for the asymptotes $\lambda \ll 1$ and $\lambda \gg 1$ only [11, 12]. Both theories calculate distributions normalized to the average $(\langle g^2 \rangle)^{1/2}$. In addition, Matveev *et al.* calculate both spin and orbital contributions to $(\langle g^2 \rangle)^{1/2}$, while Ref. [12] considered the spin contribution only. The case of intermediate λ, necessary for a quantitative comparison with the experiments of Ref. [8], was studied in Ref. [12] using numerical diagonalization of a random matrix model with variable spin-orbit scattering strength, but without inclusion of the orbital contribution to the magnetization.

In this chapter we construct a random matrix theory that describes both spin and orbital contributions to the electron g tensor. In the limit $\lambda \gg 1$ our model reproduces the g tensor distribution found in Refs. [11, 12], but it also provides a simple model to numerically obtain the full g tensor distribution for arbitrary spin-orbit scattering strength. In addition to the distribution of the g tensor we also look at the correlator of g tensors of neighboring levels. While g tensors are

not correlated for $\lambda = 0$ and, as we show here, for $\lambda \gg 1$; we find that correlations can be substantial for λ of order unity. The random-matrix model is formulated in Sec. 3.2; the g tensor distributions are considered in Sec. 3.3.

In addition to the g factors, which describe the magnetic-field dependence of the energy levels at very small magnetic fields, Salinas *et al.* obtained additional information on the magnitudes of spin-orbit scattering matrix elements from avoided crossings of energy levels at higher magnetic fields: For weak spin-orbit scattering, the minimal energy separation Δ in an avoided crossing between the downward moving level $\varepsilon_{\mu+1,-}$ and the upward moving level $\varepsilon_{\mu,+}$ is twice the matrix element of the spin-orbit coupling between the corresponding eigenstates,[5] see Fig. 3.1. In Sec. 3.4 we calculate the avoided crossing energy Δ from the random matrix model, and find its statistical distribution and dependence on the direction of the magnetic field $\mathbf{B}$.

3.2 Random matrix model

In this section we formulate a random-matrix model that describes the magnetic-field dependence of energy levels in a metal grain with spin-orbit scattering, taking into account both the Zeeman and the orbital effects of the magnetic field. Following the basic premises of random matrix theory, we replace the Hamiltonian of the metal grain by a $2N \times 2N$ matrix $\mathcal{H}$,

$$\mathcal{H}(\lambda) = H_{\mathrm{GOE}} + \frac{\lambda}{\sqrt{N}} H_{\mathrm{GSE}} + H_B. \tag{3.4}$$

The first two terms on the right hand side of Eq. (3.4) describe the Hamiltonian in the absence of the magnetic field; the last term H_B describes the effect of the magnetic field. We use the convention that the random matrices H_{GOE}, H_{GSE}, and

H_B have the dimension of energy.

Without the magnetic field, $\mathcal{H}$ is taken from an ensemble that interpolates between the Gaussian Orthogonal and Gaussian Symplectic ensembles of random matrix theory. The Gaussian Orthogonal Ensemble (GOE), which is relevant for metal grains without spin-orbit scattering, consists of real symmetric $N \times N$ matrices with independently and Gaussian distributed elements, multiplied by the 2×2 unit matrix 1_2 in spin space,

$$H_{\rm GOE} = S \otimes 1_2, \quad P(S) \propto e^{-(\pi^2/4N\delta^2)\mathrm{tr}\, S^{\rm T} S}. \tag{3.5}$$

Here δ is the mean level spacing in the metal grain (i.e., the mean spacing of the Kramers' doublets). The Gaussian Symplectic Ensemble (GSE), which describes metal grains with strong spin-orbit scattering, consists of self-dual quaternion matrices [14]. A Hamiltonian taken from the GSE can be parameterized as

$$H_{\rm GSE} = \frac{1}{2}\left(A_0 \otimes 1_2 + i \sum_{j=1}^{3} A_j \otimes \sigma_j \right), \tag{3.6}$$

where A_0 is a real symmetric $N \times N$ matrix and the A_j, $j = 1, 2, 3$, are real and antisymmetric $N \times N$ matrices. The four matrices A_0, A_1, A_2, and A_3 have independently and Gaussian distributed elements,

$$P(A_j) \propto e^{-(\pi^2/4N\delta^2)\mathrm{tr}\, A_j^{\rm T} A_j}, \quad j = 0, 1, 2, 3. \tag{3.7}$$

The crossover parameter λ describes the strength of the spin-orbit scattering in the Hamiltonian of Eq. (3.4). The cases $\lambda = 0$ and $\lambda \to \infty$ correspond to the GOE and GSE, respectively.

The effect of the magnetic field $\mathbf{B} = (B_1, B_2, B_3)$ is described by the term H_B in Eq. (3.4),

$$H_B \;=\; \sum_{j=1}^{3} B_j M_j, \tag{3.8}$$

where the $2N \times 2N$ matrices M_j $(j = 1, 2, 3)$ are given by

$$M_j = \mu_B \left(1_N \otimes \sigma_j + i \frac{\pi\eta}{\delta\sqrt{N}} X_j \otimes 1_2 \right), \tag{3.9}$$

where the X_j, $j = 1, 2, 3$, are real antisymmetric matrices, with independent and Gaussian distributions,

$$P(X_j) \propto e^{-(\pi^2/4N\delta^2)\mathrm{tr}\, X_j^{\mathrm{T}} X_j}. \tag{3.10}$$

The first term in Eq. (3.9) describes the coupling of the magnetic field to the electron spin; the second term, which is diagonal in spin space, describes the coupling of the magnetic field to the orbital angular momentum. The second term in Eq. (3.9) was originally proposed by Pandey and Mehta to describe the orbital effect of a time-reversal symmetry breaking magnetic field on the statistics of energy levels.[15, 16] For a diffusive spherical grain with radius R, mean free path l, and effective electron mass m^*, the coefficient η is given by[17]

$$\eta^2 = (m/m^*)^2 \frac{l}{5R}, \tag{3.11}$$

whereas for a ballistic sphere with diffuse boundary scattering, one has

$$\eta^2 = (m/m^*)^2 \frac{1}{8}. \tag{3.12}$$

At the end of the calculation, the limit $N \to \infty$ is taken. Without the orbital term, the Hamiltonian $\mathcal{H}$ of Eq. (3.4) is the same as the random-matrix Hamiltonian used by Brouwer, Waintal and Halperin in Ref. [12].

The derivation of the numerical coefficient for the ballistic case in Ref. [17] contains a mistake. Following appendix C of Ref. [17], for a ballistic sphere with diffuse boundary scattering one has $\eta^2 = (3/4m^{*2}v_F R^3) \int dt \langle L_z(0) L_z(t) \rangle = (m^2/4m^{*2}R^3) \langle |\mathbf{r}_0 \times \mathbf{r}_1|^2 / |\mathbf{r}_0 - \mathbf{r}_1| \rangle$, where L_z is the orbital angular momentum in

the z-direction and the average is taken over all classical trajectories in the sphere. Each trajectory is characterized by the points $\mathbf{r}_i$ of reflection from the surface; $\mathbf{r}_0$ and $\mathbf{r}_1$ are the points of reflection immediately before and after time $t = 0$. The joint distribution of $\mathbf{r}_0$ and $\mathbf{r}_1$ is $P(\mathbf{r}_0, \mathbf{r}_1) = (3/(16\pi R^5))|\mathbf{r}_0 - \mathbf{r}_1|$. The factor $|\mathbf{r}_0 - \mathbf{r}_1|$, which was not taken into account in Ref. [17], follows from the constraint that $\mathbf{r}_0$ and $\mathbf{r}_1$ are last and first boundary points before and after time $t = 0$, instead of an arbitrary pair of boundary points along the trajectory. (The flight time between $\mathbf{r}_0$ and $\mathbf{r}_1$, and hence the probability to be between $\mathbf{r}_0$ and $\mathbf{r}_1$ at $t = 0$, is proportional to $|\mathbf{r}_0 - \mathbf{r}_1|$.) Performing the double integration over the surface of the sphere then gives Eq. (3.12).

The g tensor $\mathcal{G}$ and the avoided crossing energy Δ will be expressed in terms of matrix elements involving the eigenvectors of the Hamiltonian (3.4). Eigenvectors ψ_μ of the Hamiltonian (3.4) are $2N$ component complex vectors. Their elements are denoted as $\psi_\mu(n, \sigma)$, where $n = 1, \ldots, N$ refers to the "orbital" degrees of freedom, and $\sigma = \pm 1$ to spin. At zero magnetic field, all eigenvalues of the Hamiltonian (3.4) are twofold degenerate (Kramers' degeneracy): each eigenvalue ε_μ ($\mu = 1, \ldots, N$) has two orthogonal eigenvectors ψ_μ and $\mathcal{T}\psi_\mu$ where $\mathcal{T}\psi(n, \sigma) = \sigma\psi^*(n, -\sigma)$, is the time-reversed of ψ. In the GOE ($\lambda = 0, B = 0$), the eigenvectors ψ_μ and $\mathcal{T}\psi_\mu$ can be chosen such that $\psi_\mu(n, +1) = -\mathcal{T}\psi_\mu(n, -1)$ is a real number and $\psi_\mu(n, -1) = \mathcal{T}\psi_\mu(n, 1) = 0$. In that case, the nonzero elements $\psi_\mu(n, +1)$ are independently and Gaussian distributed with zero mean and with variance $1/N$ [14]. (Of course, any linear combination of ψ_μ and $\mathcal{T}\psi_\mu$ forms a valid pair of eigenvectors for the eigenvalue ε_μ as well.) In the GSE ($\lambda \to \infty$, $B = 0$), the elements of ψ_μ are complex numbers with independent and Gaussian distributions with variance $1/2N$. In both the GSE and the GOE different eigenvectors are

statistically uncorrelated.

In the crossover between GOE and GSE, the eigenvector distribution is more complicated than in each of the two basic ensembles. Unlike for the cases of the pure GOE and GSE, eigenvectors at different energy levels are correlated, so that it is no longer sufficient to look at the distribution of one eigenvector alone (see Chap. 2). Since orthogonal invariance is preserved throughout the GOE-GSE crossover, the problem of finding the (joint) distribution of one or more eigenvectors in the crossover ensemble can be simplified by considering their orthogonal invariants first. For each pair of eigenstates ψ_μ and ψ_ν, the invariants are four quaternion numbers $\rho^j_{\mu\nu}$, $j = 0, 1, 2, 3$. If we diagonalize $\mathcal{H}$, writing

$$\mathcal{H}(B = 0) = U(E \otimes 1_2)U^\dagger, \tag{3.13}$$

where U is the symplectic eigenvector matrix and the $N \times N$ diagonal matrix E contains the eigenvalues ε_μ on the diagonal, they are

$$\begin{aligned} \rho^0_{\mu\nu} &= [U^\dagger U]_{\mu\nu} \\ &= \delta_{\mu\nu} 1_2 \end{aligned} \tag{3.14}$$

$$\begin{aligned} \rho^j_{\mu\nu} &= i[U^\dagger \sigma_j U]_{\mu\nu} \\ &= \begin{pmatrix} (\rho^j_{\mu\nu})_{++} & (\rho^j_{\mu\nu})_{+-} \\ (\rho^j_{\mu\nu})_{-+} & (\rho^j_{\mu\nu})_{--} \end{pmatrix}, \quad j = 1, 2, 3. \end{aligned} \tag{3.15}$$

The $\rho^j_{\mu\nu}$ satisfy a criterion of anti-hermiticity,

$$\rho^j_{\mu\nu} = -(\rho^j_{\nu\mu})^\dagger, \quad j = 1, 2, 3. \tag{3.16}$$

The orthogonal invariants $\rho^0_{\mu\nu}$ express orthonormality of the eigenvectors ψ_μ and $\mathcal{T}\psi_\mu$. The remaining orthogonal invariants $\rho^j_{\mu\nu}$ are characteristic for the crossover and determine to what extend spin-rotation symmetry has been broken. In the

GOE, we have: $\sum_k \mathrm{tr}(\rho^i_{\mu\mu}\sigma_k)\mathrm{tr}(\rho^j_{\mu\mu}\sigma_k) = 4\delta_{ij}$, while $\rho^j_{\mu\nu} = 0$ if $\mu \neq \nu$; in the GSE, $\rho^j_{\mu\nu} = 0$ for all μ and ν. An average involving different eigenvectors is then calculated in two steps: First, eigenvector elements have a Gaussian distribution with zero mean and with variance determined by the orthogonal invariants as shown in Chap. 2. In spinor notation, where $\psi(n)$ denotes the 2-component spinor with elements $\psi(n,+1)$ and $\psi(n,-1)$, these variances are

$$\begin{aligned}
\langle\psi_\mu(n)^\dagger\psi_\nu(m)\rangle &= \frac{\delta_{mn}}{N}\delta_{\mu\nu}, \\
i\langle\psi_\mu(n)^\dagger\sigma_j\psi_\nu(m)\rangle &= \frac{\delta_{mn}}{N}(\rho^j_{\mu\nu})_{++}, \\
\langle\psi_\mu(n)^{\mathrm{T}}\sigma_2\psi_\nu(m)\rangle &= 0, \\
\langle\psi_\mu(n)^{\mathrm{T}}\sigma_2\sigma_j\psi_\nu(m)\rangle &= \frac{\delta_{mn}}{N}(\rho^j_{\mu\nu})_{-+}.
\end{aligned} \tag{3.17}$$

With the help of Eq. (3.17) any average over eigenvectors can be expressed in terms of the orthogonal invariants involved in the problem.

What remains is to find the average over a small number of orthogonal invariants. For strong spin-orbit scattering, $\lambda \gg 1$, it was surmised that the distribution of the $\rho^j_{\mu\nu}$ for the $2N \times 2N$ crossover Hamiltonian (3.4) is equal to the distribution of the same quantities for a GSE Hamiltonian of a smaller size $2N'$,(see Chap. 2)

$$\begin{aligned}
N' &= \lambda^2 N(\lambda^2 + 2N)/(\lambda^2 + N)^2 \\
&\to 2\lambda^2 \quad \text{if } N \to \infty,
\end{aligned} \tag{3.18}$$

provided the energy difference $|\varepsilon_\mu - \varepsilon_\nu| \ll \lambda^2\delta$. This means that the elements of the matrix ρ^j are uncorrelated and that they have a Gaussian distribution with variance

$$\begin{aligned}
\langle|(\rho^j_{\mu\nu})_{++}|^2\rangle &= \frac{1}{2N}, \\
\langle|(\rho^j_{\mu\nu})_{+-}|^2\rangle &= \frac{1+\delta_{\mu\nu}}{2N}.
\end{aligned} \tag{3.19}$$

A similar surmise was proposed in Chap. 2 for the eigenvector statistics in the crossover between the GOE and the Gaussian Unitary Ensemble (GUE) of random-matrix theory. We are not aware of a formal proof of the surmise, although Eq. (3.19) can be obtained from diagrammatic perturbation theory if $\mu \neq \nu$ (see Chap. 2 for the crossover GOE-GUE) and Eq. (3.19) is in excellent agreement with numerical simulations (see Ref. [12] for the case $\mu = \nu$). The motivation underlying this surmise becomes clear once we consider the crossover Hamiltonian (3.4) in the eigenvector basis of $H_{\rm GOE}$ (as in Chap. 2). In this basis, eigenvectors of the crossover Hamiltonian are "localized": they are mainly built up from eigenvectors of $H_{\rm GOE}$ with energies inside a window of size $\sim N'\delta$ (with N' to be determined later). Since changing to the GOE basis does not change orthogonal invariants, we can calculate the $\rho^j_{\mu\nu}$ using an effective $2N' \times 2N'$ Hamiltonian that contains the $2N'$ relevant GOE eigenvectors only, if $|\mu - \nu| \ll N'$. As the spin-rotational symmetry breaking term is large for the effective Hamiltonian, its distribution is that of the GSE, not a crossover. The exact relation (3.18) between N' and N is found matching the distributions of a single orthogonal invariant $\rho^j_{\mu\mu}$ in the crossover Hamiltonian and in the GSE [12].

In the following two sections, the random matrix model (3.4) will serve as a starting point for analytical calculations of the g tensor distribution and avoided crossing energies in the regimes of weak spin-orbit scattering, $\lambda \ll 1$, and of strong spin orbit scattering, $\lambda \gg 1$, and for numerical calculations of the g-tensor distribution in the crossover regime $\lambda \approx 1$. The case of weak spin-orbit scattering can be treated using perturbation theory in λ; for strong spin-orbit scattering, we use the full eigenvector distribution of the GOE-GSE crossover Hamiltonian and the surmise for the orthogonal invariants that was discussed in this section.

3.3 Statistics of the g tensor

A typical plot of the magnetic field dependence of energy levels is shown in Fig. 3.1. A magnetic field $\mathbf{B} = B\hat{B}$ splits the Kramers' doublets ε_μ into pairs $\varepsilon_{\mu,\pm}$ that depend linearly on the magnitude B of the magnetic field,

$$\varepsilon_{\mu,\pm} = \varepsilon_\mu \pm \frac{1}{2}\delta\varepsilon_\mu, \tag{3.20}$$

with $\delta\varepsilon_\mu$ expressed in terms of the g tensor $\mathcal{G}_\mu$ as in Eq. (3.2) above.

Following Ref. [12], the g tensor can be written as

$$\mathcal{G} = G^{\mathrm{T}}G, \tag{3.21a}$$

where the 3×3 matrix G has elements

$$\begin{aligned} G_{1j} &= \frac{2}{\mu_B}\mathrm{Re}\,\langle\psi_\mu|M_j|\mathcal{T}\psi_\mu\rangle, \\ G_{2j} &= \frac{2}{\mu_B}\mathrm{Im}\,\langle\psi_\mu|M_j|\mathcal{T}\psi_\mu\rangle, \\ G_{3j} &= \frac{2}{\mu_B}\langle\psi_\mu|M_j|\psi_\mu\rangle, \end{aligned} \tag{3.21b}$$

where M_j is defined in Eq. (3.9), ψ_μ is an eigenvector of $\mathcal{H}$ at $B = 0$ with eigenvalue ε_μ, and $\mathcal{T}\psi_\mu$ is its time-reversed.

The tensor $\mathcal{G}$ has three eigenvectors and three eigenvalues g_j^2, $j = 1, 2, 3$. The eigenvectors are referred to as "principal axes", the eigenvalues g_1, g_2, and g_3 as "principal g-factors". The three principal g factors describe the splittings of the doublet for magnetic fields along each of the three principal axes. We describe the distribution of the g tensor in terms of the distributions of its eigenvectors (the principal axes) and eigenvalues (the principal g-factors). For a roughly spherical grain, the principal axes will be oriented randomly in space. Hence, it remains to find the distribution of the three principal g factors $g_{\mu,1}$, $g_{\mu,2}$, and $g_{\mu,3}$. We will now consider the cases of weak and strong spin-orbit scattering separately.

3.3.1 Weak spin-orbit scattering

In this section we consider the case of weak spin-orbit scattering, $\lambda \ll 1$ using perturbation theory. Expanding for small λ and keeping only the leading terms of order $\lambda\eta$ and λ^2, we find that the g tensor reads

$$\begin{aligned} \mathcal{G}_{\mu;ij} &= 4\left(\delta_{ij} + \frac{\eta\lambda\pi}{N\delta}\sum_{\nu\neq\mu}\frac{X_i^{\mu\nu}A_j^{\mu\nu} + A_i^{\mu\nu}X_j^{\mu\nu}}{\varepsilon_\mu - \varepsilon_\nu}\right. \\ &\quad \left. -\frac{\lambda^2}{N}\sum_{\nu\neq\mu}\frac{\delta_{ij}\sum_{k=1}^{3}(A_k^{\mu\nu})^2 - A_i^{\mu\nu}A_j^{\mu\nu}}{(\varepsilon_\mu - \varepsilon_\nu)^2}\right). \end{aligned} \tag{3.22}$$

Here ε_μ and ε_ν are eigenvalues of the Hamiltonian (3.4) at zero magnetic field and without spin-orbit scattering, and $A_j^{\mu\nu}$ and $X_j^{\mu\nu}$ are the matrix element of the matrices A_j and X_j between the corresponding eigenvectors $|\psi_\mu\rangle$ and $|\psi_\nu\rangle$ of $\mathcal{H}$, respectively, cf. Eqs. (3.6) and (3.9). While Eq. (3.22) assumes that λ is small, $\lambda \ll \min(1, \eta^{-1})$, no requirement is necessary for the parameter η that sets the scale for the orbital contribution to the magnetization.

The term proportional to $\lambda\eta$ in Eq. (3.22) corresponds to orbital paramagnetism. It is of first order in the spin-orbit coupling strength λ because the orbital contribution appears as soon as the wavefunction is complex, which happens to first order in λ. The term proportional to λ^2 is a reduction of the Pauli paramagnetism caused by interaction with other energy levels. For the case of $i = j = 3$, this term agrees with earlier work by Sone [18].

The distribution of $\mathcal{G}$ without the orbital contribution (second term in Eq. (3.22)) was studied in Refs. [11] and [12]. We find, however, that for very small spin-orbit scattering, this orbital contribution dominates the g tensor fluctuations. Notice that whereas the Zeeman contribution always gives g factors smaller than two — the last term in Eq. (3.22) is negative definite — the orbital contribution can be of arbitrary sign, allowing for principal g factors larger than two.

To illustrate this feature, we calculate the tails of the joint distribution $P(g_1, g_2, g_3)$ of the three principal g factors. The distribution of the tails is dominated by events where the spacing between the level ε_μ and one of its neighbors $\varepsilon_{\mu+1}$ or $\varepsilon_{\mu-1}$ is exceptionally small, of order $\lambda\delta$ or $\lambda\eta\delta$ (whichever is larger). Hence, the tails of $P(g_1, g_2, g_3)$ can be calculated limiting attention to the nearest-neighbor terms in the summations in Eq. (3.22). Keeping only the contribution from $\nu = \mu - 1$ or $\nu = \mu + 1$ (depending on which level is closer to ε_μ) in Eq. (3.22), we have

$$\begin{aligned} \mathcal{G}_\mu &= 4\left[1_3 + \frac{\eta\lambda\pi}{N\delta s}\left(\mathbf{X}\mathbf{A}^{\mathrm{T}} + \mathbf{A}\mathbf{X}^{\mathrm{T}}\right)\right. \\ &\quad \left. - \frac{\lambda^2}{Ns^2}\left(|\mathbf{A}|^2 1_3 - \mathbf{A}\mathbf{A}^{\mathrm{T}}\right)\right], \end{aligned} \tag{3.23}$$

where $s = \min|\varepsilon_\mu - \varepsilon_{\mu\pm1}|$ is the nearest neighbor energy splitting. For small s, the distribution $P(s)$ is given by $P(s) = \pi s/\delta^2 + \mathcal{O}(s^2)$. (Note that this is twice the result for the small-spacing asymptote of the level-spacing distribution in the GOE,[14] since s is the minimum of two level spacings.) Further, $\mathbf{A}$ and $\mathbf{X}$ are shorthand notation for the vectors with components $A_j^{\mu,\mu\pm1}$, and $\mp X_j^{\mu,\mu\pm1}$ $(j = 1, 2, 3)$ respectively. These are vectors of random Gaussian variables whose distributions are given in Eq. (3.7) and Eq. (3.10), respectively.

We order the three principal g factors as $g_1 < g_2 < g_3$ and parameterize them as $g_j = 2(1 + y_j)$, $j = 1, 2, 3$. With this notation, the tails of the distribution correspond to $\max(\lambda^2, \lambda\eta) \ll |y_j| \ll 1$ for at least one of the y_j. The tails of the distribution are found to be

$$\begin{aligned} P(y_1 < y_2 < y_3) &= \frac{3(\pi\lambda)^2}{8\eta^3}\Theta(-y_2) \\ &\times \frac{y_3 - y_1}{(-\pi y_2)^{7/2}} \exp\left[\frac{(y_1 - y_2 - y_3)^2 + 4(y_1 - y_2)y_2}{4\eta^2 y_2}\right], \end{aligned} \tag{3.24}$$

where $\Theta(x) = 1$ for $x > 0$, and $\Theta(x) = 0$ for $x < 0$. We then proceed to analyze

Eq. (3.24) in the cases of weak orbital contribution ($\eta \ll \lambda$) and the case where the orbital term dominates ($\lambda \ll \eta \ll \lambda^{-1}$).

In the limit $\eta \ll \lambda$ the tail of the distribution factors as

$$P(y_1 < y_2 < y_3) \;\; \propto \;\; \frac{y_3 - y_1}{\eta^3 (-y_2)^{7/2}} \exp\left[\frac{y_1 - y_2}{\eta^2} + \frac{y_3^2}{4\eta^2 y_2}\right],$$

reproducing the result

$$P = \frac{3\lambda^2}{4\pi y_2^2} \delta(y_3)\delta(y_2 - y_1) \tag{3.25}$$

for the tail of the g tensor distribution obtained in Ref. [12] in the limit $\eta \to 0$. This result is valid for $\lambda^2 \ll |y_1|, |y_2| \ll 1$.

In the opposite limit $\lambda \ll \eta \ll \lambda^{-1}$, Eq. (3.24) simplifies to

$$P(y_1, y_2, y_3) \;\; = \;\; \frac{9\eta^2 \lambda^2 \Theta(-y_1)\delta(y_2)\Theta(y_3)}{\pi (y_1 - y_3)^4}, \tag{3.26}$$

which is valid if $\lambda\eta \ll |y_{1,3}| \ll 1$.

In Fig. 3.2 we have shown the distributions of the principal g factors g_1, g_2, and g_3, calculated from the random matrix model (3.4) using numerical diagonalization. Although the limits (3.25) and (3.26) were derived for the tail of the g-tensor distribution only, they can account for some qualitative features of the full g-tensor distribution for weak spin-orbit scattering shown in Fig. 3.2: when the orbital contribution to the g tensor dominates ($\eta \gg \lambda$), generically $g_3 > 2$, $g_2 \approx 2$, and $g_1 < 2$, cf. Eq. (3.26). On the other hand, when the Zeeman contribution to the g tensor dominates ($\eta \ll \lambda$), one typically has $g_1 \approx g_2 < 2$ and $g_3 \approx 2$, cf. Eq. (3.25).

We now turn our attention to correlations between g tensors of neighboring levels. Such correlations are described by the correlator

$$\mathcal{C}_{ij,kl} = \langle g_\mu^2 \rangle^{-2} \left(\langle \mathcal{G}_{\mu,ij} \mathcal{G}_{\mu+1,kl} \rangle - \langle \mathcal{G}_{\mu,ij} \rangle \langle \mathcal{G}_{\mu+1,kl} \rangle \right). \tag{3.27}$$

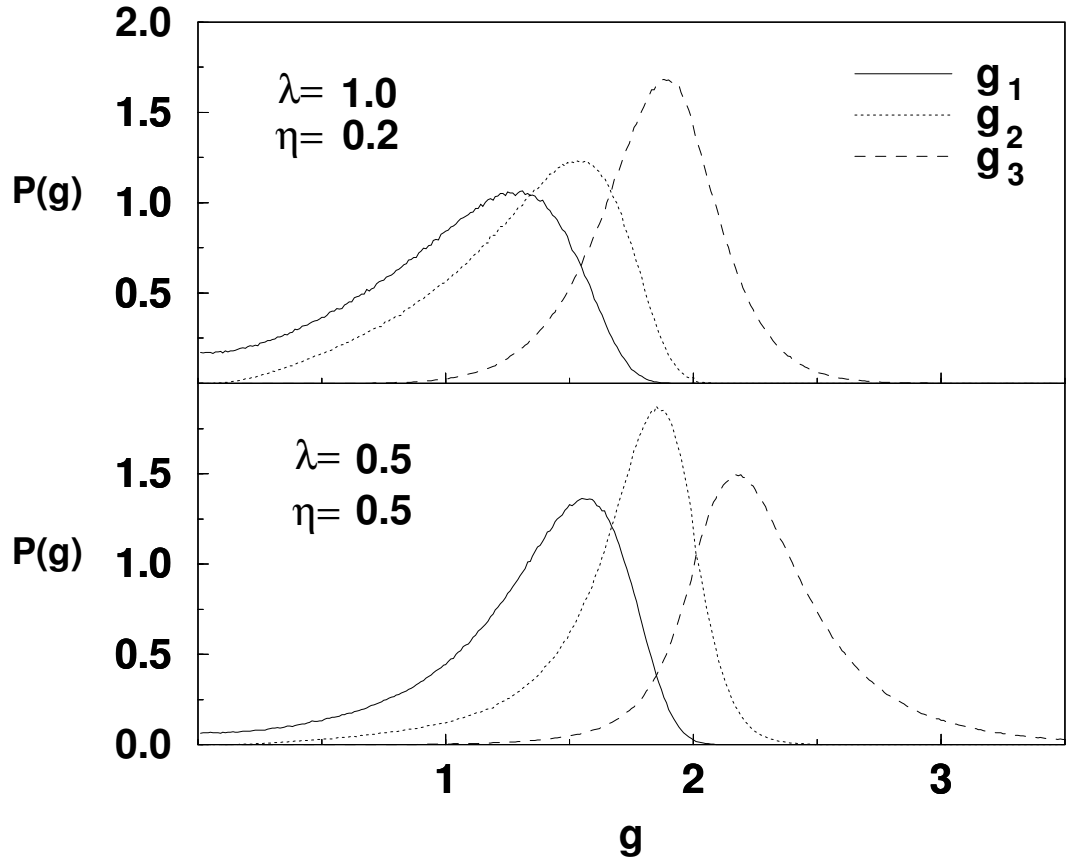

Figure 3.2: Distributions of magnitudes of the principal g factors. Upper panel: $\lambda = 1.0,\ \eta = 0.2$; Lower panel: $\lambda = \eta = 0.5$.

Calculating the correlator $\mathcal{C}$ to leading order in $\lambda \ll 1$, we find that the result is dominated by events where the levels ε_μ and $\varepsilon_{\mu+1}$ are very close. Since this contribution is formally divergent, as a result of the presence of the energy denominators in the perturbation expression (3.22), a cut off must be imposed at energy separations $\varepsilon_{\mu+1} - \varepsilon_\mu$ of order $\lambda\delta$ where the perturbation theory is not valid. To treat the contribution from nearby levels $\varepsilon_{\mu+1}$ and ε_μ correctly, we calculate the contribution from such events non-perturbatively. To leading order in $\lambda \ll 1$, the result of such a treatment amounts to the replacement of the energy denominator $\varepsilon_{\mu+1}-\varepsilon_\mu$ in Eq. (3.22) by $[(\varepsilon_{\mu+1}-\varepsilon_\mu)^2+|\mathbf{A}|^2\lambda^2/N]^{1/2}$. We then obtain the following result:

$$\begin{aligned} \mathcal{C}_{ijkl} &= \frac{\lambda^2}{\pi}(\delta_{ik}\delta_{jl}+\delta_{il}\delta_{jk})(\eta^2\ln\lambda+\frac{1}{20}) \\ &+ \frac{3\lambda^2}{10\pi}\delta_{ij}\delta_{kl}. \end{aligned} \tag{3.28}$$

The correlator between g factors (at a fixed direction of the magnetic field) is found from Eq. (3.28) setting $i=j=k=l=\hat{B}$ in the direction of magnetic field,

$$\mathcal{C} = \langle g_{\mu+1}^2 g_\mu^2\rangle/\langle g^2\rangle^2 - 1 = \frac{2\lambda^2}{\pi}\left(\eta^2\ln\lambda+\frac{1}{5}\right). \tag{3.29}$$

3.3.2 Strong spin-orbit scattering

In the regime of a strong spin-orbit scattering, $\lambda \gg 1$, the g tensor distribution can be calculated from Eq. (3.21) using the known distribution of the eigenvectors of the random Hamiltonian (3.4) at zero magnetic field, see Sec. 3.2. We then find that the matrix elements of the 3×3 matrix G of Eq. (3.21) are Gaussian random numbers, with zero mean and with variance $1/\lambda^2+2\eta^2$. The distribution of the eigenvalues of the g-tensor $\mathcal{G}$ then follows from standard results in Random Matrix

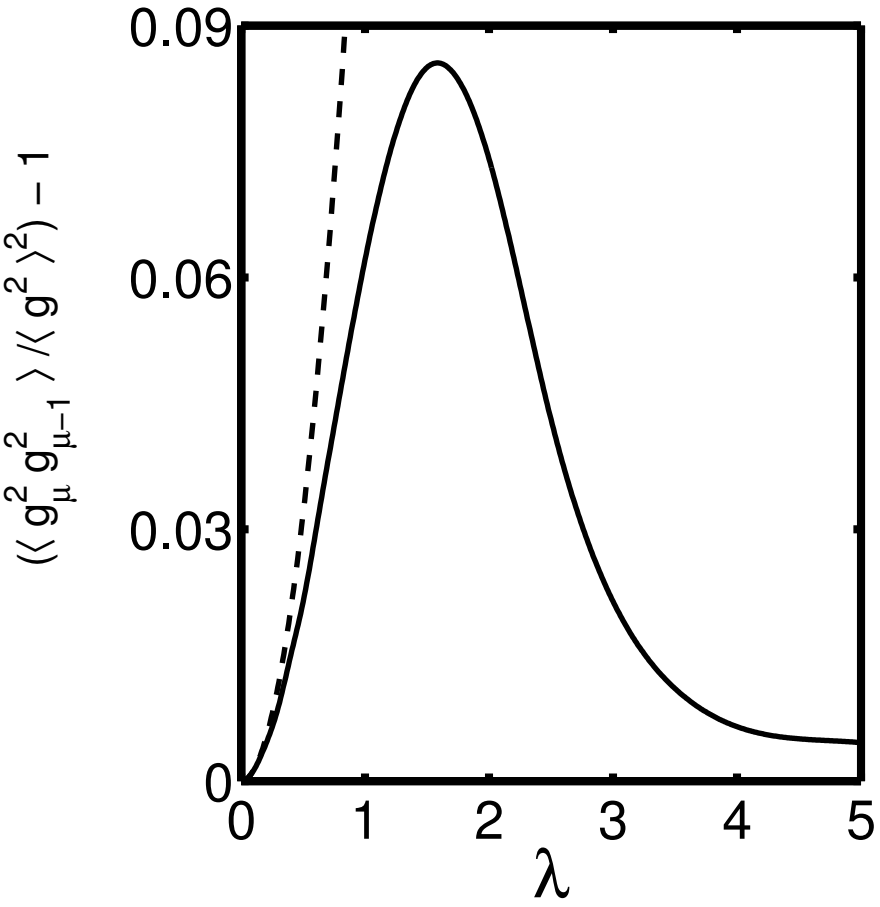

Figure 3.3: g-factor correlation as a function of spin-orbit coupling λ computed numerically for 200×200 GOE-GSE crossover matrices. Dashed line shows the result from perturbation theory Eq. (3.29).

Theory [19]. From this we conclude that the distribution of the principal g factors is [12]

$$P(g_1, g_2, g_3) \propto \left(\prod_{i<j} |g_i^2 - g_j^2| \right) \prod_i e^{-3g_i^2/2\langle g^2 \rangle}, \tag{3.30}$$

where

$$\langle g^2 \rangle = \frac{1}{3}\langle g_1^2 + g_2^2 + g_3^2 \rangle = \frac{3}{\lambda^2} + 6\eta^2. \tag{3.31}$$

Values for η for diffusive and ballistic spherical grains are given in Eqs. (3.11) and (3.12). Equations (3.30) and (3.31) extend the result of Ref. [12] to the case $\eta \neq 0$. Equation (3.31), which was derived using the random matrix model (3.4), agrees with the results of Matveev *et al.*, which were derived using a comparison of the g factors and the energy absorption of a time-dependent magnetic field.

In Fig. 3.4 we show the result of numerical calculations of $\langle g^2 \rangle$ as a function of the spin-orbit scattering rate λ and for various values of η. For $\eta^2 < 2/3$, $\langle g^2 \rangle < 2$ for all λ, while for $\eta^2 > 2/3$, $\langle g^2 \rangle > 2$. The derivatives with λ are maximal near $\lambda = 0$ because of the enhanced fluctuations due to the orbital part at small λ, cf. Eq. (3.22).

Correlations between g tensors of neighboring levels trivially vanish for large λ because, in the GSE, different eigenvectors are statistically uncorrelated. However, since the average g tensor also depends on λ, it is a more meaningful question to study the correlator between g tensors, normalized by the average g factor, cf. Eq. (3.27). In the presence of an orbital contribution to the g tensor, the average g factors are nonzero for $\lambda \gg 1$, see Eq. (3.31), so that the vanishing of correlations in the GSE implies that they vanish compared to the average as well. Without the orbital contribution, g-tensor correlations cannot be addressed with reference to the eigenvector statistics in the GSE, because $\mathcal{G} = 0$ in the

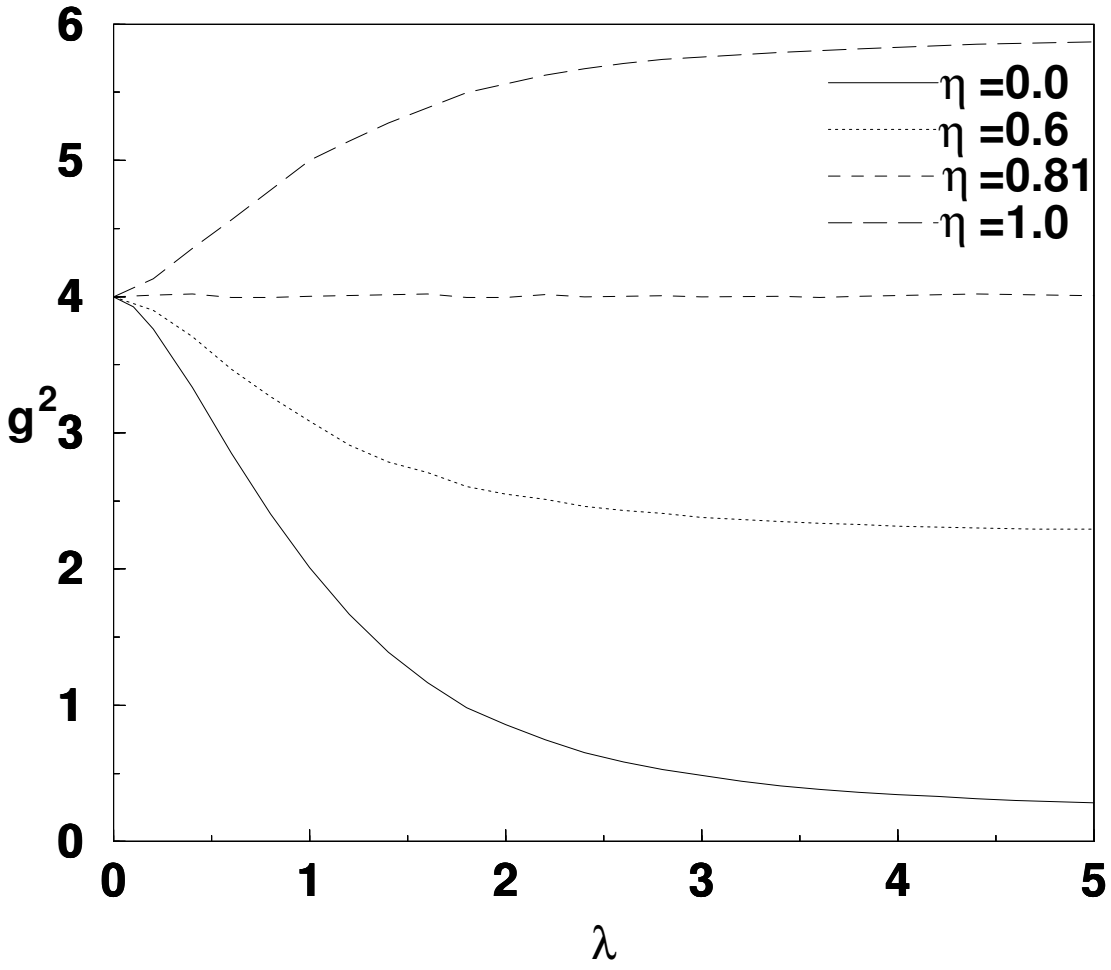

Figure 3.4: Averaged $|\mathbf{g}|^2$ as a function of spin-orbit strength λ. The critical value $\eta_0 = \sqrt{2/3} \approx 0.81$.

GSE. Instead we need the more detailed knowledge of the eigenvector distribution for large λ, which is summarized in Sec. 3.2. The main result of that section is that the eigenvector distribution depends on the distribution of certain orthogonal invariants $\rho^j_{\mu\nu}$, $j = 1, 2, 3$ which are 2×2 matrices in spin space, see. Eq. (3.17). With the help of Eq. (3.21), one easily verifies that, in the case $\eta = 0$, the g tensor may be expressed in terms of these orthogonal invariants only,

$$(\mathcal{G}_\mu)_{ij} = 2\mathrm{tr}\,\rho^i_{\mu\mu}\rho^j_{\mu\mu}, \quad i, j = 1, 2, 3, \tag{3.32}$$

where the trace is taken in spin space. Since, for $\lambda \gg 1$, the orthogonal invariants $\rho^j_{\mu\mu}$ are all independently distributed for different levels, we conclude that g tensors of different levels are uncorrelated in the case $\eta = 0$ as well.

Figure 3.3 shows the g-factor correlator (3.29) normalized by the average g factor as a function of λ. The numerical diagonalization confirms our previous conclusions that g factor correlations are small for both asymptotic regimes $\lambda \ll 1$ and $\lambda \gg 1$. Correlations are maximal for intermediate spin-orbit scattering strengths, $\lambda \sim 1.5$, but never amount to more than 10% of the average $\langle g^2 \rangle$.

3.4 Avoided crossing energies

Once the Kramers' doublets are split by the magnetic field, half of the levels move upward with slope $\sim (1/2)g\mu_B B$, while the other half moves downward with the same slope. Hence, a downward moving level $\varepsilon_{\mu+1,-}$ and the upward moving level $\varepsilon_{\mu,+}$ meet at magnetic field strength

$$B_\mathrm{c} = \frac{2(\varepsilon_{\mu+1} - \varepsilon_\mu)}{\mu_B(g_\mu + g_{\mu+1})}. \tag{3.33}$$

In fact, since the matrix element of the coupling H_B to the magnetic field between the corresponding eigenstates $|\psi_{\mu+1,-}\rangle$ and $|\psi_{\mu,+}\rangle$ is finite, the two levels do not

cross, but exhibit an avoided crossing, see Fig. 3.1. In this section we calculate the minimum distance Δ between the energy levels in the avoided crossing, its dependence on the direction $\hat{B}$ of the magnetic field, and its level-to-level fluctuations.

The avoided crossing energy is well-defined only if the magnetic field dependence of the two levels $\varepsilon_{\mu+1,-}(B)$ and $\varepsilon_{\mu,+}(B)$ is linear, the only exception being the curvature resulting from their mutual interaction at the avoided crossing. For the magnetic field strengths of interest, $B \sim B_{\rm c}$, other sources of level curvature as a function of the magnetic field, which arise both from the spin and orbital couplings in the Hamiltonian H_B of Eq. (3.8), are small if both $\lambda \ll 1$ and $\eta \ll 1$. Hence, for the purpose of calculating the avoided crossing energy Δ it is sufficient to consider the perturbative regime of small λ and small η.

Considering the Hamiltonian in the basis of states $|\psi_{\mu+1,-}\rangle$ and $|\psi_{\mu,+}\rangle$, corresponding to the energy levels $\varepsilon_{\mu+1,-}$ and $\varepsilon_{\mu,+}$ at zero magnetic field, respectively,

$$\mathcal{H} \;=\; \begin{pmatrix} \varepsilon_{\mu+1} - \frac{1}{2}\mu_B B g_\mu & \langle\psi_{\mu+1,-}|\mathcal{H}_B|\psi_{\mu,+}\rangle \\ \langle\psi_{\mu,+}|\mathcal{H}_B|\psi_{\mu+1,-}\rangle & \varepsilon_\mu + \frac{1}{2}\mu_B B g_{\mu-1} \end{pmatrix}, \tag{3.34}$$

we find that the avoided crossing energy Δ reads

$$\begin{aligned} \Delta &= 2|\langle\psi_{\mu+1,-}|\mathcal{H}_{B_{\rm c}}|\psi_{\mu,+}\rangle| \\ &= \frac{4|\varepsilon_{\mu+1} - \varepsilon_\mu|}{\mu_B(g_{\mu+1} + g_\mu)}|\langle\psi_{\mu+1,-}|\hat{B}\cdot\mathbf{M}|\psi_{\mu,+}\rangle|. \end{aligned} \tag{3.35}$$

Using first order perturbation theory in λ and η, we find

$$\Delta \;=\; \lambda\left|\hat{B}\times\left(\frac{1}{\sqrt{N}}\mathbf{A}^{\mu+1,\mu}\right)\right|, \tag{3.36}$$

plus terms of order $\lambda\eta$ which are not relevant in the regime we consider. The components of the vector $\mathbf{A}^{\mu+1,\mu}$ are matrix elements of the spin-orbit matrices A_j, $j = 1, 2, 3$ of Eq. (3.6) in the basis that diagonalizes the Hamiltonian to zeroth order in λ.

In order to find the distribution of the avoided crossing energy Δ, we write

$$\Delta = \Delta_0 \sin\theta, \tag{3.37}$$

where $0 \leq \theta \leq \pi$ is the angle between the direction $\hat{B}$ of the applied magnetic field and the vector $\mathbf{A}^{\mu+1,\mu}$. Using the known distribution (3.7) of the spin-orbit coupling matrices A_j $(j = 1, 2, 3)$, one finds that the three elements of $\mathbf{A}^{\mu+1,\mu}$ each have a Gaussian distribution with zero mean and with variance $N\delta^2/\pi^2$. Hence, we conclude that the vector $\mathbf{A}^{\mu+1,\mu}$ is randomly oriented in space, so that

$$P(\theta) = \frac{1}{2}\sin\theta, \tag{3.38}$$

and that

$$P(\Delta_0) = \frac{(\Delta_0\pi)^2\sqrt{2\pi}}{(\lambda\delta)^3} \exp\left[-\frac{1}{2}\left(\frac{\pi\Delta_0}{\lambda\delta}\right)^2\right]. \tag{3.39}$$

Equations (3.37)–(3.39) not only give the full distribution of the avoided crossing energy Δ, but also the dependence of Δ on the direction $\hat{B}$ of the magnetic field. Equations (3.37)–(3.39) can be combined to give

$$P(\Delta) = \frac{\pi^2\Delta}{(\lambda\delta)^2} \exp\left[-\frac{1}{2}\left(\frac{\pi\Delta}{\lambda\delta}\right)^2\right]. \tag{3.40}$$

The latter result is relevant for comparison with experiments where the direction of the magnetic field cannot be varied [5, 8].

Figure 3.5 shows the distribution (3.40), together with results from a numerical calculation of the distribution of Eq. (3.35) using the random matrix model (3.4) for $\eta = 0$ and two different values of λ. We see that the agreement between the numerical diagonalization of the random matrix model and the distribution (3.40) calculated using first order perturbation theory in λ remains good up to $\lambda \sim 1$. [We should note, however, that the approximations leading to an avoided

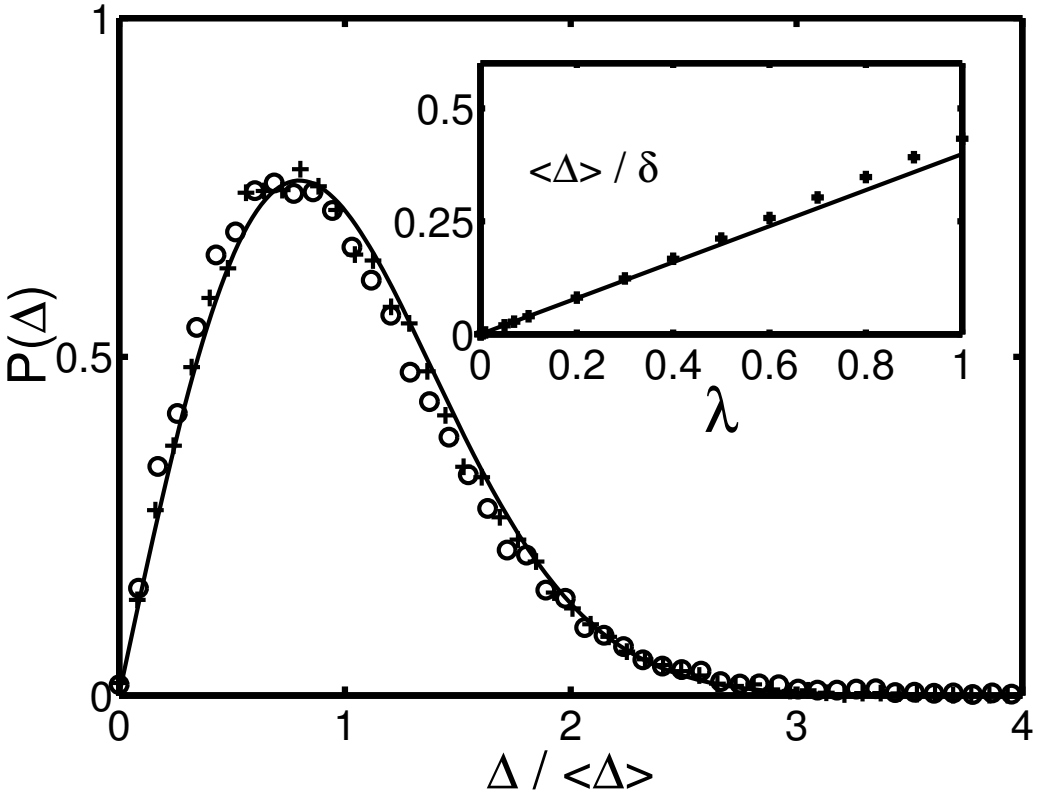

Figure 3.5: Main panel: Distribution of the avoided crossing energy Δ. Solid line is the perturbative result (3.40); the data points are from numerical evaluation of Eq. (3.35) using the numerical diagonalization of the random matrix model (3.4) with $\eta = 0$ and $\lambda = 0.2$ (crosses), and $\lambda = 0.4$ (circles). Inset: Comparison of perturbation theory (solid curve) and numerical results (data points) for the average $\langle\Delta\rangle$.

crossing energy that is dominated by matrix elements involving two neighboring levels only, is valid for $\lambda \ll 1$ and $\eta \ll 1$ only, see the discussion preceding Eq. (3.35).] Although there are corrections to $P(\Delta)$ to second order in λ, the first nonzero corrections to the average $\langle\Delta\rangle$ appear to third order in λ only.

3.5 Discussion and conclusion

In this chapter, we have presented a random matrix theory for the distributions of g tensors and avoided crossing energies in small metal grains with spin-orbit scattering. Our theory includes both the spin and the orbital effects of the magnetic field.

For large spin-orbit scattering, the main effect of the orbital contribution is to increase the typical size of the g tensor; the fluctuations (normalized by the average) and the relative magnitudes of the three principal g values are the same with and without a large orbital contribution [12]. For weak spin-orbit scattering, the presence of an orbital contribution to the g tensor not only increases the average of the g-tensor distribution, it also changes the relative magnitudes of the principal g values. Without orbital contribution, two principal g values are approximately equal and smaller than two, while the third principal g value is close to 2. If the orbital contribution is large, all three principal g values are different and, on average, symmetrically positioned around two.

Petta and Ralph have measured distributions of g factors (i.e., the square root of the $\mathcal{G}_{zz}$ element of the g-tensor) for small particles of different metals and found that distributions, if normalized to the average, were in very good agreement with the random matrix theory of Ref. [12]. The average of the distribution, however, was

up to a factor 10 smaller than the theoretical prediction (3.31) with a reasonable estimate for the parameter η [11]. A similar discrepancy between a experimental and theoretical estimates was reported in a different context by Marcus *et al.*[20] for the magnetic field scale for fluctuations of Coulomb blockade heights in two-dimensional μm-size GaAs/GaAlAs quantum dots (see also Ref. [21]). Although the experimental system studied in Refs. [20, 21] is quite different from that of Petta and Ralph, the random matrix theories describing the magnetic field dependence of Coulomb blockade peak heights and the orbital contributions to g factors are the same. At present, we do not know of a solution to either puzzle.

One complication in the search for an orbital contribution to the g factors measured in Ref. [8] is that the main effect of the orbital contribution is to change the average of the g-factor distribution only. Since, for strong spin-orbit scattering, the average g factor depends on both the dimensionless spin-orbit coupling λ and the dimensionless orbital contribution η, cf. Eq. (3.31), it is impossible to characterize what fraction of a measured g factor is the result of a state's orbital magnetic moment. The recent development of experimental methods to measure the entire g tensor[9] opens new avenues to investigate the orbital contribution. For weak spin-orbit scattering, the g-tensor distribution depends on the two parameters λ and η in a nontrivial way; even a weak orbital contribution leads to g tensors with, at least, one principal g value larger than two, see, e.g., Fig. 3.2. Hence, measurement of the full g tensors for metal grains with weak spin-orbit scattering, such as large Al grains, eventually doped with a small concentration of Au,[5] will allow the independent determination of the orbital contribution.

BIBLIOGRAPHY

[1] R. C. Ashoori, Nature **379**, 413 (1996).

[2] M. A. Kastner, Phys. Today **46**, 24 (1993).

[3] D. C. Ralph, C. T. Black, and M. Tinkham, Phys. Rev. Lett. **74**, 3241 (1995).

[4] C. W. J. Beenakker, Phys. Rev. B **44**, 1646 (1991).

[5] D. G. Salinas, S. Guéron, D. C. Ralph, C. T. Black, and M. Tinkham, Phys. Rev. B **60**, 6137 (1999).

[6] D. Davidovic and M. Tinkham, Phys. Rev. Lett. **83**, 1644 (1999).

[7] D. Davidovic and M. Tinkham, Phys. Rev. B **61**, 16359 (2000).

[8] J. R. Petta and D. C. Ralph, Phys. Rev. Lett. **87**, 266801 (2001).

[9] J. R. Petta and D. C. Ralph, Phys. Rev. Lett. **89**, 156802 (2002).

[10] W. P. Halperin, Rev. Mod. Phys. **58**, 533 (1986).

[11] K. A. Matveev, L. I. Glazman, and A. I. Larkin, Phys. Rev. Lett. **85**, 2789 (2000).

[12] P. W. Brouwer, X. Waintal, and B. I. Halperin, Phys. Rev. Lett. **85**, 369 (2000).

[13] C. P. Slichter, *Principles of Magnetic Resonance* (Springer, Berlin, 1980).

[14] M. L. Mehta, *Random Matrices*, 2 ed. (Academic Press, New York, 1991).

[15] A. Pandey and M. L. Mehta, Commun. Math. Phys. **87**, 449 (1983).

[16] C. W. J. Beenakker, Rev. Mod. Phys. **69**, 731 (1997).

[17] K. Frahm and J.-L. Pichard, J. Phys. (France) I **5**, 847 (1995).

[18] J. Sone, J. Phys. Soc. Japan **42**, 1457 (1977).

[19] E. Brézin, S. Hikami, and A. Zee, Nucl. Phys. B **464**, 411 (1996).

[20] C. M. Marcus, S. R. Patel, A. G. Huibers, S. M. Cronenwett, M. Switkes, I. H. Chan, R. M. Clarke, J. A. Folk, S. F. Godijn, K. Campman, and A. C. Gossard, Chaos, Solitons and Fractals **8**, 1261 (1997).

[21] S. M. Cronenwett, S. R. Patel, C. M. Marcus, K. Campman, and A. C. Gossard, Phys. Rev. Lett. **79**, 1312 (1997).

Chapter 4

Current induced transverse spin-wave instability in thin ferromagnets: beyond linear stability analysis

4.1 Introduction

Almost a decade ago Slonczewski [1] and Berger [2] predicted that when a spin-polarized current is passed through a ferromagnet it transfers the transverse component of its spin angular momentum to the ferromagnet. The experimental verification of the theoretical predictions followed within a few years [3, 4, 5, 6, 7]. Since then, the so-called 'spin-transfer effect' has been observed in a large number of different experiments.

In most experiments, the spin-transfer torque is studied in a ferromagnet–

normal-metal–ferromagnet tri-layer structure where a thick ferromagnet first polarizes the current which then exerts a spin-transfer torque on a second thinner ferromagnet. At sufficiently large applied current densities, the spin-transfer torque then may alter the magnetization direction of the thin magnet. The observation of hysteretic magnetic switching for one current direction only was seen as a hallmark of the spin-torque effect [6], and excluded an explanation of the experiments in terms of the magnetic field associated with the applied current. (Note that for small system sizes, the spin-transfer torque, which scales proportional to the current density, dominates over the torque exerted by the magnetic field caused by the current flow,which is proportional to the total current.) Dynamical aspects of the magnetic switching process were addressed in recent experiments [8, 9, 10, 11].

Over the past few years there has been much theoretical interest in understanding the spin-transfer torque and its consequences for hybrid ferromagnet–normal-metal devices. The connection between spin currents or spin accumulation in the normal metal spacer layer and the spin torque can be considered understood [12, 13, 14] (see Ref. [15] for a recent review). Most calculations of the response of the magnetization to the spin-transfer torque have been done in the so-called 'macrospin approximation', assuming that the ferromagnets remain single domains during spin-transfer induced switching events [16, 17, 18, 19, 20, 21]. They have addressed the precise nature of the magnetic switching process, the possibility of limit cycles, and the temperature dependence of the spin-transfer torque. In addition, full micromagnetic simulations have been done by several groups [22, 23, 24, 25], *e.g.*, to examine the effect of the Ampere field on the hysteretic switching or the breakdown of the macrospin model into quasi-chaotic dynamics at very high current densities. While the micromagnetic simulations are

a significant improvement on the macrospin approximation when it comes accounting for spatial non-uniformities in the switching process, the existing simulations derive the spin-transfer torque from an externally fixed spin current, which is a poor description of the experimental geometries in which the spin currents are determined as an intricate combination of spin polarizations caused by all ferromagnetic elements in the device [26, 12, 27, 15].

In a recent work, Polianski and Brouwer showed that a sufficiently large but unpolarized electrical current flowing perpendicular to a *single* thin ferromagnetic layer can excite spin waves in the ferromagnet [28]. These spin waves have wavevector perpendicular to the direction of current flow. The key mechanism behind the transverse spin wave instability is electron diffusion in the normal-metal contacts perpendicular to the direction of current flow, see Fig. 4.1. Electrons backscattered from the ferromagnet are spin polarized, the polarization direction being antiparallel to the direction of the magnetization at the location where they were reflected from the ferromagnet. When these electrons reach the ferromagnetic layer a second time, they typically do so at a different point at the normal-metal–ferromagnet interface. In the presence of a spin wave, the magnetization direction of the ferromagnet will be different at that point, and these electrons will transfer the perpendicular component of their spin to the ferromagnet, thus exerting a spin-transfer torque. The sign of this torque is to enhance the spin-wave amplitude. A similar argument can be made for electrons transmitted through the ferromagnet, but their torques tend to suppress the spin-wave amplitude. Typically, source and drain contacts are asymmetric, and a net spin-transfer torque is exerted on the ferromagnet. This torque leads to a spin wave instability for the current direction in which the effect of backscattered electrons dominates, and not for the other cur-

rent direction. Experiments on nanopillars a with single ferromagnetic layer found a small decrease of the device resistance above a critical current for one direction of the current and for asymmetric junctions only [29]. This finding is consistent with the theoretical prediction of a dynamic spinwave instability. A time resolved experiment, along the lines of Refs. [8, 9] could decide unambiguously whether the observation of Ref. [29] arises from a static or dynamic inhomogeneity.

For a quantitative theory of this transverse spin-wave instability, an approach that combines a full self-consistent determination of the spin-transfer torque and, at the same time, goes beyond the macrospin approximation is essential [28]. Indeed, the macrospin approximation does not allow for non-uniform spin waves in the ferromagnet, and, whereas an externally imposed spin transfer torque would predict a similar instability, a non-self-consistent theory would be quantitatively incorrect (*e.g.* predict the wrong wavelength for the spin wave) because it neglects the coupling between the spin current and the spin waves in the ferromagnet.

The possibility of current-induced non-uniform modes in heterostructures has become of recent interest in the field, both for single-layer and multilayer structures [30, 31, 32, 33, 34, 35]. In particular, Ji, Chien, and Stiles [30] reported experimental and theoretical evidence suggesting that for large ferromagnet thickness, ferromagnet–normal-metal junctions are unstable to the generation of non-uniform magnetization modes, but in this case, these are longitudinal modes (see also Refs. [6] and [36]). See also Ref. [33] for a discussion of these experiments. Further, Stiles, Xiao, and Zangwill pointed out that transverse spinwaves can be excited even in symmetric junctions if the spinwave mode is at not uniform in the direction of current flow. However, excitation of these modes requires a higher currents than the transverse spin-waves considered here [31].

Previous work [28], as well as the other theoretical works on this and related spin-wave instabilities [31, 33], was a linear stability analysis, sufficient to predict the onset of the instability, but not to describe the spin wave amplitude for current densities larger than the critical current density. Knowledge of the spin wave amplitude is necessary if one wants to study, *e.g.,* how the spin wave instability affects the resistance of the normal-metal–ferromagnet junction. It is the goal of this present work to examine in detail the dynamics of the spin-wave beyond the instability. While we focus on the case of single-layers, we expect that, in light of the work of Refs. [33, 35], our qualitative findings will carry over to the case of tri-layers and heterojunctions.

Although a quantitative description of how the spinwave instability affects the resistance of the normal-metal–ferromagnet junction will be postponed to the next two two sections, the sign of the effect can be determined using simple considerations. Once the current density has exceeded the critical current density for the spin wave excitation and a spin wave has been established, the fact that the magnetization is no longer uniform reduces the amount of spin accumulation in the normal metal contacts adjacent to the ferromagnet. A reduction of the spin accumulation in the normal metal contacts causes a reduction of the sample's resistance, see Fig. 4.2 for a schematic drawing. Indeed, the experiments of Ref. [29] observed a small decrease of the resistance of the nanopillar upon onset of the spin-wave instability. The effect of a purely transverse spinwave instability is opposite to that of a longitudinal spinwave, which increases the resistance of the device [36]. The reduction of the spin accumulation in the normal-metal spacer also lowers the spin-transfer torque, thus providing a mechanism to saturate the growth of the spin wave amplitude for current densities larger than the critical

current density. Moreover, note that a theory of this effect needs to combine features of both the micromagnetic approach and the self-consistent treatment of the spin-transfer torque.

In Sec. 4.2 we consider current densities slightly above the critical current density. In this regime, a perturbative treatment in the spin wave amplitude is possible. In Sec. 4.3 we then perform a detailed numerical simulation of a simplified system that allows us to probe current densities much larger than the critical current density. Whereas the observed magnetization dynamics in the presence of a large magnetic field is rather unsurprising — there is one stable energy minimum, and the magnetization precesses around the direction for which energy is minimal —, in the absence of an external magnetic field we find a hierarchy of instabilities. For very high currents the system shows chaotic behavior with measurable Lyapunov exponents.

4.2 Perturbative calculation

We consider a single ferromagnetic layer, connected to source and drain reservoirs, see Fig. 4.3. Between the ferromagnet and the drain reservoir is a normal-metal spacer, as is common in nanopillar geometries. There is, however, no normal-metal spacer between the ferromagnet and the source reservoir. We use coordinates x, y, z, where x is the coordinate perpendicular to the layer structure and y and z are coordinates in the plane of the layers.

Both the ferromagnet and the spacer layer have a rectangular cross section of dimensions $W_y \times W_z$. The ferromagnet has thickness d, which is taken small enough that the chemical potential for the conduction electrons and the the direction $\mathbf{m}$ of

the magnetization of the ferromagnet do not depend on the longitudinal coordinate x. The normal metal spacer has thickness L. Transport through the normal metal spacer is diffusive, with conductivity σ.

In the normal metal spacer, the charge and spin degrees of the conduction electrons are described by the equations

$$\begin{aligned} \nabla^2\mu_{\rm c} &= 0, \quad j_x = (\sigma/e)\partial_x\mu_{\rm c}, \\ l_{\rm sf}^2\nabla^2\boldsymbol{\mu}_{\rm s} &= \boldsymbol{\mu}_{\rm s}, \quad \mathbf{j}_{\rm s} = -(\hbar\sigma/2e^2)\partial_x\boldsymbol{\mu}_{\rm s}, \end{aligned} \tag{4.1}$$

where $\mu_{\rm c}$ and $\boldsymbol{\mu}_{\rm s}$ are chemical potentials for the electron density and electron spin respectively, $-e$ is the electron charge, and $l_{\rm sf}$ is the spin diffusion length in the normal metal spacer. Further, j_x is the charge current density and σ is the conductivity of the normal metal leads. The boundary conditions for $x = L$ at the drain reservoir is

$$\mu_{\rm c}(L) = -eV, \quad \boldsymbol{\mu}_{\rm s}(L) = \mathbf{0}. \tag{4.2}$$

Here the argument L refers to the x coordinate. The y and z coordinates are not written explicitly. The second boundary is the interface between the normal-metal and ferromagnet at $x = 0$. Since the electron dynamics happens on a time scale that is much faster than the rate of change of the magnetization direction $\mathbf{m}$, this boundary condition can be taken treating $\mathbf{m}$ in the adiabatic approximation [26, 27],

$$\begin{aligned} j_x(0) &= \frac{1}{e}\left[g_+\mu_{\rm c}(0) + g_-\mathbf{m}\cdot\boldsymbol{\mu}_{\rm s}(0)\right], \\ \mathbf{j}_{\rm s}(0) &= -\frac{\hbar}{2e^2}\left(g_-\mu_{\rm c}(0) + g_+\mathbf{m}\cdot\boldsymbol{\mu}_{\rm s}(0)\right)\mathbf{m} \\ &\quad + \frac{\hbar}{2e^2}g_1\left(2\boldsymbol{\mu}_{\rm s}(0)\times\mathbf{m} + \hbar\dot{\mathbf{m}}\right)\times\mathbf{m} \\ &\quad + \frac{\hbar}{2e^2}g_2\left(2\boldsymbol{\mu}_{\rm s}(0)\times\mathbf{m} + \hbar\dot{\mathbf{m}}\right). \end{aligned} \tag{4.3}$$

Here $g_\pm = (g_\uparrow \pm g_\downarrow)/2$, where $g_\uparrow$ and $g_\downarrow$ are interface conductivities for spins aligned parallel and anti-parallel to $\mathbf{m}$, and $g_1 + ig_2$ is the complex valued 'mixing interface conductivity'. The argument "0" refers to a coordinate in the normal metal spacer, just outside the ferromagnetic layer. The charge current and the spin current parallel to $\mathbf{m}$ are continuous at the interface. In writing down Eq. (4.3) we assumed that the two ferromagnet–normal-metal interfaces are identical, so that the potentials $\mu_{\rm c}$ and $\mathbf{m}\cdot\boldsymbol{\mu}_{\rm s}$ drop equally over both interfaces of the ferromagnet and that the transverse electron diffusion inside the magnetic layer is negligible. The component of $\boldsymbol{\mu}_{\rm s}$ perpendicular to $\mathbf{m}$ is then zero in the ferromagnet. (It is the non-conservation of spin current perpendicular to $\mathbf{m}$ that gives rise to the spin transfer torque.) For Co/Cu and Fe/Cr interfaces, these conductivities are tabulated, see Refs. [37, 14]. Typical values are in the range $g_2 \ll g_1 \sim g_\pm \sim 10^{14}\ \Omega^{-1}m^{-2}$. For any interface, one has the constraint $g_1 > g_+ > g_-$ [26].

We are interested in the situation in which the magnetization is allowed to vary in the direction perpendicular to the current flow. In this case a large enough current may cause spin-wave excitations perpendicular to the direction of current flow [28]. To simplify the notation, we take the limit $L \gg l_{\rm sf}$. The spin and charge chemical potentials in the normal-metal spacer then have the general solution

$$\begin{aligned}
\mu_{\rm c}(\mathbf{r}) &= \sum_{\mathbf{q}} e^{iq_y y + iq_z z} a_{\rm c}(\mathbf{q}) e^{-(q_y^2+q_z^2)^{1/2}x} + \frac{eIx}{W_y W_z \sigma}, \\
\boldsymbol{\mu}_{\rm s}(\mathbf{r}) &= \sum_{\mathbf{q}} e^{iq_y y + iq_z z} e^{-(q_y^2+q_z^2+l_{\rm sf}^{-2})^{1/2}x} \mathbf{a}_{\rm s}(\mathbf{q}),
\end{aligned} \tag{4.4}$$

where $\mathbf{q} = (0, q_y, q_z)^{\rm T}$ is a wavevector in the y-z plane. The components q_y and q_z take values $q_y = \pi n_y/W_y$, $q_z = \pi n_z/W_z$ with integers n_y and n_z. The Fourier expansion coefficients $a_{\rm c}(\mathbf{q})$ and $\mathbf{a}_{\rm s}(\mathbf{q})$ are real and satisfy

$$a_{\rm c}(\mathbf{q}) = a_{\rm c}(-\mathbf{q}), \quad \mathbf{a}_{\rm s}(\mathbf{q}) = \mathbf{a}_{\rm s}(-\mathbf{q}). \tag{4.5}$$

We further define the quantities

$$G_{\rm c}(\mathbf{q}) = (\sigma/2)(q_y^2+q_z^2)^{1/2}, \tag{4.6}$$

$$G_{\rm s}(\mathbf{q}) = (\sigma/2)(q_y^2+q_z^2+l_{\rm sf}^{-2})^{1/2}, \tag{4.7}$$

which have the same dimension as the interface conductivities $g_\pm$, g_1, and g_2. With these definitions, the boundary condition (4.3) at the normal-metal–ferromagnet interface becomes

$$\begin{aligned} 0 &= -\frac{eI}{W_yW_z} + 2\sum_{\mathbf{q}} e^{iq_y y+iq_z z}\left[G_{\rm c}(\mathbf{q})a_{\rm c}(\mathbf{q}) + g_+ a_{\rm c}(\mathbf{q}) + g_-\mathbf{a}_{\rm s}(\mathbf{q})\cdot\mathbf{m}\right], \\ 0 &= \sum_{\mathbf{q}} e^{iq_y y+iq_z z}\left[2G_{\rm s}(\mathbf{q})\mathbf{a}_{\rm s}(\mathbf{q}) + (g_- a_{\rm c}(\mathbf{q})\mathbf{m}\right. \\ &\quad \left. + g_+\mathbf{a}_{\rm s}(\mathbf{q})\cdot\mathbf{m})\mathbf{m} - 2g_1(\mathbf{a}_{\rm s}(\mathbf{q})\times\mathbf{m})\times\mathbf{m} - 2g_2\mathbf{a}_{\rm s}(\mathbf{q})\times\mathbf{m}\right] \\ &\quad - \hbar g_1\dot{\mathbf{m}}\times\mathbf{m} - \hbar g_2\dot{\mathbf{m}}. \end{aligned} \tag{4.8}$$

Although Eq. (4.8) gives a set of linear equations for the expansion coefficients $a_{\rm c}(\mathbf{q})$ and $\mathbf{a}_{\rm s}(\mathbf{q})$, a solution in closed form is not possible for arbitrary magnetization $\mathbf{m}(y,z)$. Instead, we expand around the uniform equilibrium direction. Hereto we introduce a second coordinate system with axes labeled 1, 2, and 3, such that $\mathbf{m}$ points along the unit vector $\hat{\mathbf{e}}_3$ in the absence of an applied current, and write

$$\mathbf{m} = m_1\hat{\mathbf{e}}_1 + m_2\hat{\mathbf{e}}_2 + (1-m_1^2-m_2^2)^{1/2}\hat{\mathbf{e}}_3. \tag{4.9}$$

We then perform a Fourier transform, similar to Eq. (4.4)

$$m_j(y,z) = \sum_{\mathbf{q}} m_j(\mathbf{q})e^{iq_y y+iq_z z}, \quad j=1,2, \tag{4.10}$$

where $m_j(\mathbf{q}) = m_j(-\mathbf{q})$. Finally, expanding in powers of m_1 and m_2, we have solved the spin and charge chemical potentials to third order in m_1 and m_2, which parameterize the deviations from equilibrium.

In order to complete the calculation, we need to calculate the rate of change of the magnetization direction $\mathbf{m}$ in the presence of the current I. Hereto we use the Landau-Lifshitz-Gilbert equation [38, 39],

$$\dot{\mathbf{m}} = \alpha \mathbf{m} \times \dot{\mathbf{m}} + \boldsymbol{\tau}_{\rm ex} + \boldsymbol{\tau}_{\rm an} + \boldsymbol{\tau}_{\rm ne}, \tag{4.11}$$

where α is the Gilbert damping coefficient, $\boldsymbol{\tau}_{\rm ex}$ is the torque arising from exchange, $\boldsymbol{\tau}_{\rm an}$ is the torque from the combined effect of magnetic anisotropy and an applied magnetic field, and $\boldsymbol{\tau}_{\rm ne}$ represents the current-induced spin-transfer torque. The latter reads [40]

$$\begin{aligned} \boldsymbol{\tau}_{\rm ne} &= \frac{\gamma}{Md}(\mathbf{j}_{\rm s}(0) - \mathbf{j}_{\rm s}(-d)) \times \mathbf{m}) \times \mathbf{m} \\ &= -\frac{\hbar\gamma}{Mde^2}\left[g_1(\boldsymbol{\mu}_{\rm s} \times \mathbf{m} + \hbar\dot{\mathbf{m}}) \times \mathbf{m}\right. \\ &\quad \left. + g_2(\boldsymbol{\mu}_{\rm s} \times \mathbf{m} + \hbar\dot{\mathbf{m}})\right]. \end{aligned} \tag{4.12}$$

Here the spin current $\mathbf{j}_{\rm s}(-d)$ is taken in the source reservoir, M is the magnetization per unit volume and γ is the gyromagnetic ratio. Note that the terms proportional to the time derivative $\dot{\mathbf{m}}$ have contributions from two interfaces while the contribution to the torque from the spin chemical potential has a contribution from the $x = 0$ interface only. (All potentials are zero in the source reservoir.) The exchange torque $\boldsymbol{\tau}_{\rm ex}$ is

$$\boldsymbol{\tau}_{\rm ex} = J\gamma M \nabla^2 \mathbf{m} \times \mathbf{m}, \tag{4.13}$$

where J is the exchange constant. To linear order in m_1 and m_2, the anisotropy torque $\boldsymbol{\tau}_{\rm an}$ can be written

$$\boldsymbol{\tau}_{\rm an} = -\frac{\gamma}{M}(k_1 m_1 \hat{\mathbf{e}}_1 + k_2 m_2 \hat{\mathbf{e}}_2) \times \mathbf{m}, \tag{4.14}$$

where k_1 and k_2 describe the combined effect of magnetic anisotropy and an applied magnetic field. If anisotropy dominates over the effect of a magnetic field, higher-order terms in an expansion in powers of m_1 and m_2 will be highly sample specific.

Although this case can be dealt with using the methods presented below, the result of the calculation has little predictive value if those coefficients are not known independently. Therefore, we focus on the opposite limit that the anisotropy term in Eq. (4.14) is dominated by magnetic field. Then higher-order terms in an expansion in powers of m_1 and m_2 are related to the first-order terms, and one has

$$\boldsymbol{\tau}_{\rm an} = (k\gamma/M)\hat{\mathbf{e}}_3 \times \mathbf{m}. \tag{4.15}$$

where we wrote $k_1 = k_2 = k$. For future reference, we combine the material constants J and $2k = k_1 + k_2$ into the combinations

$$q_{\rm f}^2 = \frac{k}{JM^2}, \quad j_{\rm f}^2 = \left(\frac{2e}{\hbar}\right)^2 JM^2 k, \tag{4.16}$$

which have the dimension of inverse length and current density, respectively.

We now proceed to report the result of our calculation. The lowest order result, indicated by a superscript "(0)", is

$$\begin{aligned} a_{\rm c}^{(0)}(\mathbf{q}) &= \frac{ej(g_+ + 2G_{\rm s}(0))}{g_{\rm m}(0)g_-}\delta_{\mathbf{q},0}, \\ \mathbf{a}_{\rm s}^{(0)}(\mathbf{q}) &= \frac{-ej}{g_{\rm m}(0)}\hat{\mathbf{e}}_3\delta_{\mathbf{q},0}. \end{aligned} \tag{4.17}$$

Here $j = I/W_yW_z$ is the current density and [28]

$$g_{\rm m}(\mathbf{q}) = \frac{(g_+ + 2G_{\rm s}(\mathbf{q}))(g_+ + 2G_{\rm c}(\mathbf{q}))}{g_-} - g_-. \tag{4.18}$$

Writing $\mu_{\rm c}(L) = -eV = -e(L/\sigma W_yW_z + R)I$, we conclude that the resistance R of the ferromagnetic layer is

$$R = \frac{1}{W_yW_z}\frac{\sigma/l_{\rm sf} + g_+}{g_+\sigma/l_{\rm sf} + g_+^2 - g_-^2}. \tag{4.19}$$

For the zeroth-order solution, the spin potential $\mu_{\rm s}$ is collinear with $\mathbf{m}$ throughout the sample. Hence, to that order there is no current-induced torque. This is

different when small deviations from the situation $\mathbf{m} = \hat{\mathbf{e}}_3$ are taken into account to first order. One finds that the first-order corrections $a_{\rm c}^{(1)}(\mathbf{q})$ and $a_{\rm s3}^{(1)}(\mathbf{q})$ are zero. In order to represent the first-order contributions to the transverse spin potentials $a_{\rm s1}$ and $a_{\rm s2}$, we use spinor notation, $a_{\rm s} = (a_{\rm s1}, a_{\rm s2})^{\rm T}$ and $m = (m_1, m_2)^{\rm T}$. Then, defining

$$D(\mathbf{q}) = (g_1 + G_{\rm s}(\mathbf{q}))^2 + g_2^2, \tag{4.20}$$

we find

$$\begin{aligned} a_{\rm s}^{(1)}(\mathbf{q}) &= -\frac{ej}{g_{\rm m}(0)} m(\mathbf{q}) + \frac{ej(G_{\rm s}(\mathbf{q}) - G_{\rm s}(0))}{g_{\rm m}(0) D(\mathbf{q})} \left[(g_1 + G_{\rm s}(\mathbf{q})) m(\mathbf{q}) + i g_2 \sigma_2 m(\mathbf{q}) \right] \\ &\quad + \frac{\hbar}{2D(\mathbf{q})} \left[g_2 G_{\rm s}(\mathbf{q}) \dot{m}(\mathbf{q}) + (g_1^2 + g_1 G_{\rm s}(\mathbf{q}) + g_2^2) i \sigma_2 \dot{m}(\mathbf{q}) \right]. \end{aligned} \tag{4.21}$$

where σ_2 is the second Pauli matrix. Note that the first term on the right hand side is the response to a uniform rotation of the magnetization, while the second and third terms give the response to a non-uniform and time-dependent magnetization.

The potentials are substituted into Eq. (4.12) to find the current-induced torque, and then into the Landau-Lifshitz-Gilbert equation (4.11) to find the rate of change of the magnetization. The current-induced torque has contributions proportional to the time derivative $\dot{\mathbf{m}}$, which lead to a renormalization of the Gilbert damping parameter α and the the gyromagnetic ratio γ. The renormalized Gilbert damping parameter $\tilde{\alpha}$ and gyromagnetic ratio $\tilde{\gamma} = \gamma/\tilde{\beta}$ depend on the transverse wavevector $\mathbf{q}$ and read

$$\begin{aligned} \tilde{\alpha} &= \alpha + \frac{\hbar^2 \gamma (g_1 + G_{\rm s}(\mathbf{q}))}{2Mde^2} \left[1 - \frac{G_{\rm s}(\mathbf{q})^2}{D(\mathbf{q})} \right], \\ \tilde{\beta} &= 1 + \frac{\hbar^2 \gamma g_2}{2Mde^2} \left[1 + \frac{G_{\rm s}(\mathbf{q})^2}{D(\mathbf{q})} \right]. \end{aligned} \tag{4.22}$$

In the macrospin limit $q \to 0$, these modifications coincide with the renormalized

values originally reported in Ref. [27].

Again using two-component spinor notation, the complete Landau-Lifshitz-Gilbert equation then becomes

$$(\tilde{\beta} 1_2 + i\sigma_2 \tilde{\alpha}) \dot{m}(\mathbf{q}) = A(\mathbf{q}) m(\mathbf{q}), \tag{4.23}$$

with

$$\begin{aligned} A(\mathbf{q}) &= \tau_{\parallel}^{(1)} 1_2 - i\sigma_2 \left[\tau_{\perp}^{(1)} + \frac{\hbar\gamma j_{\mathrm{f}} (q^2 + q_{\mathrm{f}}^2)}{2 e q_{\mathrm{f}} M} \right] \\ &\quad + \sigma_3 \frac{\gamma (k_1 - k_2)}{2M} \end{aligned} \tag{4.24}$$

and

$$\begin{aligned} \tau_{\parallel}^{(1)}(\mathbf{q}) &= \frac{\hbar\gamma e j}{M d e^2} \frac{g_1^2 + g_2^2 + g_1 G_{\mathrm{s}}(\mathbf{q})}{g_{\mathrm{m}}(0) D(\mathbf{q})} [G_{\mathrm{s}}(\mathbf{q}) - G_{\mathrm{s}}(0)], \\ \tau_{\perp}^{(1)}(\mathbf{q}) &= \frac{\hbar\gamma e j}{M d e^2} \frac{g_2 G_{\mathrm{s}}(\mathbf{q})}{g_{\mathrm{m}}(0) D(\mathbf{q})} [G_{\mathrm{s}}(\mathbf{q}) - G_{\mathrm{s}}(0)]. \end{aligned} \tag{4.25}$$

In the absence of a current, any spatial modulation of the magnetization is damped. However, a sufficiently large positive current I can overcome the damping, and cause a spatial modulation of $\mathbf{m}$ to grow in time, rather than decay. (A positive current I corresponds to electron flow in the negative x direction.) The instability condition is easily obtained from Eq. (4.23)

$$\tau_{\parallel}^{(1)}(\mathbf{q}) \frac{\tilde{\beta}(\mathbf{q})}{\tilde{\alpha}(\mathbf{q})} > \frac{\hbar\gamma j_{\mathrm{f}} (q^2 + q_{\mathrm{f}}^2)}{2 e q_{\mathrm{f}} M} + \tau_{\perp}^{(1)}(\mathbf{q}). \tag{4.26}$$

We can analyze this result in different limits. For a ferromagnetic layer with sufficiently small transverse dimensions, $W_y, W_z \lesssim (l_{\mathrm{sf}}/q_{\mathrm{f}}^2)^{1/3}$ if $l_{\mathrm{sf}} q_{\mathrm{f}} \gg 1$, the instability happens at wavevector $\mathbf{q} = (\pi/W_y)\hat{y}$ or $\mathbf{q} = (\pi/W_z)\hat{z}$, whichever is smallest, and the critical current follows directly from Eq. (4.26). For wider layers, the critical current density j_{c} and critical wavevector $\mathbf{q}_{\mathrm{c}}$ are found as the current-density wavevector pair for which the onset of the instability condition happens at the lowest current density.

This condition can be simplified in the limit of a very thin ferromagnetic layer, $d \to 0$, neglecting terms proportional to g_2 (which is numerically smaller than g_1), and for wavenumbers $q \ll q_{\rm f}$. We then find that the critical current follows from minimizing the relation

$$j_{\rm c}(\mathbf{q}) = \frac{\hbar^2 \gamma g_{\rm m}(0) j_{\rm f}}{2M q_{\rm f} e^2} \frac{q^2 + q_{\rm f}^2}{1 - (1 + q^2 l_{\rm sf}^2)^{-1/2}}. \tag{4.27}$$

In the limit $l_{\rm sf} \gg 1/q_{\rm f}$, this gives [28]

$$q_{\rm c} = (q_{\rm f}^2/2l_{\rm sf})^{1/3}, \quad j_{\rm c} = \frac{\hbar^2 \gamma g_{\rm m}(0) q_{\rm f} j_{\rm f}}{2Me^2}. \tag{4.28}$$

(The result for $j_{\rm c}$ was reported incorrectly in Ref. [28]. Note that the condition $q_{\rm c} \ll q_{\rm f}$, which was used to derive Eq. (4.27) is consistent with Eq. (4.28) if $l_{\rm sf} \gg 1/q_{\rm f}$.) Note that $q_{\rm f}$ increases with an applied magnetic field, so that this limit becomes relevant even for the case of a normal metal with strong spin relaxation if the magnetic field is large enough. In the limit $l_{\rm sf} \ll 1/q_{\rm f}$ of strong spin relaxation and weak anisotropy, one has

$$q_{\rm c} = (4/3)^{1/4} (q_{\rm f}/l_{\rm sf})^{1/2}, \quad j_{\rm c} = \frac{\hbar^2 \gamma g_{\rm m}(0) j_{\rm f}}{M q_{\rm f} l_{\rm sf}^2 e^2}. \tag{4.29}$$

At the critical current density, the trajectory of the magnetization is a simple ellipse (circle in the case of large magnetic fields). The ellipse is described by the coordinate transformation $m_1 = r(\cos\theta\cos\phi + \eta \sin\theta \sin\phi)$, and $m_2 = r(\sin\theta\cos\phi - \eta\cos\theta\sin\phi)$. The solution of the magnetization dynamics at the critical current then gives $\phi = \omega_0 t$ and r constant, where $\omega_0^2 = \omega_+^2 - \omega_-^2$, $\eta = (\omega_+ - \omega_-)/\omega_0$ and

$$\omega_+^{-1} = \frac{2Mce^2 q_{\rm f} \cos(2\theta)}{\gamma(q_{\rm f}^2 + q_{\rm c}^2) j_{\rm f}} - \frac{2Mce^2 q_{\rm f} g_2 G_{\rm s}(\mathbf{q}) \sin(2\theta)}{\gamma j_{\rm f}(q_{\rm f}^2 + q_{\rm c}^2)(g_1^2 + g_2^2 + g_1 G_{\rm s}(\mathbf{q}))}, \tag{4.30}$$

$$\omega_-^{-1} = \frac{2Mc\hbar}{\gamma(k_1 - k_2)}. \tag{4.31}$$

and c, θ are obtained from $\tilde{\alpha} = c \sin 2\theta, \tilde{\beta} = c \cos 2\theta$. For the case of a large applied magnetic field, $k_1 = k_2 = k$, and neglecting g_2, we have $\eta = 1$ and

$$\omega_0 = \hbar \gamma j_{\rm f} (q_{\rm c}^2 + q_{\rm f}^2)/(2 e q_{\rm f} M). \tag{4.32}$$

Note that, although the applied current has a large effect on the stability of the ellipsoidal motion (precession is damped for $j < j_{\rm c}$ and unstable for $j > j_{\rm c}$), its effect on the precession frequency is small. To a good approximation, the precession frequency equals the ferromagnetic resonance frequency in the absence of a current.

Whereas the first-order calculation allows one to find the current density at which the spin-wave instability sets in and the angular form of the low-amplitude excitations, it does not provide information about the magnitude of the spin-wave oscillation for $j > j_{\rm c}$, or about the effect of the spinwave oscillation on the resistance of the ferromagnetic layer. This information can only be obtained from the analysis of the magnetization dynamics beyond first-order in the amplitude. Such a program proceeds along the same lines as the first-order calculation shown above: Calculation of the potentials for charge and spin in the presence of a non-uniform and time-dependent magnetization, followed by a calculation of the current-induced torque and the rate of change of the magnetization. We have carried out this program to third order in m_1 and m_2, and list some of our general results in the appendix. However, as this calculation involves higher-order contributions to the anisotropy torque $\boldsymbol{\tau}_{\rm an}$, for which the expansion constants are unknown, we find that this calculation has little predictive value. Instead, we focus on the limit in which all magnetic anisotropy arises from an applied magnetic field. In this limit, $\boldsymbol{\tau}_{\rm an}$ is known, cf. Eq. (4.15), and a theoretical analysis is useful.

An important simplification is that the higher-order analysis is necessary for the Fourier components $m_1(\mathbf{q}_{\rm c})$ and $m_2(\mathbf{q}_{\rm c})$ at the critical wavevector only. The

precise value of $\mathbf{q}_c$ is determined by the transverse boundary conditions, see discussion following Eq. (4.26). For the just-above-critical current densities considered here, we can exclude a current dependent shift in $\mathbf{q}_c$. Hence, we need to consider only a single Fourier component in our considerations below. Solving for the leading (second order) correction to the charge potential, we find an expression that depends on the magnetization amplitude, to second order in m_1 and m_2, and on the time derivatives. Only first-order time-derivatives appear, which can be eliminated using the Landau-Lifshitz-Gilbert equation (4.23). For the case of a large applied magnetic field, the magnetization precession is circular, and one has

$$m_1(\mathbf{q}_c)\dot{m}_2(\mathbf{q}_c) - m_2(\mathbf{q}_c)\dot{m}_1(\mathbf{q}_c) = \omega_0 r(\mathbf{q}_c)^2, \tag{4.33}$$

where we abbreviated

$$r(\mathbf{q}_c)^2 = m_1(\mathbf{q}_c)^2 + m_2(\mathbf{q}_c)^2. \tag{4.34}$$

The precession frequency ω_0 given by Eq. (4.30) above. We then find

$$\begin{aligned} a_c^{(2)}(0) = & \frac{2(G_s(0) - G_s(\mathbf{q}_c))r(\mathbf{q}_c)^2}{D(\mathbf{q}_c)g_m(0)^2} \\ & \times \left[\omega_0 g_m(0)\left(D(\mathbf{q}_c) - G_s(\mathbf{q}_c)(g_1 + G_s(\mathbf{q}_c))\right)\right. \\ & \left. - 2ej_c\left(D(\mathbf{q}_c) + (G_s(0) - G_s(\mathbf{q}_c))(g_1 + G_s(\mathbf{q}_c))\right)\right] \end{aligned} \tag{4.35}$$

Solving for the leading (third) order torque, we note that the third order torque depends not only on the magnetization amplitudes $m_1(\mathbf{q}_c)$ and $m_2(\mathbf{q}_c)$, but also on their time derivative $\dot{m}_1$ and $\dot{m}_2$. The time derivatives appear to first, second, and third order in the expansion. The dependence on $\dot{m}^{(3)}$ leads to the same modifications to the Gilbert damping and gyromagnetic ratio as for the first-order current-induced torque calculated above. The dependence on $\dot{m}^{(2)}$ is through the 3-component only, which can be written as

$$\dot{m}_3^{(2)} = -m_1\dot{m}_1^{(1)} - m_2\dot{m}_2^{(1)}. \tag{4.36}$$

The first-order time derivatives $\dot{m}^{(1)}$ can be expressed in terms of m_1 and m_2 using Eq. (4.33) [or, in the general case, using Eq. (4.23)]. For the anisotropy torque $\tau_{\rm an}$ we take the contribution from the magnetic field only. Hence,

$$\begin{aligned}\tau_{\rm ex}(\mathbf{q}_{\rm c})+\tau_{\rm an}(\mathbf{q}_{\rm c}) &= \frac{\hbar\gamma j_{\rm f}}{2eq_{\rm f}M}\left[q_{\rm c}^2+q_{\rm f}^2+\frac{q_{\rm c}^2}{2}r(\mathbf{q}_{\rm c})^2\right]\\ &\quad\times(-i\sigma_2)m(\mathbf{q}_{\rm c}).\end{aligned}\tag{4.37}$$

Thus proceeding, we find that the third-order equation for the rate of change of the magnetization direction reads

$$(\tilde{\beta}1_2+i\sigma_2\tilde{\alpha})\dot{m}(\mathbf{q})^{(3)}=A(\mathbf{q})^{(3)}m(\mathbf{q})^{(3)},\tag{4.38}$$

with

$$\begin{aligned}A(\mathbf{q}_{\rm c})^{(3)} &= -\frac{1}{2}r(\mathbf{q}_{\rm c})^2\left[2\tau_{\parallel}^{(3)}(0)1_2-2i\sigma_2\tau_{\perp}^{(3)}(0)+\tau_{\parallel}^{(3)}(2\mathbf{q}_{\rm c})1_2-i\sigma_2\tau_{\perp}^{(3)}(2\mathbf{q}_{\rm c})\right.\\ &\quad\left.+3\tilde{\alpha}\omega_0 1_2+\frac{\hbar\gamma j_{\rm f}q_{\rm c}^2}{2eq_{\rm f}M}i\sigma_2\right],\end{aligned}\tag{4.39}$$

and

$$\begin{aligned}\tau_{\parallel}^{(3)}(\mathbf{k}) &= \frac{\hbar\gamma g_1}{Mde^2(g_1+G_{\mathbf{q}})}\left\{\frac{[g_++2G_{\rm c}(\mathbf{k})][g_++2G_{\rm s}(\mathbf{q})]-g_-^2}{[g_++2G_{\rm c}(\mathbf{k})][g_++2G_{\rm s}(\mathbf{k})]-g_-^2}\right\}\\ &\quad\times\left\{\frac{ej}{g_{\rm m}(0)}[G_{\rm s}(\mathbf{k})-G_{\rm s}(0)]\right.\\ &\quad\left.+\left[g_1\hbar\omega_0-\frac{2ej(g_1+G_{\rm s}(0))}{g_{\rm m}(0)}\right]\frac{G_{\rm s}(\mathbf{k})-G_{\rm s}(\mathbf{q})}{g_1+G_{\rm s}(\mathbf{q})}\right\},\end{aligned}\tag{4.40a}$$

$$\begin{aligned}\tau_{\perp}^{(3)}(\mathbf{k}) &= \frac{\hbar\gamma g_2\,G_{\rm s}(\mathbf{q})[G_{\rm s}(\mathbf{k})-G_{\rm s}(\mathbf{q})]}{Mde^2[g_1+G_{\rm s}(\mathbf{q})]^3}\\ &\quad\times\left\{\frac{[g_++2G_{\rm c}(\mathbf{k})][g_++2G_{\rm s}(\mathbf{q})]-g_-^2}{[g_++2G_{\rm c}(\mathbf{k})][g_++2G_{\rm s}(\mathbf{k})]-g_-^2}\left[g_1\hbar\omega_0-\frac{ej(g_1+G_{\rm s}(0))}{g_{\rm m}(0)}\right]\right.\\ &\quad\left.+\frac{[(g_+-2g_1)(2G_{\rm c}(\mathbf{k})+g_+)-g_-^2][G_{\rm s}(\mathbf{q})-G_{\rm s}(0)]ej}{g_{\rm m}(0)[(g_++2G_{\rm c}(\mathbf{k}))(g_++2G_{\rm s}(\mathbf{k}))-g_-^2]}\right\}.\end{aligned}\tag{4.40b}$$

Solving the differential equation for m, one finds that the precession amplitude

for current density j slightly above the critical current density j_c reads

$$r(\mathbf{q}_c)^2 = \frac{\hbar\gamma j_f(j-j_c)}{eq_f M j_c} \times \frac{\tilde{\alpha}(q_c^2+q_f^2)}{\tilde{\beta}\left[2\tau_\parallel^{(3)}(0)+\tau_\parallel^{(3)}(2\mathbf{q}_c)-3\tau_\parallel^{(1)}(\mathbf{q}_c)\right]-\tilde{\alpha}\left[2\tau_\perp^{(3)}(0)+\tau_\perp^{(3)}(2\mathbf{q}_c)-\hbar\gamma j_f q_c^2/(2eq_f M)\right]} \tag{4.41}$$

The result takes a simpler form in the limit $g_2 \to 0$ (since g_2 is numerically smaller than g_1), $d \to 0$, and $1/l_{sf} \ll q_c \ll q_f$,

$$r(\mathbf{q}_c)^2 = \frac{(j-j_c)(g_+^2-g_-^2+g_+\sigma/l_{sf})}{j_c(2g_1g_+ + g_+\sigma/l_{sf}-g_+^2+g_-^2)}. \tag{4.42}$$

Since $g_1 > g_+ > g_-$ we conclude that the $r(\mathbf{q}_c)^2 > 0$ is positive if $j > j_c$, which excludes hysteretic behavior.

In the same limit we can also calculate the change in frequency of the spinwave given by

$$\frac{\omega}{\omega_0} = 1 + \frac{q_c^2 r(\mathbf{q}_c)^2}{3(q_c^2+q_f^2)}. \tag{4.43}$$

Since the prefactor of the second term is much smaller than unity, $q_c \ll q_f$ for the parameter regime of interest, we conclude that in the regime of perturbation theory, there is hardly any change from the ferromagnetic resonance frequency.

Finally, at the onset of the spin-wave instability, the resistance of the ferromagnetic layer acquires a small negative correction

$$\begin{aligned} \frac{R}{R_0} &= 1 + \frac{a_c^{(2)}(0)}{a_c^{(0)}(0)}, \\ &\approx 1 - \frac{2(\sigma/l_{sf}+3g_1)g_-^2 r(\mathbf{q}_c)^2}{(\sigma/l_{sf}+g_+)(g_+^2-g_-^2+g_+\sigma/l_{sf})}. \end{aligned} \tag{4.44}$$

(In the second line we took the limits $g_2 \to 0$, $d \to 0$, and used $1/l_{sf} \ll q_c \ll q_f$.) This resistance decrease is anticipated on physical grounds since the non-uniform mode allows for an increased transmission of minority elections that diffuse along the transverse direction — see Fig. 4.2 and the corresponding discussion in Sec. 4.1.

4.3 Numerical calculation

The calculations in the preceding section are valid for currents close to the onset of the instability. For currents much larger than the critical current, we need to go beyond perturbation theory to obtain the dynamics. Hereto we numerically solve for the magnetization dynamics and its effect on the resistance of the ferromagnetic layer.

In our numerical analysis, we assume $W_z \ll W_y$ and impose that the magnetization direction $\mathbf{m}(y,z)$ does not depend on z. The remaining two-dimensional problem is replaced by a finite number of one-dimensional problems by substituting the normal-metal spacer and the ferromagnetic layer by N normal metal channels, each attached to a magnet with magnetization direction $\mathbf{m}(n)$, $n = 1, \ldots, N$. In order to model a higher-dimensional structure, electrons are allowed to diffuse between the channels, whereas the N magnets interact via an exchange energy. A schematic drawing of this model is shown in Fig. 4.4.

In this discretized model, the potentials for charge and spin obey the equations

$$\begin{aligned}
\partial_x^2 \mu_{\rm c}(n,x) \;+\; & \left(\frac{N}{W_y}\right)^2 [\mu_{\rm c}(n+1,x) + \mu_{\rm c}(n-1,x) \\
& - 2\mu_{\rm c}(n,x)] = 0, \\
\partial_x^2 \boldsymbol{\mu}_{\rm s}(n,x) \;+\; & \left(\frac{N}{W_y}\right)^2 [\boldsymbol{\mu}_{\rm s}(n+1,x) + \boldsymbol{\mu}_{\rm s}(n-1,x) \\
& - 2\boldsymbol{\mu}_{\rm s}(n,x)] = \frac{\boldsymbol{\mu}_{\rm s}(n,x)}{l_{\rm sf}^2}.
\end{aligned} \tag{4.45}$$

Equations for the boundary channels, $n = 1$ and $n = N$, are obtained by setting $\mu_{\rm c,s}(0,x) = \mu_{\rm c,s}(1,x)$ and $\mu_{\rm c,s}(N+1,x) = \mu_{\rm c,x}(N,x)$. The general solution of Eq.

(4.45) is of the form

$$\begin{aligned}\mu_{\rm c}(n,x) &= 2\sum_{l=0}^{N-1} a_{\rm c}(l)\cos\left[l\pi(n+1/2)/N\right]e^{-q_{\rm c}(l)x} \\ &\quad + \frac{eIx}{\sigma W_y W_z}. \\ \boldsymbol{\mu}_{\rm s}(n,x) &= 2\sum_{l=0}^{N-1} \mathbf{a}_{\rm s}(l)\cos\left[l\pi(n+1/2)/N\right]e^{-q_{\rm s}(l)x}, \end{aligned} \tag{4.46}$$

with

$$\begin{aligned} q_{\rm c}(l)^2 &= 4(N/W_y)^2\sin^2\left(l\pi/2N\right), \\ q_{\rm s}(l)^2 &= l_{\rm sf}^{-2} + 4(N/W_y)^2\sin^2\left(l\pi/2N\right). \end{aligned} \tag{4.47}$$

The boundary conditions at $x = 0$ (normal-metal–ferromagnet interface) are given by Eq. (4.3).

The magnetization dynamics is given by the Landau-Lifshitz-Gilbert equation (4.11), with a discretized exchange torque $\boldsymbol{\tau}_{\rm ex}$,

$$\boldsymbol{\tau}_{\rm ex}(n) = \frac{J\gamma M N^2}{W_y^2}\left[\mathbf{m}(n+1)+\mathbf{m}(n-1)\right]\times\mathbf{m}(n), \tag{4.48}$$

For the anisotropy torque we consider two different cases: The limit of a large applied magnetic field,

$$\boldsymbol{\tau}_{\rm an} = \frac{k\gamma}{M}\hat{\mathbf{e}}_3\times\mathbf{m}(n), \tag{4.49}$$

as well as the case of no applied field, where we take a simple model for the torque arising from magnetocrystalline and shape anisotropy,

$$\boldsymbol{\tau}_{\rm an}(n) = -\frac{\gamma}{M}[k_1 m_1(n)\hat{\mathbf{e}}_1 + k_2 m_2(n)\hat{\mathbf{e}}_2]\times\mathbf{m}(n). \tag{4.50}$$

The Landau-Lifshitz-Gilbert equation, together with the boundary conditions at $x = 0$, are sufficient to determine the $4N$ expansion coefficients $a_{\rm c}(l)$ and $\mathbf{a}_{\rm s}(l)$, $l = 0,\ldots,N-1$, and the time derivative of the magnetization directions $\mathbf{m}(n)$,

$n = 1, \ldots, N$. Our numerical procedure consists of first expressing $\dot{\mathbf{m}}(n)$ in terms of the potential expansion coefficients $a_{\rm c}(l)$ and $\mathbf{a}_{\rm s}(l)$ using the Landau-Lifshitz-Gilbert equation, and then solving for the potential expansion coefficients using the boundary condition at $x = 0$.

For the practical implementation of this scheme, it is useful to define 3×3 matrices $\mathcal{M}$ and $\mathcal{R} = \mathbf{m}\mathbf{m}^T$ such that for any vector $\mathbf{v}$, $\mathbf{v} \times \mathbf{m} = \mathcal{M}\mathbf{v}$ and $\mathcal{R} - 1_3 = \mathcal{M}^2$. In 3×3 matrix notation, the time derivative of the magnetization vector can be expressed in terms of the potential coefficients as

$$\begin{aligned} \dot{\mathbf{m}}(n) &= \frac{\beta' 1_3 + \alpha'^2 \mathcal{R}/\beta' - \alpha' \mathcal{M}}{\alpha'^2 + \beta'^2} \\ &\times \left\{ \mathcal{M}[\boldsymbol{\tau}_{\rm ex} + \boldsymbol{\tau}_{\rm an}] + \frac{2\hbar\gamma}{Mde^2} \sum_{l=0}^{N-1} [\mathcal{M} g_1 + g_2 1_3] \mathcal{M} \mathbf{a}_{\rm s}(l) \cos\left[l\pi(n+1/2)/N\right] \right\}, \end{aligned} \tag{4.51}$$

where $\alpha' = \alpha + \hbar^2 \gamma g_1/(Mde^2)$ and $\beta' = 1 + \hbar^2 \gamma g_2/(Mde^2)$. In turn, the potential coefficients $\mathbf{a}_{\rm s}(l)$ are obtained from inverting a $4N$ dimensional matrix equation,

$$\begin{aligned} \sum_{l=0}^{N-1} 2\cos\left(l\pi(n+1/2)/N\right) \begin{bmatrix} 2\sigma q_{\rm c}(l) + 2g_+ & 2\mathbf{m}^{\rm T} g_- \\ 2\mathbf{m} g_- & \sigma q_{\rm s}(l) 1_3 + 4\chi_1 \end{bmatrix} \begin{pmatrix} a_{\rm c}(l) \\ \mathbf{a}_{\rm s}(l) \end{pmatrix} \\ = \frac{2eI}{W_y W_z} \begin{pmatrix} g_+ \\ g_- \mathbf{m} \end{pmatrix} + \begin{pmatrix} 0 \\ \boldsymbol{\chi}_2 \end{pmatrix}, \end{aligned} \tag{4.52}$$

where we abbreviated

$$\begin{aligned} \chi_1(n) &= g_- \mathcal{R} - \mathcal{M}(g_1 \mathcal{M} + g_2 1_3) \\ &\quad + \frac{\hbar^2 \gamma}{2Mde^2(\alpha'^2 + \beta'^2)} (g_1 \mathcal{M} + g_2 1_3)[\beta' 1_3 \\ &\qquad + \alpha'^2 \mathcal{R}/\beta' - \alpha' \mathcal{M}] \mathcal{M}(g_1 \mathcal{M} + g_2 1_3), \end{aligned} \tag{4.53}$$

$$\begin{aligned} \boldsymbol{\chi}_2(n) &= \frac{2(g_1 \mathcal{M} + g_2 1_3)\hbar^2 \gamma}{Mde^2(\alpha'^2 + \beta'^2)} [\beta' 1_3 \\ &\qquad + \alpha'^2 \mathcal{R}/\beta' - \alpha' \mathcal{M}] \mathcal{M}[\boldsymbol{\tau}_{\rm ex}(n) + \boldsymbol{\tau}_{\rm an}(n)]. \end{aligned} \tag{4.54}$$

We have performed numerical simulations for N ranging between 10 and 20, although all data shown are for $N = 10$ and $N = 11$. We verified that there is no qualitative dependence on the parity of N in our simulations. A small random torque was added at each time step to mimic the effect of a small but finite temperature. (The corresponding temperature obtained from the fluctuation-dissipation theorem was less then a mK [19].)

Below we present our results. We first consider the case in which the anisotropy torque is dominated by an applied magnetic field, taking Eq. (4.49) for the anisotropy torque $\boldsymbol{\tau}_{\rm an}$. We then consider the case in which there is no applied magnetic field, taking Eq. (4.50) for $\boldsymbol{\tau}_{\rm an}$. The latter case is qualitatively different from the former, as it has two stable equilibria for $\mathbf{m}$ ($\mathbf{m} = \hat{\mathbf{e}}_3$ and $\mathbf{m} = -\hat{\mathbf{e}}_3$), whereas in the presence of a large applied field the equilibrium position is at $\mathbf{m} = \hat{\mathbf{e}}_3$.

4.3.1 Large applied magnetic field

For the numerical simulations with a magnetic field, we took values for the various parameters as follows: thickness $d = 0.2$ nm, Width $W_y = 55$ nm, as is appropriate for typical nanopillar experiments [7], spin-diffusion length $l_{\rm sf} = 100$ nm, $\sigma/l_{\rm sf} = 10^{15}\Omega^{-1}\mathrm{m}^{-2}$, $g_1 = 5.5 \times 10^{14}\ \Omega^{-1}\mathrm{m}^{-2}$, $g_2 = 0.3 \times 10^{14}\ \Omega^{-1}\mathrm{m}^{-2}$, $g_\uparrow = g_+ + g_- = 4.2 \times 10^{14}\ \Omega^{-1}\mathrm{m}^{-2}$, $g_\downarrow = g_+ - g_- = 3.3 \times 10^{14}\ \Omega^{-1}\mathrm{m}^{-2}$. The interface conductivities are taken from numerical calculations for a disordered Cu/Co interface [14]; the conductivity σ and the spin relaxation length $l_{\rm sf}$ are consistent with those in Cu. We further took $\alpha = 0.01$, $\hbar\gamma g_1/Mde^2 = 0.0138$, $j_{\rm f} = 10^{12}\mathrm{A/m}^2$, $q_{\rm f} = 10^{-1}\mathrm{nm}^{-1}$ (as is appropriate for Co, see Ref. [41]; the magnetic field corresponding to the values of $j_{\rm f}$ and $q_{\rm f}$ listed above is of a strength comparable to the intrinsic anisotropy energy). For these parameters, the width of the sample is so

small that the spinwave wavenumber q is set by the finite sample width, $q = \pi/W_y$.

For current densities below j_c, no spinwaves are excited. Simulation runs in which the magnetization is tilted away from the easy axis $\hat{\mathbf{e}}_3$ show damped precession towards the equilibrium magnetization direction $\mathbf{m} = \hat{\mathbf{e}}_3$. For current densities above j_c, a spin-wave with wavenumber $q = \pi/W_y$ is excited. Each magnet n in our simulation $n = 1, \ldots, N$ shows circular precession around the direction of the applied magnetic field, see Fig. 4.5, inset. The amplitude of the oscillation increases with current as predicted by the perturbation theory of the preceding section. The 3-component of the magnetization is a constant of the motion and can be monitored to measure the amplitude. Numerical results for m_3 for the magnet $n = 1$ are shown in Fig. 4.5 as a function of current density, together with a comparison of our numerical results with the perturbative result (4.42). With a large applied field, the magnetization dynamics remains regular even for current densities much larger than j_c. The effect of the spin-wave instability on the resistance of the ferromagnetic layer is shown in Fig. 4.6.

4.3.2 No applied magnetic field

We have also performed numerical simulations in the absence of an applied magnetic field. Hereto, we choose Eq. (4.50) for the anisotropy torque, and choose k_1 and k_2 such that $(k_1 - k_2)/(k_1 + k_2) = 0.99$. This form of the anisotropy is appropriate for thin magnetic layers, in which the magnetic anisotropy is predominantly of easy-plane type. The magnitude of the anisotropy energy is set by the parameters q_f and j_f, for which we take the same values as in the previous subsection. All other parameters are also taken the same as in the previous subsection.

The magnetization dynamics without applied magnetic field is much richer than

the magnetization dynamics at a large magnetic field. The reason is the existence of two stable equilibrium directions if no external magnetic field is applied ($\mathbf{m} = \hat{\mathbf{e}}_3$ and $-\hat{\mathbf{e}}_3$). At sufficiently large current densities, the current-induced torque drives the magnetization direction between these two stable directions, leading to a variety of dynamical phases.

For the numerical parameters chosen in our simulation, we observe the following characteristic dynamical modes: For current densities $j_c < j \lesssim 2j_c$ the instability develops with the wavenumber $q = \pi/W_y$. Because the magnetic anisotropy energy used for the simulation has no rotation symmetry around the 3 axis, the magnetization direction $\mathbf{m}(n)$ of each magnet $n = 1, \ldots, N$ traces out an ellipse, rather than a circle. We describe the magnetization motion is described using Poincaré sections for the polar angles θ and ϕ for the magnetization. The top right panel in Fig. 4.7 shows traces that are symmetric about $\phi = \pi$, which have the functional form for $\mathbf{m}$ as predicted by the perturbation theory in the preceding section.

For higher currents with $2j_c \lesssim j \lesssim 2.5j_c$, the reflection symmetry about the easy axis is spontaneously broken, resulting in asymmetric ellipses (upper inset in Fig. 4.8), which for even higher current densities turn into orbits around the direction perpendicular to the easy axis (lower inset in Fig. 4.8). A three-dimensional rendering of this regime is shown in Figure 4.8.

For even larger currents there is a transition into non-periodic modes that cover a significant part of phase space, as shown in Figure 4.9. Whereas these modes are non-ergodic for lower current densities, they eventually become ergodic and chaotic at high current densities, with Lyapunov exponents increasing with the current density j (data not shown).

In this general case, when the magnetization motion is not just simple circular

precession, the spin-wave instability not only leads to a decrease of the dc resistance of the ferromagnetic layer, it also causes a fast oscillation of the resistance as shown in the time trace in Figure 4.10. The right panel in Fig. 4.10 shows the decrease of the dc resistance up to $j = 2.5j_c$. (No sufficiently accurate numerical results were obtained for larger current density.) Results for the variation of the resistance amplitude and frequency with the applied current density are shown in the left panel for current densities up to $4j_c$. At the parameter values considered in our simulation, the onset of the non-periodic magnetization variations is accompanied by a sharp rise in precession frequency and a decrease of the amplitude of the resistance fluctuations.

4.4 Discussion and conclusion

We have presented a detailed study of the transverse spin-wave instability for a single ferromagnetic layer subject to a large current perpendicular to the layer. Our calculations have been in the small-amplitude regime, where perturbation theory can be used, and in the large-amplitude regime, where the magnetization dynamics can be solved numerically.

The two main signatures of the spin-wave instability are (1) existence of the instability for one current direction only, and (2) a small reduction in the dc resistance of the ferromagnetic layer. The resistance decrease arises because the existence of a spin wave with large amplitude lowers the spin accumulation in the normal metal adjacent to the ferromagnet. A lower spin accumulation corresponds to a lower resistance (just as a high spin accumulation state of the antiparallel configuration in the standard current-perpendicular-to-plane giant magnetoresistance

geometry gives a high resistance state). Both features have been seen in a recent experiment [29].

An important question for a dynamical instability is whether or not it is hysteretic. Our calculation has shown that the instability studied here is not, if a large magnetic field is applied. Without applied magnetic field, the nature of the spin wave instability depends on the precise form of the magnetic anisotropy, and both hysteretic and non-hysteretic behavior can be expected, in principle.

A noteworthy aspect of our calculation is that the spin-transfer torque is calculated self-consistently: the magnitude and direction of the spin-transfer torque depends on the spin accumulation in the normal metal, which, in turn, depends on the precise magnetization profile of the ferromagnet. In doing this, our work connects the the circuit theory for hybrid ferromagnet–normal-metal systems, which has been used extensively to describe the magnet's effect on spin accumulations in macrospin approximation [15], and micromagnetic simulations, which, to date, have been restricted to simplified models for the spin-transfer torque. However, our simulations should be considered a proof-of-principle. They lack the spatial resolution and sophistication that full-scale micromagnetic simulations have.

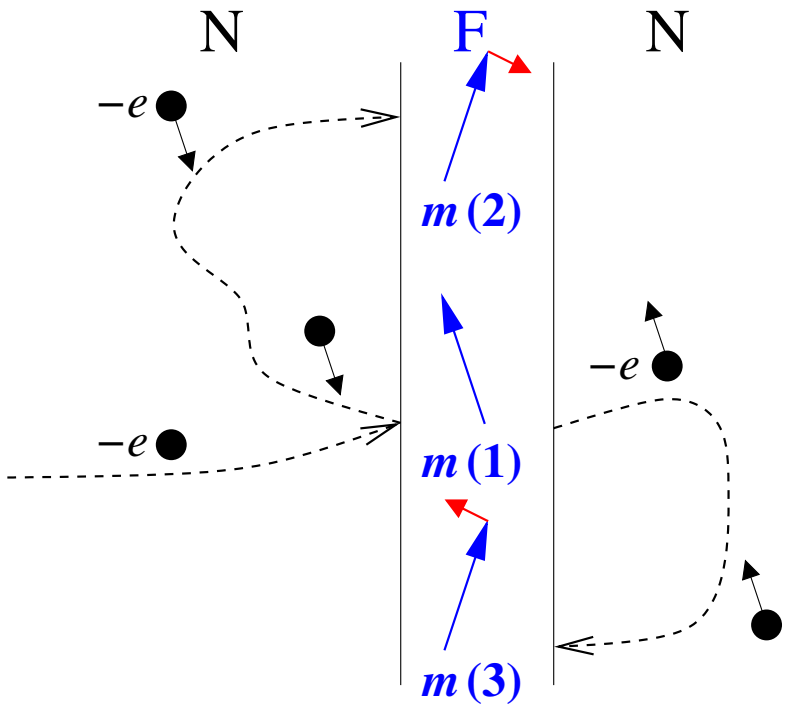

Figure 4.1: Through the spin-transfer torque, an unpolarized electrical current flowing perpendicular to a thin ferromagnetic layer can enhance or suppress spin waves. Electrons *backscattered* from the ferromagnet at point 1 have their spin predominantly polarized antiparallel to magnetization direction $\mathbf{m}(1)$. These electrons exert a torque on the ferromagnet's magnetization $\mathbf{m}(2)$ if they reach the ferromagnet a second time at point 2, the direction of the torque being to enhance an existing spinwave [*i.e.*, to increase any pre-existing difference between $\mathbf{m}(1)$ and $\mathbf{m}(2)$]. When electrons *transmitted* through the ferromagnet reach the ferromagnet a second time at point 3, they exert a torque that suppresses an existing spinwave. If source and drain contacts are not symmetric, there is a net torque on the ferromagnet, which enhances or suppresses the spin wave, depending on current direction.

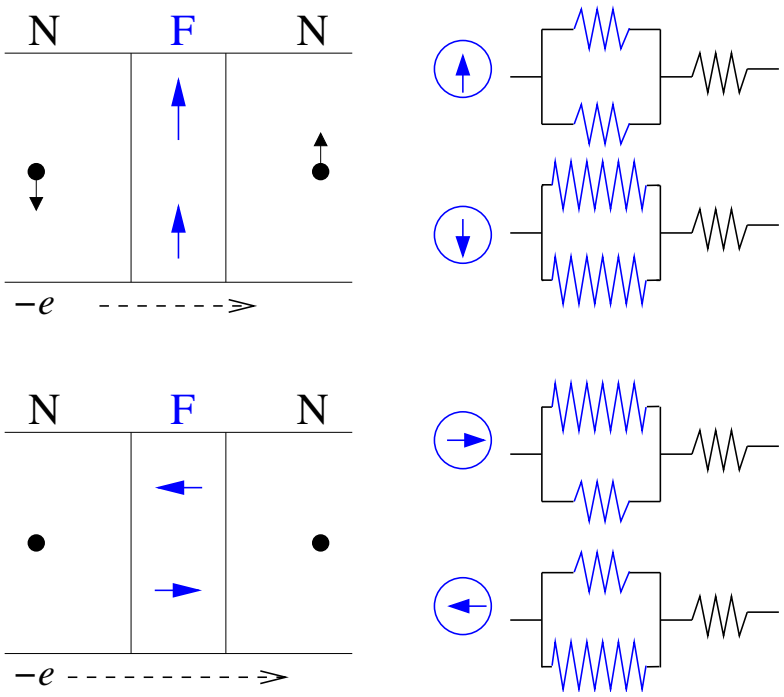

Figure 4.2: Spin will accumulate in normal metals on both sides of a ferromagnetic layer with uniform magnetization if an unpolarized current is passed through the ferromagnet (top left). A large-amplitude spinwave in the ferromagnet reduces the amount of spin polarization in the normal-metal regions adjacent to the ferromagnet and lowers the total resistance of the device (bottom left). This is shown schematically in the circuit diagrams (right). The top two circuit diagrams show the resistances seen by majority and minority electrons when the magnetization is spatially uniform, the short and long resistor symbols referring to minority and majority resistances, respectively. The ferromagnet with a large-amplitude spin wave can be seen as a parallel configuration of ferromagnets with opposite magnetization directions. The bottom two circuit diagrams show the resistances seen by two spin directions in this case. The net resistance is lower in the presence of a large-amplitude spin wave.

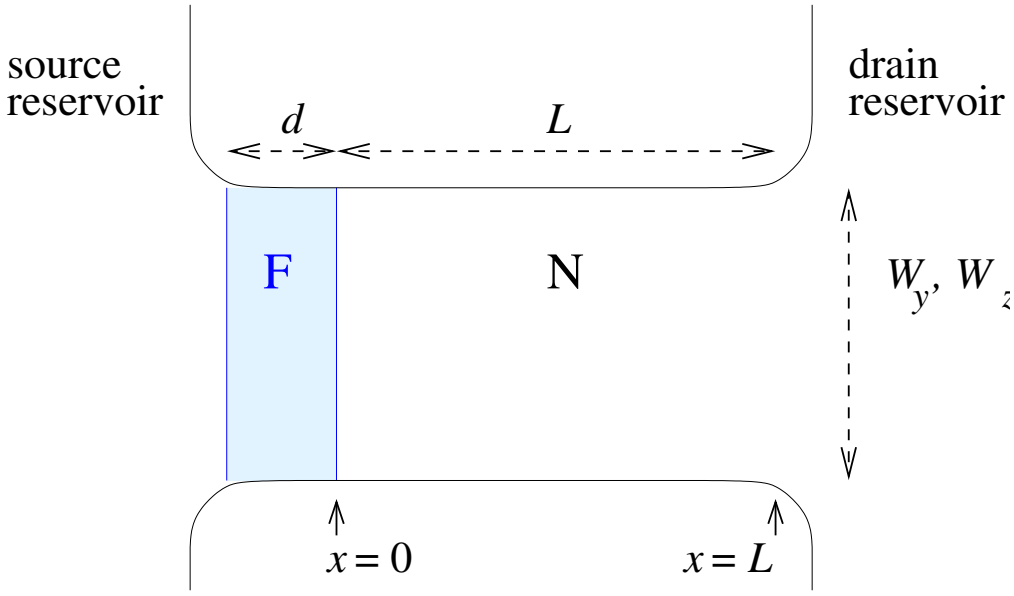

Figure 4.3: Schematic picture of the normal-metal–ferromagnet–normal-metal junction considered in our calculations. The ferromagnetic layer (F) is connected to source and drain reservoirs though normal metal spacers (N). We consider the maximally asymmetric case with only one spacer of length $L \gg l_{\rm sf}$.

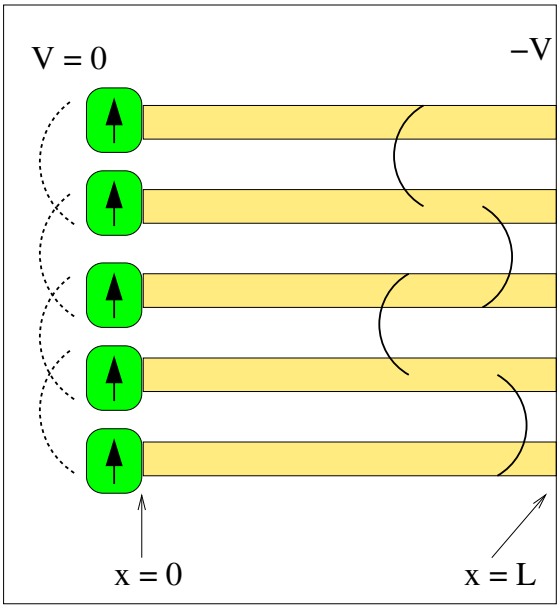

Figure 4.4: Schematic drawing of the model solved numerically. The continuous magnet is replaced by N magnets (left), each coupled to a normal-metal wire (right). The wires are coupled via transverse diffusion (shown schematically as solid lines); the magnets are coupled via the exchange interaction (shown schematically as dashed lines).

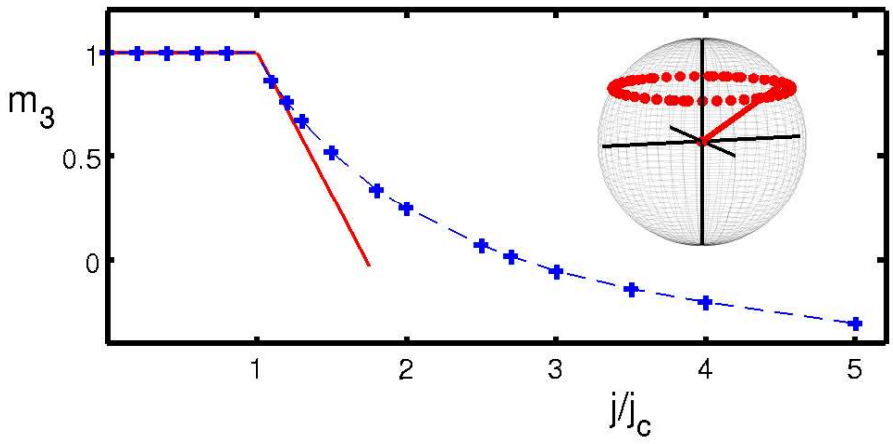

Figure 4.5: Main panel shows the magnetization component $m_3(1)$ of the first magnet, as a function of applied current. The solid line is obtained from the perturbation theory result (4.42), while the dashed line is a guide to the eye. In a large magnetic field, the motion is circular. an example is shown in the inset where $j = 1.5j_c$.

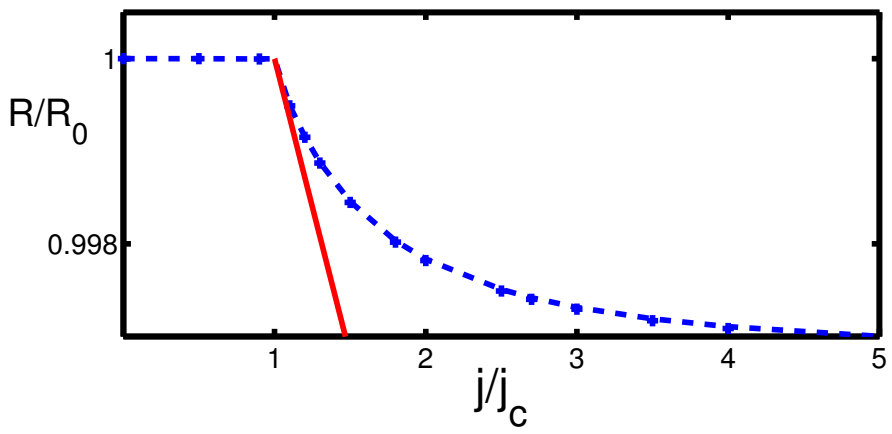

Figure 4.6: Resistance of the ferromagnetic layer, as a function of applied current (crosses). The solid line is obtained from the perturbation theory result (4.44), while the dashed line is a guide to the eye.

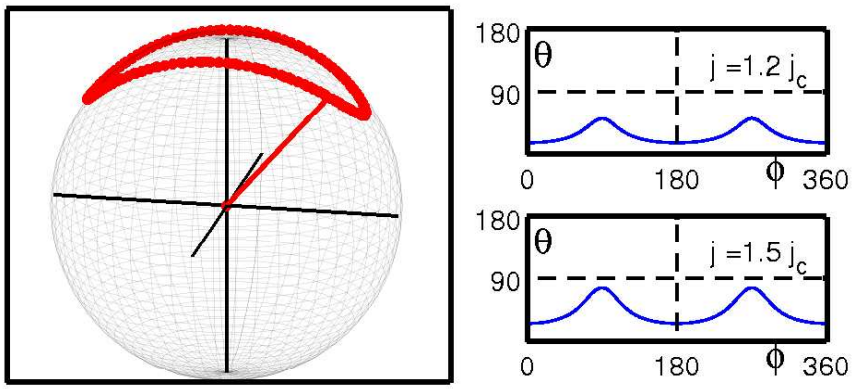

Figure 4.7: Typical elliptical trajectory for one of the discrete nanomagnets $\mathbf{m}(n)$ for weak easy axis and strong easy plane anisotropy with $j_c < j < 2j_c$ (left panel). The upper and lower right panels show the corresponding Poincaré sections for $j = 1.2j_c$ and $1.5j_c$ respectively. This regime agrees with the perturbative calculation of Sec. 4.2, where the lowest energy spin-wave mode is excited and increasing the current only changes the amplitude of elliptical oscillation.

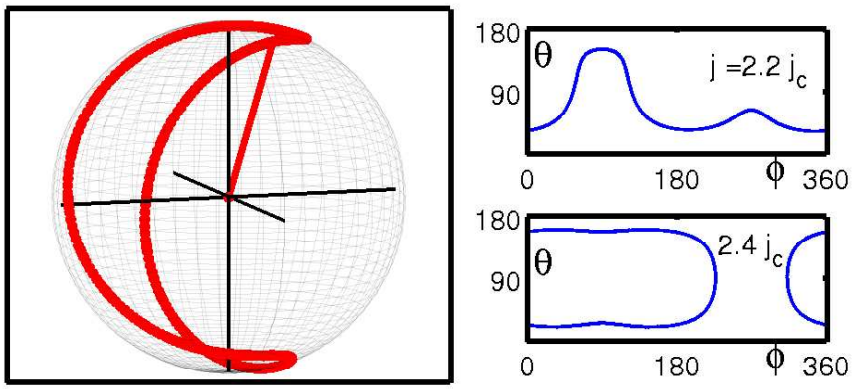

Figure 4.8: First manifestations of further dynamical instabilities in the range $2j_c < j < 2.5j_c$. The upper right panel shows a Poincaré section for $j = 2.2j_c$ where the motion is no longer symmetric about the easy axis. The lower right panel shows the motion for $j = 2.4j_c$ where the motion is trapped between the $\pm\hat{e}_3$ easy axes direction. The left panel shows what this motion looks like on the unit sphere.

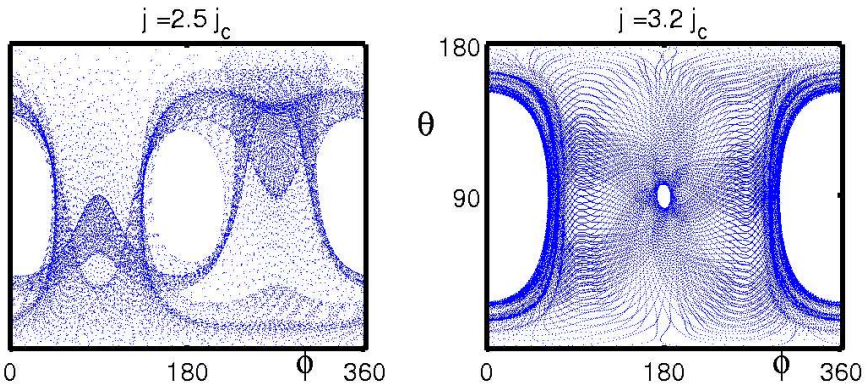

Figure 4.9: Poincaré sections for the magnetization direction of one of the magnets at $j = 2.5j_c$ (left) and $j = 3.2j_c$ (right).

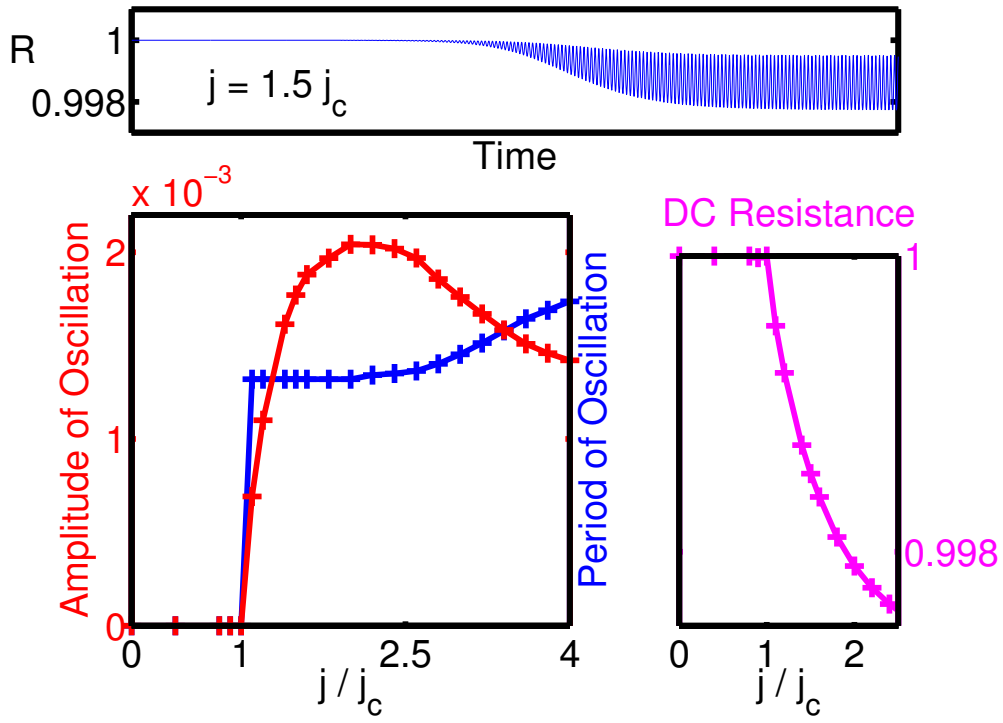

Figure 4.10: The upper panel shows the time trace of resistance where the spin-wave instability causes a decrease in the observed resistance. The lower left plot shows how the amplitude and period of the resistance oscillation change with the driving current, while the lower right panel shows the decrease of dc resistance.

BIBLIOGRAPHY

[1] J. C. Slonczewski, J. Magn. Magn. Mater. **159**, 1 (1996).

[2] L. Berger, Phys. Rev. B **54**, 9353 (1996).

[3] M. Tsoi, A. G. M. Jansen, J. Bass, W.-C. Chiang, M. Seck, V. Tsoi, and P. Wyder, Phys. Rev. Lett. **80**, 4281 (1998).

[4] J. Z. Sun, J. Magn. Magn. Mater. **202**, 157 (1999).

[5] J.-E. Wegrowe, D. Kelly, Y. Jaccard, P. Guittienne, and J.-P. Ansermet, Europhys. Lett. **45**, 626 (1999).

[6] E. Myers, D. Ralph, J. Katine, R. Louie, and R. Buhrman, Science **285**, 867 (1999).

[7] J. A. Katine, F. J. Albert, R. A. Buhrman, E. B. Myers, and D. C. Ralph, Phys. Rev. Lett. **84**, 3149 (2000).

[8] S. I. Kiselev, J. C. Sankey, I. N. Krivorotov, N. C. Emley, R. J. Schoelkopf, and R. A. Buhrman, Nature **425**, 380 (2003).

[9] S. I. Kiselev, J. C. Sankey, I. N. Krivorotov, N. C. Emley, M. Rinkoski, C. Perez, R. A. Buhrman, and D. C. Ralph, Phys. Rev. Lett. **93**, 036601 (2004).

[10] W. H. Rippard, M. R. Pufall, S. Kaka, S. E. Russek, and T. J. Silva, Phys. Rev. Lett. **92**, 027201 (2004).

[11] I. N. Krivorotov, N. C. Emley, A. G. F. Garcia, J. C. Sankey, S. I. Kiselev, D. C. Ralph, and R. A. Buhrman, Phys. Rev. Lett. **93**, 166603 (2004).

[12] X. Waintal, E. B. Myers, P. W. Brouwer, and D. C. Ralph, Phys. Rev. B **62**, 12317 (2000).

[13] M. D. Stiles and A. Zangwill, Phys. Rev. B **66**, 014407 (2002).

[14] K. Xia, P. J. Kelly, G. E. W. Bauer, A. Brataas, and I. Turek, Phys. Rev. B **65**, 220401(R) (2002).

[15] Y. Tserkovnyak, A. Brataas, G. E. W. Bauer, and B. I. Halperin, cond-mat/0409242 (2004).

[16] J. Z. Sun, Phys. Rev. B **62**, 570 (2000).

[17] Y. B. Bazaliy, B. A. Jones, and S.-C. Zhang, Phys. Rev. B **69**, 094421 (2004).

[18] Z. Li and S. Zhang, Phys. Rev. B **69**, 134416 (2004).

[19] D. Apalkov and P. Visscher, cond-mat/0405305 (2004).

[20] A. Kovalev, G. Bauer, and A. Brataas, cond-mat/0504705 (2005).

[21] J. Xiao, A. Zangwill, and M. D. Stiles, cond-mat/0504142 (2005).

[22] Z. Li and S. Zhang, Phys. Rev. B **68**, 024404 (2003).

[23] D. Berkov and N. Gorn, Phys. Rev. B **71**, 052403 (2005).

[24] D. Berkov and N. Gorn, cond-mat/0503754 (2005).

[25] L. Torres, L. Lopez-Diaz, E. Martinez, M. Carpentieri, and G. Finocchio, J. Magn. Mag. Mater. **286**, 381 (2005).

[26] A. Brataas, Y. V. Nazarov, and G. E. W. Bauer, Phys. Rev. Lett. **84**, 2481 (2000).

[27] Y. Tserkovnyak, A. Brataas, and G. E. W. Bauer, Phys. Rev. Lett. **88**, 117601 (2002).

[28] M. L. Polianski and P. W. Brouwer, Phys. Rev. Lett. **92**, 026602 (2004).

[29] B. Özyilmaz, A. D. Kent, J. Z. Sun, M. J. Rooks, R. H. Koch, Phys. Rev Lett. **93**, 176604 (2004).

[30] Y. Ji, C. L. Chien, and M. D. Stiles, Phys. Rev. Lett. **90**, 106601 (2003).

[31] M. D. Stiles, J. Xiao, and A. Zangwill, Phys. Rev. B. **69**, 054408 (2004).

[32] S. Urazhdin, Phys. Rev. B. **69**, 134430 (2004).

[33] A. Brataas, Y. Tserkovnyak, and G. Bauer, cond-mat/0501672 (2005).

[34] A. Slavin and P. Kabos, IEEE Trans. Mag. **41**, 1264 (2005).

[35] B. Özyilmaz, A. D. Kent, M. J. Rooks, and J. Z. Sun, Phys. Rev. B **71**, 140403 (2005).

[36] T. Y. Chen, Y. Ji, C. L. Chien, and M. D. Stiles, Phys. Rev. Lett. **93**, 026601 (2004).

[37] M. D. Stiles, J. Appl. Phys. **79**, 5805 (1996).

[38] E. M. Lifschitz and L. P. Pitaevskii, *Statistical Physics, part 2* (Pergamon, Oxford, 1980).

[39] T. L. Gilbert, IEEE Trans. Mag. **40**, 3443 (2004).

[40] Ya. B. Bazaliy, B. A. Jones, and S.-C. Zhang, Phys. Rev. B **57**, R3213 (1998).

[41] E. P. Wohlfahrt, in *Ferromagnetic Materials*, edited by E. P. Wohlfahrt (North-Holland, Amsterdam, 1980), Vol. 1.

Chapter 5

Mesoscopic anisotropic magnetoconductance fluctuations in ferromagnets

5.1 Introduction

One hallmark of phase-coherent transport is the phenomenon of "universal conductance fluctuations", random, but reproducible variations in a sample's conductance as a function of the applied magnetic field or the Fermi energy [1, 2, 3, 4, 5]. The magnitude of the conductance fluctuations is of order unity, in units of the conductance quantum e^2/h, and does not depend on specific sample properties, such as the impurity concentration, the meterial, shape, or method of preparation.

Recently there has been both theoretical and experimental interest in mesoscopic transport in itinerant ferromagnets. The experimental interest stems from the ability to fabricate ferromagnetic conductors small enough that transport

through the magnet is predominantly coherent [6, 7]. The theoretical interest is motivated by the rich variety of ways through which random impurity scattering can affect the properties of an itinerant ferromagnet. Theoretical predictions exist for the effect of domain walls on weak localization and conductance fluctuations [8, 9] as well as for the combined effect of spin-orbit interaction and impurity scattering on weak localization [10] and magnetic anisotropy [11]. Although disordered ferromagnetic conductors display different phenomena than their normal-metal counterparts, the theoretical framework to describe them is rather similar. Indeed, the methods of diagrammatic perturbation theory developed for electron transport in disordered metals can be applied to ferromagnets by modifying the single particle Hamiltonian taking into account the exchange field and/or spin-orbit interactions.

In this chapter, we address the mesoscopic contribution to a ferromagnet's anisotropic magnetoresistance. Anisotropic magnetoresistance is the phenomenon that a magnet's resistance depends on the orientation of the magnetization resulting from a combination of spin-orbit coupling and orbital magnetic effects [12]. For a single domain magnet, the resistance is a smooth function of the magnetization direction. The mesoscopic effect described here consists of an additional and faster random dependence on the magnetization direction that is different for each sample, but reproducible for a given sample. This situation is not very different from the case of standard universal conductance fluctuations in a normal metal, where the random magnetic-field dependent fluctuations are superimposed on a systematic magnetoconductance.

There are two possible mechanisms through which the magnetization direction can affect the interference correction to the conductance. First, a change of the

magnetization direction causes a change of the internal magnetic field, which directly affects the orbital motion of the electrons via a change of Aharonov-Bohm phases. Second, a change of the magnetization direction causes a change of the exchange field, which affects the motion of the electrons via spin-orbit scattering. The first effect would be dominant if the magnetic flux through the cross-section of a phase coherent volume is of the order of the flux quantum. For many magnetic materials, the phase coherent lengths can be small and this effect can be neglected (see discussion in Ref. [10]). In what follows, we assume that this condition holds, and that the second effect dominates the mesoscopic anisotropic magnetoresistance. For the same reason, we ignore any effect of an applied magnetic field used to change the magnetization direction.

5.2 Theoretical model

We consider an ensemble of ferromagnetic particles, each with a different configuration of impurities and calculate the conductance autocorrelation function

$$\mathcal{C}(\theta) = \langle G(\hat{\mathbf{m}})G(\hat{\mathbf{m}}')\rangle - \langle G(\hat{\mathbf{m}})\rangle^2, \tag{5.1}$$

where θ is the angle between the magnetization directions $\hat{\mathbf{m}}$ and $\hat{\mathbf{m}}'$ and the brackets $\langle \ldots \rangle$ denote the ensemble average. The vectors $\hat{\mathbf{m}}$ and $\hat{\mathbf{m}}'$ are defined to have unit length. The Hamiltonian for a ferromagnet with spin-orbit scattering is

$$\mathcal{H}_{\alpha\beta} = \left(\frac{p^2}{2m} - \mu\right)\delta_{\alpha\beta} - E_{\mathrm{Z}}\sigma^z_{\alpha\beta} + \mathcal{V}_{\alpha\beta} \tag{5.2}$$

where α and β are spin indices, σ_z the Pauli matrix, the magnetization direction $\hat{\mathbf{m}}$ is taken as the spin quantization axis, and $E_{\mathrm{Z}} = \mu_{\mathrm{B}}B_{\mathrm{ex}}$ is the Zeeman energy corresponding to the exchange field B_{ex}. We perform the ensemble average at a

fixed chemical potential μ and exchange field $B_{\rm ex}$, rather than at self-consistently determined μ and $B_{\rm ex}$. Although the omission of the self-consistency conditions is known to affect averaged quantities, it is believed not to affect fluctuations [13, 14, 15].

The random potential $\mathcal{V}$ in Eq. (5.2) describes the effect of elastic impurity scattering and spin-orbit scattering, respectively. Its Fourier transform is

$$\begin{aligned} \mathcal{V}_{\alpha\mathbf{k},\beta\mathbf{k}'} &= V_{\mathbf{k}-\mathbf{k}'} \\ &\quad - iV^{\rm so}_{\mathbf{k}-\mathbf{k}'}((\mathbf{k}'\times\mathbf{k})\cdot(\hat{\mathbf{m}}\sigma^z+\hat{\mathbf{e}}_1\sigma^x+\hat{\mathbf{e}}_2\sigma^y)_{\alpha\beta}, \end{aligned} \tag{5.3}$$

where $\hat{\mathbf{e}}_1$ and $\hat{\mathbf{e}}_2$ are unit vectors perpendicular to each other and to $\hat{\mathbf{m}}$ such that $\hat{\mathbf{e}}_1\times\hat{\mathbf{e}}_2=\hat{\mathbf{m}}$. The random potentials V and $V^{\rm so}$ are assumed to be uncorrelated and Gaussian white noise, with r.m.s. strength v and $v^{\rm so}$, respectively,

$$\langle V_{\mathbf{q}}V_{\mathbf{q}'}\rangle = v^2\delta(\mathbf{q}-\mathbf{q}'), \quad \langle V^{\rm so}_{\mathbf{q}}V^{\rm so}_{\mathbf{q}'}\rangle = v^2_{\rm so}\delta(\mathbf{q}-\mathbf{q}'). \tag{5.4}$$

In the leading order Born approximation, the scattering time τ_α for spin-independent impurity scattering of electrons with spin α is given by

$$\frac{1}{2\pi\nu_\uparrow\tau_\uparrow}=v^2, \quad \frac{1}{2\pi\nu_\downarrow\tau_\downarrow}=v^2, \tag{5.5}$$

where ν_α is the density of states of electrons with spin α. Similarly, for spin-conserving and spin-flip scattering off $V^{\rm so}$, one has the mean free times

$$\begin{aligned} \frac{1}{2\pi\nu_\uparrow\tau_{\uparrow\parallel}} &= \frac{2}{9}v^2_{\rm so}k^4_{\rm F\uparrow}, \quad \frac{1}{2\pi\nu_\downarrow\tau_{\downarrow\parallel}}=\frac{2}{9}v^2_{\rm so}k^4_{\rm F\downarrow}, \\ \frac{1}{2\pi\nu_\downarrow\tau_{\uparrow\perp}} &= \frac{1}{2\pi\nu_\uparrow\tau_{\downarrow\perp}}=\frac{2}{9}v^2_{\rm so}k^2_{\rm F\uparrow}k^2_{\rm F\downarrow}, \end{aligned} \tag{5.6}$$

respectively, where $k_{\rm F\alpha}$ is the Fermi wavevector for spin α electrons. In a realistic ferromagnet, the kinetic energy and the random potential will not have the simple form assumed in our calculation, which implies that the relationships between the

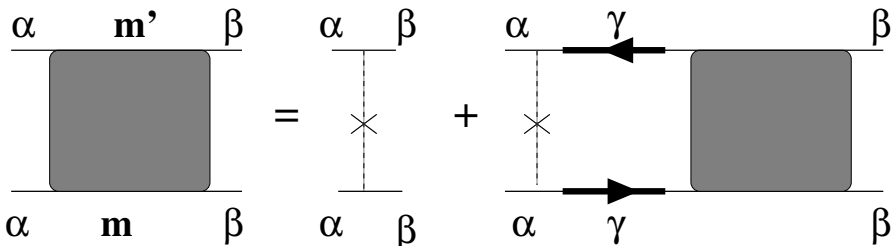

Figure 5.1: Dyson Equation for Diffuson ladder. The dotted line indicates a scattering event.

scattering times implied by Eqs. (5.5) and (5.6) need not hold. Although we use the simple model described above to set up our calculation and to define the scattering times, these are then considered independent for the rest of the calculation [except for the equality in the second line of Eq. (5.6), which follows from detailed balance].

Throughout the calculation, we assume that $\tau \ll \tau_{\|}$, $\tau_{\perp}$. This implies that all Green functions appearing in intermediate phases of the calculation can be averaged over all directions of the momentum. We also assume that phase coherence is preserved over the entire sample. In a sample with size L larger than the phase coherence length L_ϕ, our answer would be modified as $\mathcal{C}(\theta, L) \sim \mathcal{C}(\theta, L_\phi)(L_\phi/L)$. In this case, the angle over which the conductance typically fluctuates is then determined by L_ϕ instead of L.

5.3 Details of calculation

We now describe the details of our calculation. For the retarded Green function $\mathcal{G}^{\mathrm{R}}$, averaged over the random potential and over all directions of the momentum, we find

$$\langle \mathcal{G}^{\mathrm{R}}_{\alpha}(\omega, k, \hat{\mathbf{m}})\rangle^{-1} = \omega - \varepsilon_{\alpha}(k) + \frac{i}{2\tau_{\alpha}} + \frac{i}{2\tau_{\alpha\|}} + \frac{i}{\tau_{\alpha\perp}}, \tag{5.7}$$

where $\varepsilon_\alpha(k) = \hbar^2 k^2/2m - \mu - E_Z \sigma^z_{\alpha\alpha}$ is the energy of an electron with spin α and momentum $\hbar\mathbf{k}$. In order to calculate the conductance autocorrelation function (5.1), we need to consider the Diffuson and Cooperon propagators of diagrammatic perturbation theory. Again, in view of the inequality $\tau \ll \tau_\parallel$, $\tau_\perp$, we only need Diffuson and Cooperon propagators averaged over all momentum directions. Since the Cooperon and Diffuson propagators are related by time reversal,

$$C(\omega, \mathbf{q}, \theta) = D(\omega, \mathbf{q}, \pi - \theta), \tag{5.8}$$

it will be sufficient to calculate the Diffuson only.

The Diffuson propagator is defined by the ladder diagrams shown in Fig. 5.1. The solid arrows in Fig. 5.1 denote the impurity-averaged Green functions (5.7). The two legs of the ladder refer to the two magnetization directions $\hat{\mathbf{m}}$ and $\hat{\mathbf{m}}'$. For both magnetization directions we use the convention that the magnetization direction is the spin quantization axis. This is the natural choice for ferromagnets: Since $E_Z\tau \gg 1$ in a typical ferromagnet, with this convention only ladder diagrams for which the spin indices of retarded and advanced Green functions are pairwise equal at all times need to be considered; contributions with different spin index for retarded and advanced Green functions dephase within a mean free time and do not contribute to the Diffuson propagator. One should note, however, that this convention implies that the directions of "spin up" and "spin down" in the upper and lower legs of the ladder correspond to different physical directions if $\hat{\mathbf{m}} \neq \hat{\mathbf{m}}'$.

Summing the ladder diagrams of Fig. 5.1, we then find that the Diffuson obeys the 2×2 matrix equation

$$\sum_{\gamma=\uparrow,\downarrow} K_{\alpha\gamma} D(\omega, \mathbf{q}, \theta)_{\gamma\beta} = \delta_{\alpha\beta} \frac{1}{2\pi\nu_\alpha\tau_\alpha}. \tag{5.9}$$

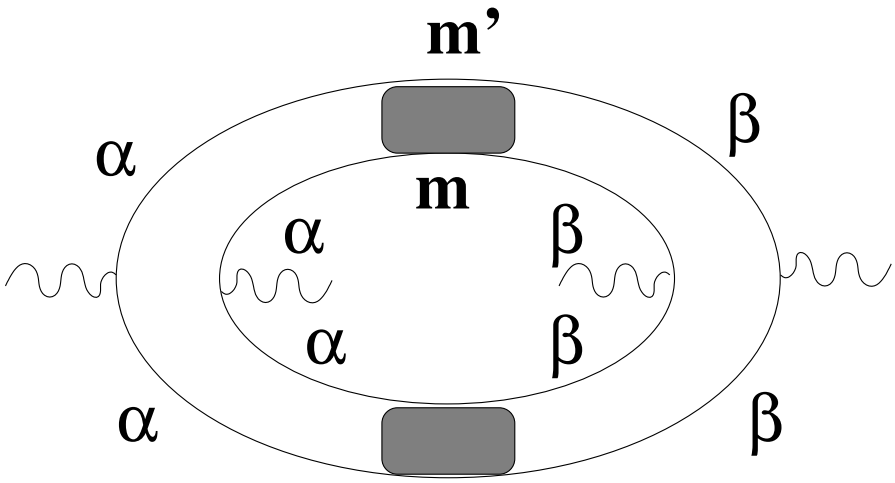

Figure 5.2: Leading diagrams for conductance correlator. The wavy lines represent the current vertex J and the shaded box represents either the Cooperon or Diffuson propagator.

Here K is a 2×2 matrix, with diagonal elements given by

$$\hat{K}_{\alpha\alpha} \;=\; \tau_\alpha \left[D_\alpha q^2 + i\omega + \frac{2}{\tau_{\alpha\perp}} + \frac{1-\cos\theta}{\tau_{\alpha\|}} \right], \tag{5.10}$$

where $D_\alpha = v_{\mathrm{F}\alpha}^2 \tau_\alpha / 3$ is the diffusion constant. The off-diagonal matrix elements contain a phase factor that depends on the precise choice of coordinate axes perpendicular to $\hat{\mathbf{m}}$ and $\hat{\mathbf{m}}'$, cf. Eq. (5.3). In all final expressions, the off-diagonal elements of K only enter through their product, which is independent of this choice,

$$K_{\uparrow\downarrow} K_{\downarrow\uparrow} = \frac{\tau_\uparrow \tau_\downarrow}{\tau_{\uparrow\perp}\tau_{\downarrow\perp}} (1+\cos\theta)^2. \tag{5.11}$$

Once the Diffuson is known, the Cooperon is calculated via Eq. (5.8). For the special case $\theta = 0$, the result for C was previously obtained by Dugaev *et al.*[10].

We can now proceed to calculate the conductance correlation function $\mathcal{C}(\theta)$. We are interested in the conductance correlations at zero temperature, which allows us to set $\omega = 0$ in our expressions for the Diffuson and Cooperon propagators. We

consider a coherent rectangular sample with sides L_x, L_y and L_z, with a current in the z direction. Following Refs. [5, 2], we then find that the conductance autocorrelation function is given by

$$\mathcal{C}(\theta) = \frac{3e^4}{2L_z^4 h^2} \sum_{\mathbf{q}} \mathrm{tr}\,[JD(\mathbf{q})JD(\mathbf{q}) + JC(\mathbf{q})JC(\mathbf{q})], \tag{5.12}$$

where the current vertex reads

$$J_{\alpha\beta} = \frac{4\pi}{3} v_{\mathrm{F}\alpha}^2 \tau_\alpha^3 \delta_{\alpha\beta} \tag{5.13}$$

and the vector $\mathbf{q}$ is summed over the values $q_x = \pi n_x/L_x$, $q_y = \pi n_y/L_y$, and $q_z = \pi n_z/L_z$ with n_x, $n_y = 0, 1, 2, \ldots$ and $n_z = 1, 2, \ldots$. Without the prefactor 3/2, Eq. (5.12) is precisely the contribution from the diagram shown in Fig. 5.2. The factor 3/2 in front of Eq. (5.12) accounts for other diagrams that contribute to the conductance fluctuations, whose net contribution is 1/2 times that of the diagram of Fig. 5.2 [2, 5]. Substituting our results for the Diffuson and Cooperon propagators, we find

$$\mathcal{C}(\theta) = \frac{6e^4}{\pi^4 h^2} \sum_{\mathbf{q}} \sum_{\pm} \left[\frac{1}{((L_z q/\pi)^2 + a_\pm(\theta))^2} + \frac{1}{((L_z q/\pi)^2 + a_\pm(\pi - \theta))^2} \right], \tag{5.14}$$

where

$$\begin{aligned} a_\pm(\theta) \;=\; & \frac{1}{\tau_{\uparrow\perp} E_\uparrow} + \frac{1}{\tau_{\downarrow\perp} E_\downarrow} + \frac{\tau_{\uparrow\parallel} E_\uparrow + \tau_{\downarrow\parallel} E_\downarrow}{2\tau_{\uparrow\parallel}\tau_{\downarrow\parallel} E_\uparrow E_\downarrow}(1 - \cos\theta)) \\ & \pm \sqrt{\frac{(1+\cos\theta)^2}{\tau_{\uparrow\perp}\tau_{\downarrow\perp} E_\uparrow E_\downarrow} + \left[\frac{1}{\tau_{\uparrow\perp} E_\uparrow} - \frac{1}{\tau_{\downarrow\perp} E_\downarrow} - \frac{\tau_{\uparrow\parallel} E_\uparrow - \tau_{\downarrow\parallel} E_\downarrow}{2\tau_{\uparrow\parallel}\tau_{\downarrow\parallel} E_\uparrow E_\downarrow}(1 - \cos\theta) \right]^2} \end{aligned} \tag{5.15}$$

and $E_\alpha = D_\alpha(\pi/L_z)^2$ is the Thouless energy for spin α. Note that the parameter that governs the importance of spin-orbit scattering is the product $\tau_{\alpha\perp} E_\alpha$ or $\tau_{\alpha\parallel} E_\alpha$, which is the ratio of the spin-orbit time and the Thouless time, which is the time to diffuse through the sample.

The expression for $a_\pm(\theta)$ simplifies in two limiting cases. If $\theta = 0$, one has $a_+ = 2/\tau_{\uparrow\perp}E_\uparrow + 2/\tau_{\downarrow\perp}E_\downarrow$ and $a_- = 0$, showing the presence of universal conductance fluctuations in a ferromagnet. The corresponding eigenvalues for the Cooperon contribution are found by setting $\theta = \pi$, $a_+(\pi) = 2/\tau_{\uparrow\perp}E_\uparrow + 2/\tau_{\uparrow\parallel}E_\uparrow$ and $a_-(\pi) = 2/\tau_{\downarrow\perp}E_\downarrow + 2/\tau_{\downarrow\parallel}E_\downarrow$. Another simple limit is that of a half-metal, a ferromagnet with vanishing density of states for the minority spins. For a half metal, the only relevant time and energy scales are the scattering time $\tau_{\uparrow\parallel}$ for spin-preserving spin-orbit scattering of majority electrons and the majority electron Thouless energy $E_\uparrow$. One then finds that only one root $a_\pm$ is relevant, $a(\theta) = (1 - \cos\theta)/\tau_{\uparrow\parallel}E_\uparrow$.

5.3.1 Analytical result for quasi one-dimension

The sum over wavevectors in Eq. 5.14 can be performed analytically for a quasi one-dimensional sample. Setting $n_x = n_y = 0$ in the summation, one finds

$$\mathcal{C}(\theta) \;=\; \sum_{\pm} \left[F(\pi\sqrt{a_\pm(\theta)}) + F(\pi\sqrt{a_\pm(\pi-\theta)}) \right], \tag{5.16}$$

where $F(x) = 3e^4(-2 + x\coth x + x^2\sinh^{-2}x)/2x^4h^2$. Note that for $\theta = 0$, Eq. (5.16) reproduces the known results $\operatorname{var} G = (e^2/h)^2(1/15)$ for strong spin-orbit scattering and $\operatorname{var} G = (e^2/h)^2(4/15)$ for weak spin orbit scattering.

5.3.2 Numerical results for higher dimensions

For quasi 2D and 3D samples $\mathcal{C}(\theta)$ can be computed numerically. The dependence on the spin-orbit scattering is qualitatively similar for all these cases. Shown in Fig. 5.3 is $\mathcal{C}(\theta)$ for a half metal with $L_x = L_y = L_z$. The top dashed line in Fig. 5.3 is the variance of the conductance in the absence of spin-orbit scattering. Without spin-orbit scattering, there is no angle-dependent mesoscopic correction

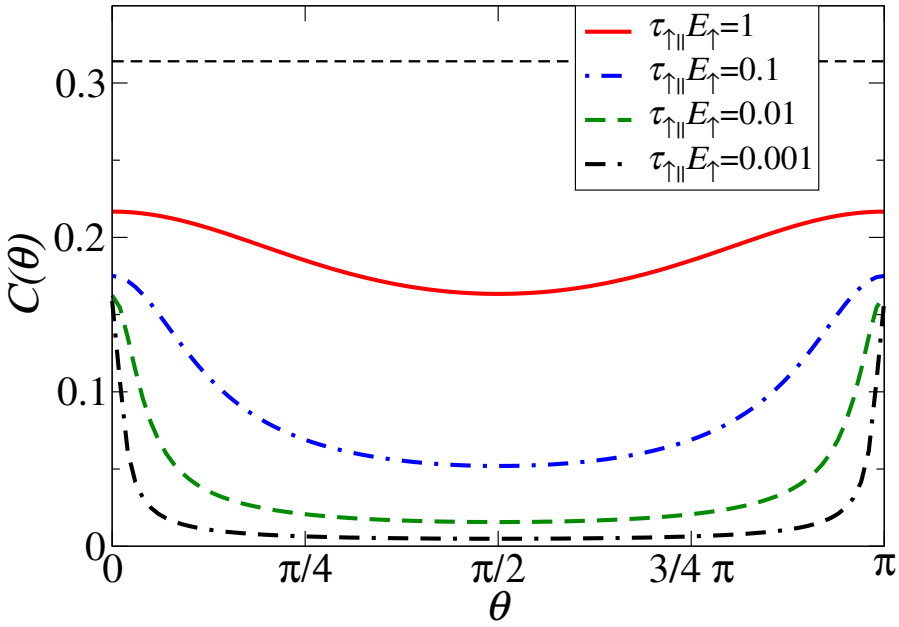

Figure 5.3: The correlation function of the conductance at different directions of the magnetization, for various strengths of the spin orbit scattering. Results shown here are for a half metal with cubic geometry.

to the conductance, so $\mathcal{C}(\theta)$ is independent of θ. For $\tau_{\uparrow\|} \ll 1/E_\uparrow$, conductance fluctuations saturate at half their value without spin-orbit scattering. Changing the magnetization by a small angle θ_c changes the mesoscopic conductance correction enough to lose all conductance correlations. Our calculation shows

$$\theta_c \sim (\tau_{\uparrow\|} E_\uparrow)^{1/2} \sim (\tau_{\uparrow\|}/\tau_\uparrow)^{1/2} l/L, \tag{5.17}$$

where l is the mean free path. In a realistic ferromagnet, the quantitative form of $\mathcal{C}(\theta)$ is different, although the qualitative picture, including the estimate for the correlation angle θ_c is the same as for the half metal (see Eq. 5.15).

5.4 Discussion and conclusion

Let us estimate the correlation angle θ_c for the spin-orbit induced mesoscopic conductance fluctuations. For the highly disordered ferromagnetic wires used in the experiments of Refs. [6, 7], the mean free path l is of the order of a few nm. Taking the spin-orbit times $\tau_\|$ and $\tau_\perp$ within an order of magnitude of the elastic scattering time τ (as is appropriate for Co [16]), we find $\theta_c \sim (1 \times 10^{-8}\text{m})/L$. (Recall that L has to be replaced by the phase coherence length L_ϕ if $L_\phi < L$.) This would be sufficiently small to explain the few conductance oscillations seen in the experiment of Ref. [7], for which $L_\phi \sim 30$nm and the conductance was measured as a function of an external magnetic field that changed the magnetization direction.

It is instructive to compare the correlation angle θ_c for spin-orbit induced conductance fluctuations considered here to the correlation angle arising from the coupling of the electron's charge to the internal magnetic field. The latter is $\sim \Phi_0/\Phi$, where Φ is the magnetic flux through the sample and Φ_0 is the flux quantum. Taking the internal magnetic field to be ~ 2T, as is appropriate for Co, one finds

a correlation angle $\sim (2 \times 10^{-15}\mathrm{m}^2)/L^2$. Hence, with the parameters taken above, the orbital effect will dominate for samples with size $L \gtrsim 2 \times 10^{-7}$m. This is in agreement with Ref. [7], where it was shown that the orbital effect alone cannot account for the observed conductance fluctuations [7].

BIBLIOGRAPHY

[1] P. A. Lee and A. D. Stone, Phys. Rev. Lett. **55**, 1622 (1985).

[2] P. A. Lee, A. D. Stone, and H. Fukuyama, Phys. Rev. B **35**, 1039 (1987).

[3] B. L. Altshuler, JETP Lett. **41**, 648 (1985).

[4] B. L. Altshuler and D. E. Khmelnitskii, JETP Lett. **42**, 359 (1986).

[5] B. L. Altshuler and B. I. Shklovskii, Sov. Phys. JETP **64**, 127 (1986).

[6] S. Lee, A. Trionfi, and D. Natelson, Phys. Rev. B **70**, 212407 (2004).

[7] Y. G. Wei, X. Y. Liu, L. Y. Zhang, and D. Davidović, cond-mat/0509452 (2005).

[8] G. Tatara and H. Fukuyama, Phys. Rev. Lett. **78**, 3773 (1997).

[9] Y. Lyanda-Geller, I. L. Aleiner, and P. M. Goldbart, Phys. Rev. Lett. **81**, 3215 (1998).

[10] V. K. Dugaev, P. Bruno, and J. Barnás, Phys. Rev. B **64**, 144423 (2001).

[11] P. W. Brouwer and D. A. Gorokhov, Phys. Rev. Lett. **95**, 017202 (2005).

[12] R. C. O'Handley, *Modern Magnetic Materials* (Wiley, New York, 2000).

[13] H. Bouchiat and G. Montambaux, J. Phys. (Paris) **50**, 2695 (1989).

[14] H.-F. Cheung, E. K. Riedel, and Y. Gefen, Phys. Rev. Lett. **62**, 587 (1989).

[15] B. L. Altshuler, Y. Gefen, and Y. Imry, Phys. Rev. Lett. **66**, 88 (1991).

[16] L. Piraux, S. Dubois, C. Marchal, J. M. Beuken, J. F. D. L. Filipozzi, K. Ounadjel, and A. Fert, J. Magn. Magn. Mater. **156**, 317 (1996).

Appendix A

Appendix to Chapter 4: Third order torque

The perturbative calculation of Sec. 4.2 focused on the case of a large applied magnetic field because, in that case, theoretical results for the spin wave amplitude do not depend on sample-dependent anisotropy energies. In this appendix we outline the theory for the general case.

For the most general case, one needs a better ansatz for the intrinsic torque $\boldsymbol{\tau}_{\rm an}$ than Eqs. (4.14) or (4.15), as well as an expression for the current-induced torque that does not rely on rotation symmetry around the easy axis. In principle the $\boldsymbol{\tau}_{\rm an}$ can be derived from the Free energy $\boldsymbol{\tau}_{\rm an} = -(\gamma/M)(\partial F/\partial \hat{\mathbf{m}}) \times \hat{\mathbf{m}}$ if there was some way to estimate the higher-order expansion coefficients. Once $\boldsymbol{\tau}_{\rm an}$ is known or determined empirically, the dynamics would still depend on the current-induced spin-transfer torque.

The general expression for the torque $\boldsymbol{\tau}_{\rm an}$ is most conveniently derived from the Free energy, $\boldsymbol{\tau}_{\rm an} = -(\gamma/M)(\partial F/\partial \hat{\mathbf{m}}) \times \hat{\mathbf{m}}$. Since we are interested in the mode $\hat{\mathbf{m}}(\mathbf{q}_{\rm c})$ only, we can expand F in powers of $m_1(\mathbf{q}_{\rm c})$ and $m_2(\mathbf{q}_{\rm c})$, up to fourth order

as

$$\begin{aligned} F(\hat{\mathbf{m}}) &= \frac{1}{2}\left[k_1 m_1(\mathbf{q}_c)^2 + k_2 m_2(\mathbf{q}_c)^2\right] \\ &\quad + \sum_{j=0}^{3} k'_j m_1(\mathbf{q}_c)^j m_2(\mathbf{q}_c)^{3-j} \\ &\quad + \sum_{j=0}^{4} k''_j m_1(\mathbf{q}_c)^j m_2(\mathbf{q}_c)^{4-j}. \end{aligned} \tag{A.1}$$

The higher-order expansion constants k'_j, $j = 0, 1, 2, 3$, and k''_j, $j = 0, 1, \ldots, 4$, are not governed by any special symmetry and therefore likely to be sample specific. (The cubic terms in the expansion of $F(\hat{\mathbf{m}})$ may be forbidden if there is a reflection symmetry around the easy axis. However, there is no such symmetry in the presence of an applied magnetic field that is not aligned with the one of the sample's easy or hard axes, so that cubic terms need to be included in a general treatment.) Note that the higher-order torque terms are as important in determining the spin wave amplitude as the higher-order current-induced spin-transfer torque. Unless these coefficients are known independently, a calculation of the spin wave amplitude has no predictive value — that was the reason why the main text addressed the case of a large applied magnetic field.

We now list our general results for the second and third order potentials and third-order spin-transfer torque. The symbols used are defined in Sec. 4.2 of the main text. The second-order charge potential expansion coefficients for the normal-

metal spacer are

$$
\begin{aligned}
a_{\rm c}^{(2)}(\mathbf{q}) \;&=\; ej\sum_{\mathbf{q}'} \\
&\Bigg\{\frac{[G_{\rm s}(0)+G_{\rm s}(\mathbf{q})-2G_{\rm s}(\mathbf{q}')]D(\mathbf{q}')+2[G_{\rm s}(0)-G_{\rm s}(\mathbf{q}')][G_{\rm s}(\mathbf{q})-G_{\rm s}(\mathbf{q}')][g_1+G_{\rm s}(\mathbf{q}')]}{D(\mathbf{q}')g_{\rm m}(0)g_{\rm m}(\mathbf{q})} \\
&\quad\times[m_1(\mathbf{q}')m_1(\mathbf{q}-\mathbf{q}')+m_2(\mathbf{q}')m_2(\mathbf{q}-\mathbf{q}')] \\
&\quad-\frac{2g_2[G_{\rm s}(0)-G_{\rm s}(\mathbf{q})][G_{\rm s}(\mathbf{q})-G_{\rm s}(\mathbf{q}')]}{D(\mathbf{q}')g_{\rm m}(0)g_{\rm m}(\mathbf{q})}[m_1(\mathbf{q}')m_2(\mathbf{q}-\mathbf{q}')-m_2(\mathbf{q}')m_1(\mathbf{q}-\mathbf{q}')]\Bigg\} \\
&-\hbar\sum_{\mathbf{q}'}\Bigg\{\frac{[G_{\rm s}(\mathbf{q})-G_{\rm s}(\mathbf{q}')][D(\mathbf{q}')-G_{\rm s}(\mathbf{q}')(g_1+G_{\rm s}(\mathbf{q}'))]}{D(\mathbf{q}')g_{\rm m}(\mathbf{q})} \\
&\quad\times[m_1(\mathbf{q}-\mathbf{q}')\dot{m}_2(\mathbf{q}')-m_2(\mathbf{q}-\mathbf{q}')\dot{m}_1(\mathbf{q}')] \\
&+\frac{g_2[G_{\rm s}(\mathbf{q})-G_{\rm s}(\mathbf{q}')]G_{\rm s}(\mathbf{q})}{D(\mathbf{q}')g_{\rm m}(\mathbf{q})}[m_1(\mathbf{q}-\mathbf{q}')\dot{m}_1(\mathbf{q}')+m_2(\mathbf{q}-\mathbf{q}')\dot{m}_2(\mathbf{q}')]\Bigg\}\,.
\end{aligned}
\tag{A.2}
$$

The coefficient $a_{\rm c}^{(2)}(0)$ determines how the spin wave instability affects the resistance of the ferromagnetic layer, cf. Eq. (4.44) in the main text. The second order correction to the 3-component of the spin potential is given by the expansion co-

efficients

$$
\begin{aligned}
\mathbf{a}_{\mathrm{s3}}^{(2)}(\mathbf{q}) \;=\; & ej\sum_{\mathbf{q}'}\Bigg\{\frac{1}{2g_{\mathrm{m}}(0)}[m_1(\mathbf{q}')m_1(\mathbf{q}-\mathbf{q}')+m_2(\mathbf{q}')m_2(\mathbf{q}-\mathbf{q}')] \\
& -\frac{1}{D(\mathbf{q}')g_{\mathrm{m}}(0)g_{\mathrm{m}}(\mathbf{q})}\,[D(\mathbf{q}')(g_+ + 2G_{\mathrm{c}}(\mathbf{q}))(G_{\mathrm{s}}(0)+G_{\mathrm{s}}(\mathbf{q})-2G_{\mathrm{s}}(\mathbf{q}')) \\
& -(G_{\mathrm{s}}(0)-G_{\mathrm{s}}(\mathbf{q}'))(g_1+G_{\mathrm{s}}(\mathbf{q}))(g_{\mathrm{m}}(\mathbf{q})-2(g_+ + 2G_{\mathrm{c}}(\mathbf{q})))(G_{\mathrm{s}}(\mathbf{q})-G_{\mathrm{s}}(\mathbf{q}'))] \\
& \qquad\times[m_1(\mathbf{q}')m_1(\mathbf{q}-\mathbf{q}')+m_2(\mathbf{q}')m_2(\mathbf{q}-\mathbf{q}')] \\
& -\frac{g_2[G_{\mathrm{s}}(0)-G_{\mathrm{s}}(\mathbf{q})][2(g_+ + 2G_{\mathrm{c}}(\mathbf{q}))(G_{\mathrm{s}}(\mathbf{q})-G_{\mathrm{s}}(\mathbf{q}'))-g_{\mathrm{m}}(\mathbf{q})]}{D(\mathbf{q}')g_{\mathrm{m}}(0)g_{\mathrm{m}}(\mathbf{q})} \\
& \qquad\times[m_1(\mathbf{q})m_2(\mathbf{q}-\mathbf{q}')-m_2(\mathbf{q})m_1(\mathbf{q}-\mathbf{q}')]\Bigg\} \\
& -\hbar\sum_{\mathbf{q}'}\Bigg\{\frac{g_2G_{\mathrm{s}}(\mathbf{q}')[g_{\mathrm{m}}(\mathbf{q})-2(g_+ + 2G_{\mathrm{c}}(\mathbf{q}))(G_{\mathrm{s}}(\mathbf{q})-G_{\mathrm{s}}(\mathbf{q}'))]}{2D(\mathbf{q}')g_{\mathrm{m}}(\mathbf{q})} \\
& \qquad\times[m_1(\mathbf{q}-\mathbf{q}')\dot{m}_1(\mathbf{q}')+m_2(\mathbf{q}-\mathbf{q}')\dot{m}_2(\mathbf{q}')] \\
& -\frac{[D(\mathbf{q}')-G_{\mathrm{s}}(\mathbf{q}')(g_1+G_{\mathrm{s}}(\mathbf{q}'))][g_{\mathrm{m}}(\mathbf{q})-2(g_+ + 2G_{\mathrm{c}}(\mathbf{q}))(G_{\mathrm{s}}(\mathbf{q})-G_{\mathrm{s}}(\mathbf{q}'))]}{2D(\mathbf{q}')g_{\mathrm{m}}(\mathbf{q})} \\
& \qquad\times[m_1(\mathbf{q}-\mathbf{q}')\dot{m}_2(\mathbf{q}')-m_2(\mathbf{q}-\mathbf{q}')\dot{m}_1(\mathbf{q}')]\Bigg\}, \qquad \text{(A.3)}
\end{aligned}
$$

The very first term describes the effect of a uniform magnetization rotation; the remaining terms are the result of a non-uniform magnetization. There are second-order corrections to the spin potential expansion coefficients a_1 and a_2 that arise from the presence of cubic terms in the anisotropy Free energy. Such cubic terms cause second-order contributions to the time derivatives $\dot{m}_1$ and $\dot{m}_2$, which give a contribution to the second order spin potentials $a^{(2)}$ in the same way as the first-order time contribution to the time derivative affects the first-order spin potentials $a^{(1)}$, see Eq. (4.21).

Instead of listing the third-order potentials $a^{(3)}$, we describe the corresponding current-induced torque. We specialize to the contributions that are cubic in the magnetization amplitude at wavevector $\mathbf{q}_{\mathrm{c}}$. The resulting torque has terms proportional to the third-order contributions to the time derivatives of the magne-

tization. These terms give rise to a renormalized Gilbert damping coefficient and a renormalized gyromagnetic ratio, see Eq. (4.22). The remaining terms can be written as $2\tilde{\boldsymbol{\tau}}(0) + \tilde{\boldsymbol{\tau}}(2\mathbf{q}_{\rm c})$, where (again using two-component spinor notation)

$$
\begin{aligned}
\tilde{\tau}^{(3)}(\mathbf{k}) \;=\; & \frac{-\hbar\gamma}{2Mde^2 D(\mathbf{q}_{\rm c})^2 g_{\rm m}(0) g_{\rm m}(\mathbf{k})} \\
& \times \{2ejg_2 D(\mathbf{q}_{\rm c}) G_{\rm s}(\mathbf{q}_{\rm c})[G_{\rm s}(\mathbf{q}_{\rm c}) - G_{\rm s}(\mathbf{k})][g_+ + 2G_{\rm c}(\mathbf{k})][G_{\rm s}(0) - G_{\rm s}(\mathbf{q}_{\rm c})] \\
& \times i\sigma_2 m(\mathbf{q}_{\rm c}) m^{\rm T}(\mathbf{q}_{\rm c}) m(\mathbf{q}_{\rm c}) \\
& - [g_{\rm m}(\mathbf{k}) + 2(g_+ + 2G_{\rm c}(\mathbf{k}))(G_{\rm s}(\mathbf{q}_{\rm c}) - G_{\rm s}(\mathbf{k}))] \\
& \times \big[- ej[(2G_{\rm s}(\mathbf{q}_{\rm c}) - G_{\rm s}(0) - G_{\rm s}(\mathbf{k}))D(\mathbf{q}_{\rm c}) \\
& \quad + 2(G_{\rm s}(0) - G_{\rm s}(\mathbf{q}_{\rm c}))(g_1 + G_{\rm s}(\mathbf{q}_{\rm c}))(G_{\rm s}(\mathbf{q}_{\rm c}) - G_{\rm s}(\mathbf{k}))] \\
& \times [D(\mathbf{q}_{\rm c}) - G_{\rm s}(\mathbf{q}_{\rm c})(g_1 + G_{\rm s}(\mathbf{q}_{\rm c}))] m(\mathbf{q}_{\rm c}) m^{\rm T}(\mathbf{q}_{\rm c}) m(\mathbf{q}_{\rm c}) \\
& + ejg_2 G_{\rm s}(\mathbf{q}_{\rm c})[G_{\rm s}(\mathbf{q}_{\rm c}) - G_{\rm s}(\mathbf{k})] \\
& \times [D(\mathbf{q}_{\rm c}) + 2(G_{\rm s}(0) - G_{\rm s}(\mathbf{q}_{\rm c}))(g_1 + G_{\rm s}(\mathbf{q}_{\rm c}))] i\sigma_2 m(\mathbf{q}_{\rm c}) m^{\rm T}(\mathbf{q}_{\rm c}) m(\mathbf{q}_{\rm c}) \\
& + \hbar g_2 G_{\rm s}(\mathbf{q}_{\rm c}) g_{\rm m}(0)[G_{\rm s}(\mathbf{q}_{\rm c}) - G_{\rm s}(\mathbf{k})][D(\mathbf{q}_{\rm c}) - G_{\rm s}(\mathbf{q}_{\rm c})(g_1 + G_{\rm s}(\mathbf{q}_{\rm c}))] \\
& \times \dot{m}(\mathbf{q}_{\rm c}) m^{\rm T}(\mathbf{q}_{\rm c}) m(\mathbf{q}_{\rm c}) \\
& + (\hbar/2)[G_{\rm s}(\mathbf{q}_{\rm c}) - G_{\rm s}(\mathbf{k})] D(\mathbf{q}_{\rm c}) g_{\rm m}(0)[D(\mathbf{q}_{\rm c}) - G_{\rm s}(\mathbf{q}_{\rm c})(2g_1 + G_{\rm s}(\mathbf{q}_{\rm c}))] \\
& \times [m(\mathbf{q}_{\rm c}) m^{\rm T}(\mathbf{q}_{\rm c}) i\sigma_2 \dot{m}(\mathbf{q}_{\rm c}) - i\sigma_2 m(\mathbf{q}_{\rm c}) m^{\rm T}(\mathbf{q}_{\rm c}) \dot{m}(\mathbf{q}_{\rm c})] \\
& + (\hbar/2)[G_{\rm s}(\mathbf{q}_{\rm c}) - G_{\rm s}(\mathbf{k})] g_{\rm m}(0) \\
& \times [(D(\mathbf{q}_{\rm c}) - G_{\rm s}(\mathbf{q}_{\rm c})(g_1 + G_{\rm s}(\mathbf{q}_{\rm c})))^2 - (g_2 G_{\rm s}(\mathbf{q}_{\rm c}))^2] \\
& \times i\sigma_2 \dot{m}(\mathbf{q}_{\rm c}) m^{\rm T}(\mathbf{q}_{\rm c}) m(\mathbf{q}_{\rm c}) \,\big] \big\} \,.
\end{aligned}
\tag{A.4}
$$

(A.5)

Once the perturbative expansions for the anisotropy torque and the current-induced spin-transfer torque are known, the Landau-Lifshitz-Gilbert equation can be solved for the magnetization dynamics.

Appendix B

Appendix to Chapter 5: Calculation of diagrams

In this Appendix we further discuss the methods used in arriving at the results of Chapter 5. While the framework for calculating conductance fluctuations using diagrammatic perturbation theory is now well established, the steps outlined in this Appendix provide some of the details that is usually skipped in the literature. Moreover, since the calculation presented in Chapter 5 generalized the standard UCF result, we provide additional details on how to include the effect of spin-orbit scattering and the matrix spin-structure that is necessary for considering a ferromagnet where the majority and minority spins states are inequivalent channels that interact through the spin-orbit scattering.

We identify three areas where we feel the calculations presented in the main text merit elaboration. First, we will discuss the enumeration of diagrams and the different ways of canceling terms that allow us to arrive at Eq. 5.12. Second, we examine the matrix spin-structure of the conductance correlator and show that the calculation reduces to a sum over spin-eigenvalues, and finally we look at the

effects of spin-orbit scattering, provide the details leading up to Eq. 5.16 and show that the cancellation of diagrams remains true even in the presence of spin-orbit scattering.

B.1 Relationships between diagrams

The purpose of this section is to motivate the starting point for the calculation in Chapter 5. In Eq.(5.12) we had

$$\mathcal{C}(\theta) = \frac{3e^4}{2L_z^4 h^2} \sum_{\mathbf{q}} \mathrm{tr}\left[JD(\mathbf{q})JD(\mathbf{q}) + JC(\mathbf{q})JC(\mathbf{q})\right]. \tag{B.1}$$

We now motivate the prefactor 3/2 that comes from the enumeration of the different conductance fluctuation diagrams. For the moment we discard the effects of spin-orbit scattering or the matrix structure of Diffuson and Cooperon ladders and show in later sections that these do not change the result.

The diagrams which contribute to the conductance correlation are all shown in Fig. B.1. When calculating these diagrams, one needs to sum over different things, for example, the shaded regions represent either Cooperons or Diffuson ladders. One also needs to sum over diagrammatic combinatorial factors and spin. However, for this section, the most important summation is over all combinations of retarded and advanced Greens functions which have poles in the upper and lower halves of the complex plane respectively. Since this property determines the rules for analytical continuation during the complex integration, we equivalently talk of this summation as one over the different analyticities. Requiring that the Diffuson and Cooperon ladders be made from Greens functions with different analyticity, this provides certain restrictions. In particular, we conclude that Diagrams B.1 (a), (d) and (e) have two allowed possibilities, where either the analyticity does

not changes at the current vertex (which we shall denote with the superscript A), and those where the analyticity does change (denoted with superscript B). We note that Diagrams B.1 (b) and (c) are required to be of type A. To make further progress one needs to study the different types of Hikami boxes that found in the diagrams in Fig. B.1. These have been enumerated in Fig. B.2 which shows the different types of current vertices coupled to Greens functions using + and − labels to indicate Greens functions with positive and negative poles. Each of these diagrams can be calculated explicitly. If we call the the diagrams in Fig. B.2 (a), (b) as $j_0^{A,B}$, (c) as j_1 (which is of type B), (d), (e) as $j_2^{A,B}$ and (f), (g) as $j_3^{A,B}$, we find

$$\begin{aligned} j_0 &= j_0^A = j_0^B = \frac{4\pi\nu k_F^2\tau^3}{3} \\ j_1 &= j_0 \frac{d}{idr_{1,z}} \int \frac{d\mathbf{q}}{(2\pi)^3} \exp[i\mathbf{q}.(\mathbf{r}_1 - \mathbf{r}_2)], \\ j_2^A &= -\frac{j_0}{2}, \quad j_2^B = j_0, \quad j_3^A = 0, \quad j_3^B = -\frac{j_0}{2}. \end{aligned} \tag{B.2}$$

We are now in a position to derive the 3/2 prefactor. The method of Lee, Stone and Fukuyama [1, 2] was to sum over all allowed analyticities. With this one sees that the contributions from the diagrams of Fig. B.1 (d) and (e) becomes $j_2^A + j_2^B + j_3^A + j_3^B = 0$. This cancellation allows one to get the conductance correlation by only considering the diagrams of Fig. B.1 (a), (b) and (c) which we shall call F_a, F_b and F_c. It will be shown in the last section of this appendix that both with and without spin-orbit scattering, these diagrams at zero temperature and zero frequency have the property that $F_a = -F_b = (4/3)F_c$ so that their sum (multiplied by 2 to count for both analyticities) is given by $(3/2)F_a$ as required. Another method is that of Altshuler and Shklovskii [3] where they argue that all diagrams of type A that do not change analyticity are a total derivative and sum

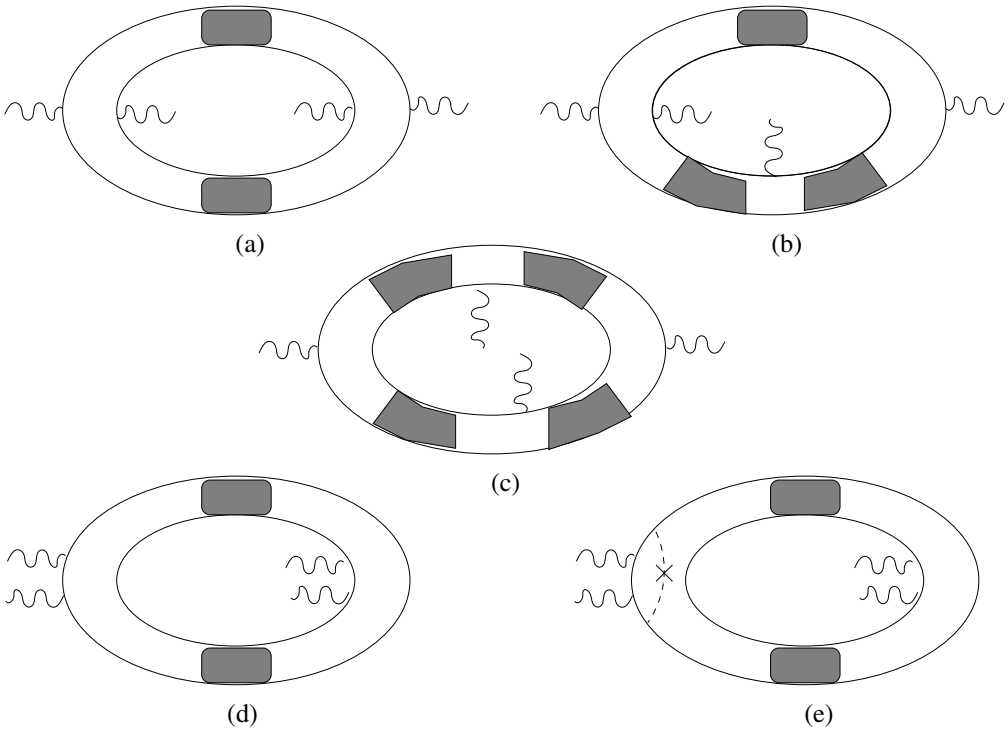

Figure B.1: Diagrams contributing to conductance correlations. For each of the diagrams, the shaded area represents Diffuson or Cooperon Ladders. The dashed line in diagram (e) represents an additional single impurity scattering.

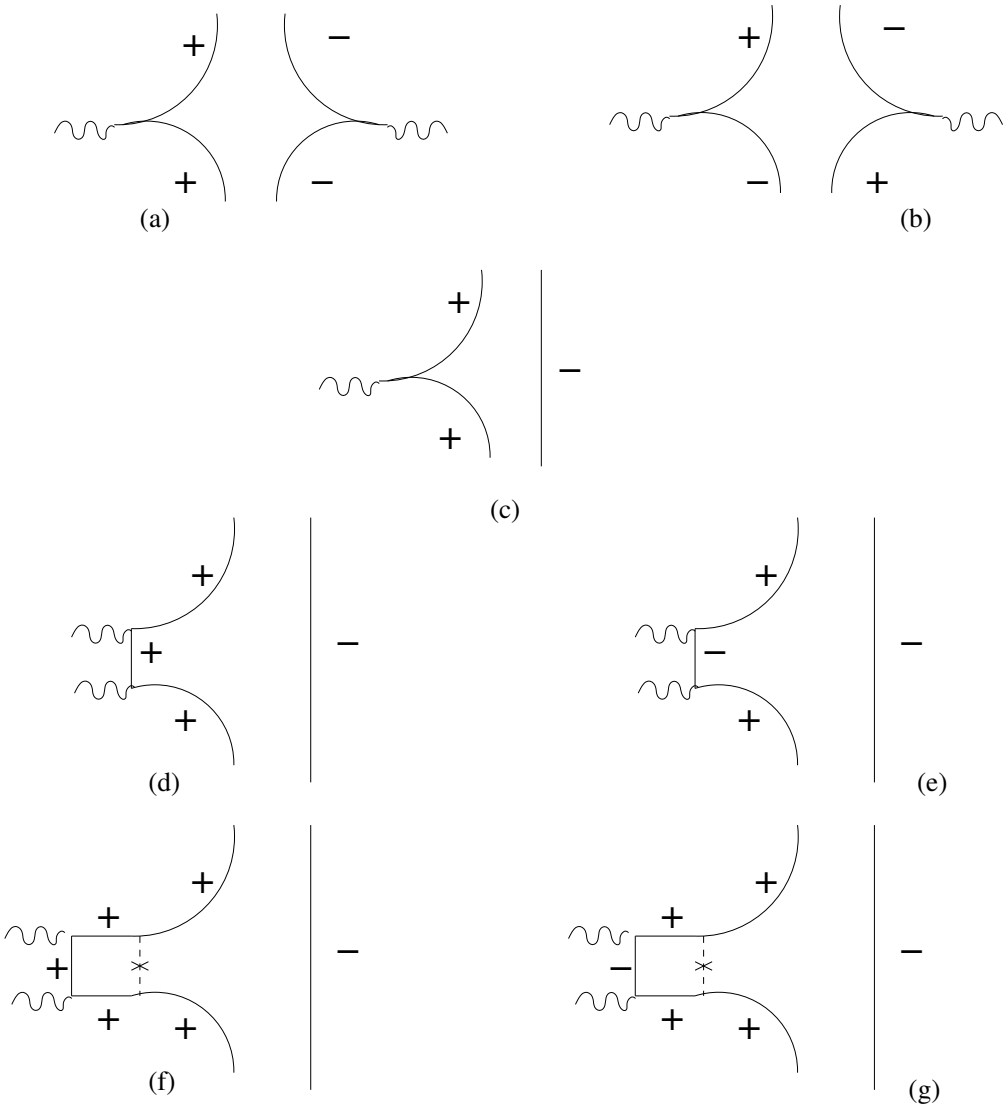

Figure B.2: Different types of current vertices found in the conductance correlation diagrams shown in Fig. B.1. Diagrams (a), (c), (d), (f) do not change their analyticity at the vertex, while (b) and (e) do.

to zero. Considering only diagrams of type B, we have that the sum of diagrams in Fig. B.1 can be represented as the sum of $j_0^B + j_2^B + j_3^B = (3/2)j_0$. Therefore, using this method one only needs to calculate diagrams of the form Fig. B.1 (a) and multiply by the factor 3/2 giving the required result.

B.2 Adding spin structure

The heart of this section is to show that the same dimensional cancellations that made the UCF universal without the spin structure works even when we use a matrix formulation. The key idea is that to leading order, these dimensional cancellations are preserved for each spin-species independently. In particular, we have that the current vertex $J_{\alpha\beta} = (4\pi/3)v_{\mathrm{F}\alpha}^2\tau_\alpha^3\delta_{\alpha\beta}$ and $KD = (2\pi\nu_\alpha\tau_\alpha)\delta_{\alpha,\beta}$ are both diagonal in spin space (See Eq. 5.9). Recall that D is the matrix Diffusion, K is its inverse and α, β are spin indices. We also have that ν is a density of states and τ is the scattering time. The universal properties arise because

$$\frac{1}{L_z^2} J_{\alpha\alpha} \frac{(KD)_{\alpha\alpha}}{E_\alpha \tau_\alpha} = \frac{2}{\pi^2} \tag{B.3}$$

is a constant independent of any system property. It is the cancellation of any dependence on the system size L_z or mean free path $v_{\mathrm{F}}\tau$ that makes the quantity universal.

Using a eigenvector decomposition of the form $D(\mathbf{r}, \mathbf{r}') = \sum_m Q_m^*(\mathbf{r}) Q_m(\mathbf{r}') K_m^{-1} N$ where all the matrix structure is in K and $N_{\alpha\beta} = \delta_{\alpha\beta}(2\pi\nu_\alpha\tau_\alpha)^{-1}$, we can then write

$$\begin{aligned} \frac{1}{L_z^4} tr[JD(\mathbf{q})JD(\mathbf{q})] &= \frac{4}{\pi^4} \sum_n tr\Lambda_n^{-2}, \\ &= \frac{4}{\pi^4} \sum_n tr \begin{bmatrix} \lambda_{n\uparrow} & b \\ \tilde{b} & \lambda_{n\downarrow} \end{bmatrix}^{-2}, \end{aligned} \tag{B.4}$$

with $\lambda_{n\alpha} = g(n) + f_\alpha$ separating into a function $g(n) = n_z^2 + n_x^2(L_z/L_x)^2 + n_y^2(L_z/L_y)^2$ that depends on integer eigenvalues $n = (n_x, n_y, n_z)$, where $n_z = 1, 2, \cdots, \infty$; $n_x, m_y = 0, 1, 2, \cdots, \infty$ and a function

$$f_\alpha = \frac{2}{\tau_{\alpha\perp} E_\alpha} + \frac{1 - cos\theta}{\tau_{\alpha\parallel} E_\alpha}, \tag{B.5}$$

that depends on spin and magnetization direction. We also have that $b\tilde{b} = (1 + \cos\theta)^2/(E_\uparrow E_\downarrow \tau_{\uparrow\perp}\tau_{\downarrow\perp})$.

The form of Eq. B.4 makes it evident that the conductance correlator depends only on the eigenvalues of Λ_n (which can be thought of as a correctly scaled inverse Diffuson). This result holds for even more complicated diagrams with three and four Diffuson or Cooperon ladders (see Fig. B.1 (b), (c) and the discussion in the preceding section for different ways of summing diagrams). This property can be understood by observing that the part of the matrix Λ_n that depends on n is proportional to the unit matrix as $g(n)I_2$, and therefore all traces over matrix products of $\{\Lambda_n\}$ can be simultaneously diagonalized. It follows that the conductance correlator only depends on the eigenvalues of Λ_n which are given by $\lambda_\pm^n = g(n) + a_\pm$. The eigenvalues can be calculated explicitly to find

$$\begin{aligned} a_\pm(\theta) \;=\; & \frac{1}{\tau_{\uparrow\perp} E_\uparrow} + \frac{1}{\tau_{\downarrow\perp} E_\downarrow} + \frac{\tau_{\uparrow\parallel} E_\uparrow + \tau_{\downarrow\parallel} E_\downarrow}{2\tau_{\uparrow\parallel}\tau_{\downarrow\parallel} E_\uparrow E_\downarrow}(1 - \cos\theta)) \\ & \pm \sqrt{\frac{(1+\cos\theta)^2}{\tau_{\uparrow\perp}\tau_{\downarrow\perp} E_\uparrow E_\downarrow} + \left[\frac{1}{\tau_{\uparrow\perp} E_\uparrow} - \frac{1}{\tau_{\downarrow\perp} E_\downarrow} - \frac{\tau_{\uparrow\parallel} E_\uparrow - \tau_{\downarrow\parallel} E_\downarrow}{2\tau_{\uparrow\parallel}\tau_{\downarrow\parallel} E_\uparrow E_\downarrow}(1 - \cos\theta)\right]^2} \end{aligned} \tag{B.6}$$

The main conclusion of this section is that the full spin structure does not present any serious complications to the calculation. The results for a half-metal carry forward for the full ferromagnet where to get the conductance fluctuation one would use the same formalism, but sum over the two spin eigenvalues of the correctly normalized diffusion equation.

B.3 Effects of spin-orbit scattering

The diagram F_a represented by Fig. B.1 can be calculated as

$$F_a = \frac{8}{\pi^4} \sum_n \lambda_n^{-2}. \tag{B.7}$$

To make the connection with the notation of Lee, Stone and Fukuyama [2], what they call $2(4/\pi^2)^2 F1$ is what we call $16 \times F_a$, where the factor of 16 comes from summing our diagram over spin (4), Cooperons and Diffusons (2), and analyticity (2). We now proceed to calculate the diagrams. Actually, we only do the sum over n_z which corresponds to the quasi one dimensional limit (with $n_x = n_y = 0$). However, we note that the structure of the summations for 2 and 3 dimensions imply that the relations proved between F_a, F_b and F_c in quasi one dimension hold for higher dimensions (this is not surprising in light of the earlier discussion on the cancellation of diagrams). For quasi one dimension, we have

$$F_a = \frac{8}{\pi^4} \sum_j \frac{1}{(j^2 + a)^2}, \tag{B.8}$$

where $j = n_z$ is an integer, and a is the term that depends on the spin-orbit scattering and the angle θ. For the purpose of this section a is just some real constant. In the limit $a \to 0$ one can calculate that

$$\begin{aligned}
F_a &= \frac{8}{\pi^4} \sum_{j=1}^{\infty} \frac{1}{j^4} = \frac{2}{45} \\
F_b &= -\frac{4^4}{\pi^3} \sum_{\substack{j=\text{odd} \\ k=\text{even}}} \frac{1}{j^2((j+k)(j-k))^2} + \frac{1}{k^2((j+k)(j-k))^2} \\
&= -\frac{2}{45}, \\
F_c &= 3\left(\frac{4}{\pi^2}\right)^2 \left(\frac{4}{\pi}\right)^4 \sum_{\substack{j,l \\ k,m \ \text{odd} \\ \text{even}}} \frac{1}{(j^2-k^2)(k^2-l^2)(l^2-m^2)(m^2-j^2)} \\
&= \frac{1}{30},
\end{aligned} \tag{B.9}$$

from which one can verify that $F_a = -F_b = (4/3)F_c$. We have verified that this continues to be true when the eigenvalues change from $\lambda_{a=0} = j^2$ to $\lambda_{a\neq 0} = (j^2+a)$. Here we present only the result for F_a.

$$\begin{aligned} F_a &= \frac{8}{\pi^4}\sum_{j=1}^{\infty}\frac{1}{(j^2+a)^2} \\ &= \left(\frac{8}{\pi^4}\right)\frac{-2+\pi\sqrt{a}\coth(\pi\sqrt{a})+a\pi^2(\sinh(\pi\sqrt{a}))^{-2}}{4a^2}, \end{aligned} \tag{B.10}$$

which in the limit of $a \to 0$ reproduces the earlier result of $2/45$. Having done this summation, and using the definition of a from Eq. 5.15, we immediately get Eq. 5.16.

BIBLIOGRAPHY

[1] P. A. Lee and A. D. Stone, Phys. Rev. Lett. **55**, 1622 (1985).

[2] P. A. Lee, A. D. Stone, and H. Fukuyama, Phys. Rev. B **35**, 1039 (1987).

[3] B. L. Altshuler and B. I. Shklovskii, Sov. Phys. JETP **64**, 127 (1986).